UNIVERSITY OF CAMBRIDGE

Jesus college

Cucurbit[*n*]uril-based colloidal self-assembly in hybrid polymeric systems

Author: Yuchao Wu

Supervised by: Prof. Oren A. Scherman

This dissertation is submitted for the degree of Doctor of Philosophy

September 30, 2017

Abstract

Supramolecular interactions are of great importance in the fabrication of new functional materials. In particular, colloidal assembly *via* supramolecular pathway has contributed to numerous innovations in material chemistry, on account of its specific, directional and dynamic non-covalent interactions. By taking advantage of the non-covalent supramolecular interactions, tailored complementary colloidal building blocks which are normally incompatible with each other could be integrated interdependently, forming novel hybrid materials with emerging properties. This thesis mainly focuses on the design, preparation and characterization of novel colloidal assemblies based on cucurbit[n]urils host-guest interactions, including hybrid 'raspberry-like' colloids, catalytic polymeric nanocomposites, advanced structured colloids, and supramolecular polymer colloidal hydrogel.

In the first chapter, the host-guest complexation of macrocycle cucurbit[n]urils is explained, with discussions of classic examples of supramolecular materials prepared by taking advantage of this supramolecular 'hand-cuff'. In addition, the research over supramolecular colloidal assemblies and the importance of their interfacial interactions are summarized.

The second chapter focuses on the preparation and characterization of hybrid 'raspberry-like' colloids through the host-guest complexation of cucurbit[8]urils (CB[8]). 'Hard' silica nanoparticles (NPs) were functionalized with azo-benzene (Azo) moieties, acting as a core of the 'raspberry-like' structure; 'Soft' polymeric colloids were prepared with methyl viologen (MV) moieties on the surface, serving as the corona of the 'raspberry-like' structure. Mixing the silica NPs and polymeric colloids with CB[8] in an aqueous environment results in a formation of the 1:1:1 ternary complex (K_{eq}=10^{12} M^{-2}) of CB[8],

MV and Azo in a stepwise manner. Consequently, the MV-functionalized polymeric colloids would be attached on the surface of the Azo-functionalized silica NPs directly, forming the 'raspberry-like' structures. Moreover, the 'raspberry-like' colloid can be reversibly dissembled via external stimuli, taking advantage of its dynamic non-covalent interactions. TEM (Transmission electron microscopy) and SEM (Scanning electron microscopy) of all colloids and hybrid assemblies were examined to build an intuitive understanding of these structures. This facile supramolecular approach provides a platform for the synthesis of colloids with topological complexity in material chemistry.

The third chapter mainly discuss the preparation, characterization and application of catalytic polymeric nanocomposites *via* cucurbit[7]urils (CB[7]) host-guest interactions. A supramolecular pathway was introduced to immobilize catalytically active metallic NPs onto polymeric colloidal substrates, considering the high affinities between CB[n]s and certain metallic NPs. MV functionalized polymeric colloids were prepared and complexed with CB[7], followed by *in-situ* reduction of metallic NPs. Spontaneously, the catalytic active nanocomposites were formed where metallic NPs with a narrow size distribution were anchored onto the MV functionalized polymeric colloids. Moreover, the catalytic efficiency of the nanocomposites was examined through Suzuki coupling reactions, demonstrating high conversion rate in aqueous environment with good recyclability. This facile and spontaneous supramolecular approach allows for control over size, morphology and composition of the nanocomposites.

Next, structured colloids with higher complexity were investigated as a continuation of the above work, which is demonstrated in the fourth chapter. Micro-sized Janus particles were prepared, one hemisphere of which were modified by naphthol moieties and further complexed with MV-functionalized NPs *via* CB[8] host-guest interactions. More importantly, a novel microfluidic compartmental self-assembly approach was employed. This method was devoted to assembling these functional particles in a confined microdroplet environment where any non-specific interactions between particles could be avoided. Therefore, targeted structures could be obtained and effectively screened out from a systematic sorting device. The molecular recognition of CB[8] successfully directs an asym-

metric assembly of supra-colloids in a control manner, representing a new platform for fabricating topological structures.

Beyond the assembly of complementary colloidal particles, the fifth chapter further looks at the effect of functional colloids in polymer network. Inspired by biological systems, a supramolecular polymer colloidal hydrogel (SPCH) was prepared comprising 98 wt% water that can be readily drawn into uniform (ca. 6 μm thick) 'supramolecular fibers' at room temperature. Functionalized polymer-grafted silica NPs, a semicrystalline hydroxyethyl cellulose derivative and CB[8] underwent aqueous self-assembly at multiple length scales to form the SPCH, facilitated by host-guest interactions at the molecular level and nano-fibril formation at colloidal length scale. Moreover, the fibers exhibit a unique combination of stiffness and high damping capacity (60-70%), the latter exceeding that of even biological silks and cellulose-based viscose rayon. The remarkable damping performance of the hierarchically-structured fibers is proposed to arise from the complex combination and interactions of 'hard' and 'soft' phases within the SPCH and its constituents. SPCH represent a new class of hybrid supramolecular composites, opening a window into fiber technology through low-energy manufacturing.

The sixth chapter further explored the fiber network and introduce a covalent network into the fiber polymeric matrix. The resulting hydrogel fiber (SCF) is showing high resilience in water. More interestingly, the fiber is capable of contracting up to 50% of its original length at high humidity, comparable to spider silk. In comparison to the supramolecular fibre (Chapter 5) where its polymers matrix is held by physical interactions, this new fiber is imparted with a second network of covalent cross-links *via* UV treatment. It exhibits up to 300% of uptake of water by its volume at high humidity, confirmed under the environmental scanning electronic microscopy (ESEM). Moreover, the SCF undergoes a cyclic relaxation-contraction response to wetting and drying, similar to spider silk. This type of fibre materials provides a new opportunity of fabricating biomimetic muscle for diverse applications, ranging from humanoid robots, prosthetic limbs, and exoskeletons.

In the end, a concluding chapter summarizes the presented work . It also highlights

the importance of supramolecular interactions when building blocks are assembled at colloidal interfaces and the great potential of supramolecular materials in the near future.

Contents

1 Introduction **1**

1.1 Chemistry Beyond the Molecules 1

1.1.1 Macrocyclic Host-Guest Complexation 2

1.1.2 Supramolecular 'hand-cuff' Based on CB[n]s 8

1.2 Supramolecular Colloidal Self-Assemblies 11

1.3 Aim 17

2 Hybrid Raspberry-like Colloids Based on Host-guest Interactions **19**

2.1 Introduction 20

2.2 Results and Discussion 23

2.2.1 Synthesis and Characterisation of Functional Nanoparticles 23

2.2.2 Fabrication of Hybrid Raspberry-like Colloids (HRCs) 27

2.3 Conclusion and Outlook 32

2.4 Experimental Appendix 33

2.4.1 Materials and General Methods 33

2.4.2 Synthesis of StMV 33

2.4.3 Synthesis of MV-NP (PSt-*co*-StMV) 34

2.4.4 Synthesis of Azo-silica NPs 34

2.4.5 Preparation of Hybrid Raspberry-like Colloids 35

2.4.6 Control Experiments of Raspberry-like Microspheres 35

2.4.7 Coating of Raspberry-like Microspheres 36

2.4.8 Control Experiments of Coating Raspberry-like Microspheres . . . 36

3 Catalytic Polymeric Nanocomposites *via* Cucurbit[n]uril Host-guest Interactions 37

3.1 Introduction . . . 38
3.2 Results and Discussion . . . 40
3.2.1 Fabrication of Polymeric Nanocomposites . . . 40
3.2.2 Catalysis with Palladium Nanocomposites . . . 45
3.3 Conclusion and Future work . . . 47
3.4 Experimental Appendix . . . 48
3.4.1 Materials and General Methods . . . 48
3.4.2 Synthesis of Palladium Nanocomposites . . . 48
3.4.3 Control Experiments of Palladium Nanocomposites . . . 48
3.4.4 Synthesis of Silver Nanocomposites . . . 49
3.4.5 Synthesis of Gold Nanocomposites . . . 49
3.4.6 General Protocol Used for Suzuki Couplings . . . 49

4 Compartmentalised Supramolecular Self-assembly of Supra-colloids 50

4.1 Introduction . . . 51
4.2 Results and Discussion . . . 52
4.2.1 Fabrication and Characterization of Janus Particles . . . 52
4.2.2 Compartmentalised Assembly of Supra-colloids . . . 54
4.3 Conclusion and Future Work . . . 61
4.4 Experimental Appendix . . . 62
4.4.1 Materials and General Methods . . . 62
4.4.2 Synthesis of PSt (P1) . . . 63
4.4.3 Synthesis and Characterization of PolyMMA-*co*-MANp (P2) . . . 63
4.4.4 Fabrication of Janus Nanoparticles . . . 64
4.4.5 Encapsulation of Janus Nanoparticles . . . 65
4.4.6 Fusion of Janus Nanoparticles . . . 66
4.4.7 Sorting of Janus Nanoparticles . . . 66

5 Bioinspired Supramolecular Fibers and its Mechanical Properties 67

5.1 Introduction . . . 68

5.2 Results and Discussion . . . 70

5.2.1 Self-assembly of SPCH . . . 70

5.2.2 Characterisation of the Supramolecular Fiber . . . 76

5.3 Conclusion and Future Work . . . 81

5.4 Experimental Appendix . . . 83

5.4.1 Materials and General Methods . . . 83

5.4.2 Preparation of Poly(Nipam-co-HEAm-MV) Grafted Silica NPs (P1) 84

5.4.3 SPCH Preparation . . . 87

5.4.4 Further Rheological Studies . . . 88

5.4.5 SEM Studies of SPCH . . . 88

5.4.6 Mechanical Test of Supramolecular Fiber . . . 88

6 Biomimmetic Contractile Fiber 91

6.1 Introduction . . . 92

6.2 Results and Discussion . . . 93

6.2.1 Characterisation of SCF . . . 99

6.3 Conclusion and Future Work . . . 102

6.4 Experimental Appendix . . . 103

6.4.1 Materials and General Methods . . . 103

6.4.2 Preparation of supramolecular polymer-colloidal hydrogel (H1) . . 104

6.4.3 Preparation of supercontracted fiber . . . 105

6.4.4 Mechanical test of the supercontracted fiber . . . 106

7 Conclusion and Outlook 111

Bibliography 114

List of Abreviations and common units

- AA - acrylic acid
- ACPA - 4,4′-Azobis(4-cyanopentanoic acid)
- ADA - adamantane amine
- AIBA - 2,2′-azobis(2-methylpropionamidine) dihydrochloride
- AIBN - azobisisobutyronitrile
- Am - acrylamide
- ATRP - atom-transfer radical-polymerization
- AZO - azobenzene
- CB[n] - cucurbit[n]uril
- CD - cyclodextrin
- CP - conjugated polymer
- CT - charge transfer
- DCM - dichloromethane
- DI - deionized water
- DLS - dynamic light scattering
- DMF - dimethylformamide
- DMSO - dimethyl sulfoxide

- DNA - deoxyribonucleic acid
- GPC - gel permeation chromatography
- FTIR - fourier transform infrared spectroscopy
- FITC - fluorescein isothiocyanate
- GPC - gel permeation chromatography
- HRCs - hybrid raspberry colloids
- HUMO - highest unoccupied molecular orbital
- HEAm - hydroxyethyl acrylamide
- HEC - hydroxyethyl cellulose glass
- HEMA - 2-hydroxyethyl methacrylate
- HPLC - high-performance liquid chromatography
- HRCs - hybrid raspberry-like colloids
- KDa - kilodalton
- LUMO - lowest occupied molecular orbital
- MMA - Methyl methacrylate
- Mn - Number Average Molecular Weight
- MANp - methacrylate-naphthol
- MV-OH - 1-(2-hydroxyethyl)-1′-methyl-[4,4′-bipyridine]-1,1′-diium di(hexafluorophosphate)
- MV - methyl viologen
- NCO - isocyanate
- NIPAM - N-Isopropylacrylamide

- NMR - nuclear magnetic resonance
- Np - 2-naphthol
- NPs - nanoparticles
- PDi - pyromellitic dianhydride
- PDI - polydisperitity
- PDMS - polydimethylsiloxane
- PEG - poly(ethylene glycols)
- PTFE - polytetrafluoroethylene
- PS - polystyrene
- PVA - poly(vinyl alcohol)
- PVP - polyvinylpyrrolidone
- r.t. - room temperature
- r.p.m - revolutions per minute
- SDS - sodium dodecyl sulfate
- SEFP - soap-free emulsion polymerization
- SEM - scanning electron microscope
- SPCH - supramolecular polymer-colloidal hydrogel
- TEM - transmission electron microscope
- TEOS - tetraethyl orthosilicate
- TDL - dibutyltin dilaurate
- THF - tetrahydrofuran

- TMNPS - transition-metal nanoparticles
- UV - ultraviolet
- ZP - zeta potential

Declaration

This report is submitted in the fulfilment for the PhD Study in Chemistry. Except where indicated to the contrary, either directly or by reference, the work described in this dissertation is solely the work of the author. This work by no means surpases the word limit of 60000.

Signed,

Number of words:

Yuchao Wu,
University of Cambridge

Acknowledgements

First of all, I would like to thank my supervisor, Prof. Oren A. Scherman, for giving me the opportunity to study in the world's best university, and searching funding for my PhD project in his group. I have learned this 'hand-free' style from him, once I came to this lab. It is essential for me to grow independently. I appreciate the degree of freedom he gave to us. Whenever, I want to do something, he is always supportive and tell me "go and try it!" Now I am confident to say, I am fully capable of conducting professional research and well prepared to solve any problems.

Next, I would like to acknowledge my co-workers as well as my colleagues in/outside the Scherman group, who helped me and let me work in such enjoyable environment. While I am writing this, a lot of funny and sweet stories in the past five years go through my mind, I become emotional several times. To thank them in turn:

I want to thank Yang Lan, now Dr. Lan, who is the first person I have met in the Melville Laboratory. He was in his second year at that time. I worked with him in my Mphil year as well as the first year of my PhD. He is a nice senior and a nice mentor, who trained me to do research from the entry level. Now if I am proud to say 'I have expertise in colloidal science and supramoelcular chemistry', or 'I am a expert user of TEM' etc, it was Yang who taught me these important things. I believe I will benefit from this in my future career. Beside, I also want to thank him as a considerable house mate, as a brother to all of us juniors. Secondly, Cindy, now Dr. Tan, I want to thank her for having a great time together as a colleague. We went to the Melville lab and all the induction sessions at the same time. Though we have not collaborated with each other in research inside the lab, we have joined to make tiramissu and macaroons in the kitchen. I enjoyed being a colleague with her. Third, Ziyi, (Dr. Yu), is my colleague outside the Scherman group.

We came into the department of chemistry almost at the same time (2012, September), and we have been working as co-workers for a long time. As a senior, he has taught me so many things through out my PhD. If I have any scientific problem that I am not able to solve, he is the first person I turn into. We have successfully prepared functional Janus particles and assembled them into interesting structures. I often visit his house in Cambridge and have 'hotpot' together with other group members, and yes, cannot remember much afterwards. He is my colleague who became a father, and it's nice to see her daughter grow up from a baby. Hope he would enjoy his time in Cambridge after we leave. Then, Yuzheng, (Dr.zheng, others call him Danial), has been one of my best colleagues and friends. He is an expert in polymer science, and that's how I have learned and applied ARTP, RAFT to my projects. We both like to playing basketball and watching NBA, he is really good player. We have a lot of enjoyable conversations, no matter when we were have working lunch in the tea room or working late at night. I have learned so much from him, not just about doing research. Now he has moved out from research and become a consultant in McKinsey. I feel very proud of him and wish him all the best in his career. Fifth, Dr. Ji, joined the group in my second year. He is a very hard working and talent person, as a chemist. Every time, I went back to the lab at night, I always saw him working either in the office or in the lab. He helped me a lot on proof-reading my CPGS report, multiple manuscripts etc. He also gives me many suggestions about my future plan. It is really nice to see both of us have developed some interesting materials and open some new directions in our group, on supramolecular bio-inspired materials. Sixth, Chi Hu, now Dr. Hu, I enjoyed the time we had in my first group winter school to Poland. Now even she is not in Cambridge, she gives me a lot of help through 'wechat' on finding jobs. Next, my so-called 'juniors' xiaohe and chenyan, I want to thank these two people. Whenever I need help in/outside the lab, they are always helpful. I have enjoyed the research we have done and the time we spent in Cambridge. I wish they have a productive year and a successful PhD. Additionally, I want to thank Darshil, (Dr. Shah) from the department of architecture. He is an excellent scientist in fiber and material science. We have intensive collaboration in the last two

years, we have developed a brand-new way of making fibers, like spiders. He helped me to collect and analyse all the testing results from over three hundreds of fiber samples. We have been through a lot of disappointing moments together in order to publish our work, but we comfort each other all the time and never give up to try it one more time. It is nice to see our work being highlighted in Cam News, and I enjoyed the time when we were interviewed. I also want to thank the supervisor of my collaborators, Prof. Michael Ramage for the support and suggestion on our fiber project, Prof. Chris Abell for the support on the colloidal particles project and giving access to most equipments in his lab and Mrs Catherine for the considerable conversation and encouraging me to become a good scientist. Then, I want to thank Matt for helping me to learn about rheology, Magda for being a very nice lab buddy and sharing some very useful information with me on finding jobs, Dominique for proof reading my manuscript and answering my questions on rheology, kamil for my first taste of vodaka in Poland, Alex for teaching me climbing, Qifeng for a very nice trip we had in Disney Land, Dr Roger and Dr. Jing for letting me work with you on developing capsules, Dr. David for the help on the peptide synthesis, and great confession on Chinese food as well as Cantonese.

In addition, I want to thank all the support staff in the lab, it is a honour for me to meet all three secretaries, (Catherine, Glenda and Ishita), three lab technicians (Allen, Athen and Matt) and the new lab manager Elisabetta. They are incredibly helpful and so crucial to keep the lab operating properly on day-to-day basis.

Lastly, I would like to thank my parents as always, for the unlimited support far away from China. They give me the opportunity to peruse my study in the UK, and give me the freedom to choose what I want to do. We get together less than 20 days every year, I love you and miss you both every single time in the UK.

List of Publications

Publication

- **Wu, Y.**; Yu, Z.*; Liu, J.; Pambos, O. J.; Abell, C.; O. A.* "Compartmentalised supramolecular self-assembly of supra-colloids," *submitted*.

- **Wu, Y.**; Shah, D. U.; Wang, B.; Ramage, M. H.; Scherman, O. A.* "Biomimetic suprecontracted fibre", *submitted*.

- **Wu, Y.**‡; Shah, D. U.‡; Liu, C.; Yu, Z.; Liu, J.; Ren, X.; Rowland, M. J.; Abell, C.; Ramage, M. H.; Scherman, O. A.* "Bioinspired supramolecular fibers drawn from a multi-phase self-assembled hydrogel", ***Proc. Natl. Acad. Sci. U.S.A.***, doi: 10.1073/pnas.1705380114

- Wu, G.; Olesinska, M.; **Wu, Y.**; Matak-Vinkovic, D.; Scherman, O.A.* "Mining 2: 2 Complexes from 1: 1 Stoichiometry: Formation of Cucurbit [8] uril-Diarylviologen Quaternary Complexes Favored by Electron-Donating Substituents" ***J. Am. Chem. Soc.***, **2017** 139, 3202.

- Liu, C.; Xiang, G.; **Wu, Y**.; Barrow, S. J.; Rowland, M. J.; Clarke, D. E.; Wu G.; Scherman, O. A.* "Hybrid organic–inorganic supramolecular hydrogel reinforced with CePO4 nanowires", ***Polym. Chem.***, **2016**, 7, 6485.

- Ren, X.; **Wu, Y.**; Clarke, D. E.; Liu, J.; Wu G.; Scherman, O. A.*; "Surface-Bound Cucurbit[8]uril Catenanes on Magnetic Nanoparticles Exhibiting Molecular Recognition", ***Chem. Asian J.***, **2016**, 11, 2382.

- Yu, Z.; Zheng, Y.; Parker, R. M.; Lan, Y.; **Wu, Y.**; Coulston, R. J.; Zhang, J.; Scherman, O. A.*; Abell, C.* "Microfluidic Droplet-Facilitated Hierarchical Assembly for Dual

Cargo Loading and Synergistic Delivery", ***ACS Appl. Mater. Interfaces***, **2016**, 8, 8811.

- Xu, X.; Tian, F.; Liu, X.; Parker, R. M.; Lan, Y.; **Wu, Y.**; Yu, Z.; Scherman, O. A.*; Abell C. "Supracolloidal Architectures Self-Assembled in Microdroplets", **Chem. Eur. J.**, **2015**, 44, 15516.

- **Wu, Y.**; Lan, Y.; Liu, J.; Scherman, O. A.* "Catalytic polymeric nanocomposites via cucurbit[n]uril host-guest interactions", ***Nanoscale***, **2015**, 7, 13416.

- Zheng, Y., Yu, Z.; Parker, R. M.; **Wu, Y.**; Abell C.*; Scherman, O. A.* "Interfacial assembly of dendritic microcapsules with host-guest chemistry", ***Nat Commun.***, **2014**, 5, 5772.

- Lan, Y.‡; **Wu, Y.**‡; Karas, A.; Scherman, O. A.* "Photoresponsive Hybrid Raspberry-Like Colloids Based on Cucurbit[8]uril Host-Guest Interactions", ***Angew. Chem.***, **2014**, 53, 2166.

  ‡These authors contributed equally to this work

Chapter 1

Introduction

1.1 Chemistry Beyond the Molecules

Chemistry lies in the middle of physics and biology as it deals with the ordering and rearrangement of atoms at the molecular level,[1] rather than the fundamental subatomic nature of matter or its animation in macroscopic time dependent structures. Regardless of the interactions between atoms that enables the formation of molecules, the study on interactions (non-covalent) between molecules is crucial to understand many fundamental biological processes within living systems, thereby stimulating the design of advanced functional materials. From the lock-and-key principle proposed by Emil Fischer in 1873 to the hydrogen bonding theory by Linus Pauling in 1939,[2] until Lehn, who was awarded the Nobel Prize in 1987, defined 'chemistry beyond the molecule',[3] supramolecular chemistry is growing extremely rapidly with remarkable contributions to the areas of material technology,[4–8] catalysis[3,9–11] and medicine chemistry.[12–16]

Supramolecular chemistry focuses on the interactions between molecules, and molecular self-assembly is defined as the autonomous organization of components into patterns or structures from a disordered systems without human intervention, and widely used in many disciplines.[17–19] Different from the chemical bonds such as covalent bond, supramolecular interactions, or non-covalent interactions, are much weaker in strength (less than 350 kJ/mol) on account of a larger length-scale with a dimension of 1-100 nm. A range of non-covalent interactions were discovered with different strength. Among

these ion-ion interactions resulting from columbic forces between opposite charges are the strongest in strength. Hydrogen bonding originally explains why water has a much higher boiling point than other group 16 hydrogen derivatives. It is also responsible for the 3 dimensional assembly of DNA on account of its specific and directional hydrogen bonding within complementary nuclei base pairs (Figure 1.1). Table 1.1 summaries typical non-covalent interactions that are substantial in rationally designed self-assemblies.[20,21]

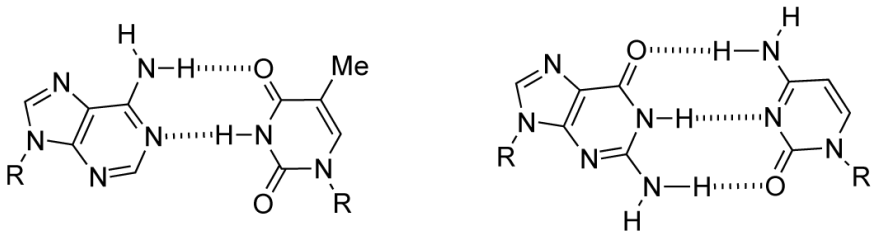

Figure 1.1: Hydrogen bonding model between DNA base pairs: adenine and thymine, guanine and cytosine.

	ion-ion interactions	ion-dipole interactions	dipole-dipole interactions	hydrogen bonding
Energy (kJ mol^{-1})	100-350	50-200	5-50	4-120
	cation-π interactions	π-π interactions	van der waals forces	hydrophobic-hydrophilic effects
Energy (kJ mol^{-1})	5-80	0-50	0-5/variable	-

Table 1.1: Non-covalent interactions and their associate strengths.[20,21]

1.1.1 Macrocyclic Host-Guest Complexation

Macrocyclic host-guest complexation is a typical process of molecular self-assembly where molecules bind selectively through a combination of supramolecular interactions. A variety of macrocyclic host molecules has been synthesized such as cyclodextrins,[22] calixarenes,[23] cucurbiturils[24] and porphyrins.[25] In these cases, the 'host' usually has dis-

tinctive features externally and internally that could interact with the solvent and the 'guest' respectively. The molecular inclusion complexation is a dynamic process where molecules associate/dissociate rapidly. The binding constant is a measure of the rates between these two processes that is dependent on the molecules. A hydrophobic guest prefers to enter a hydrophobic cavity in an aqueous media to eliminate any contact with water molecules. In addition to this, molecule size and shape, solvent, temperature would also determine its binding constant. For example, studies has shown that crown ether is able to stabilize positively charged ions with K_{eq} values between 10^2 and 10^5 M^{-1}.[26]

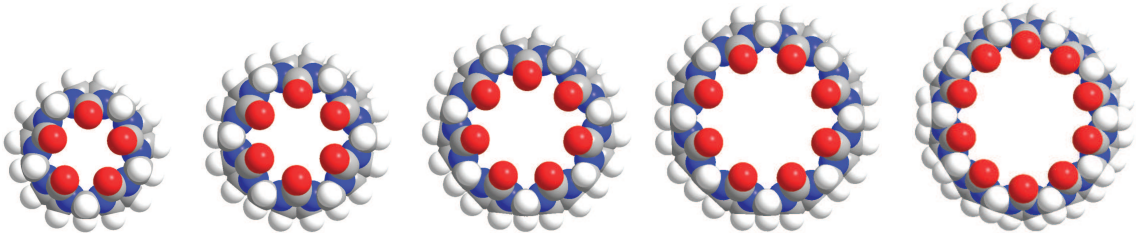

Figure 1.2: Molecular structure of of CB[n] homologues CB[5]-CB[8],CB[10].[24]

Cucurbit[n]urils (CB[n]s) are a class of macrocyclic oligomers based on glycoluril monomers as repeating units, their names were from the resemblance of pumpkins in shape.[27–30] They are commonly written as cucurbit[n]uril, where n is the number of glycoluril units in the host molecules (Figure 1.2). Cucurbit[6]uril was first synthesized in 1905 by Behrend,[31] by condensing glycoluril with formaldehyde (Figure 1.3).[27,32] However, its structure was not elucidated until 1981 when Mock[28] and co-works used a range of characterization techniques, and reported that macrocylic structure contained six glycolurils and twelve methylene bridges. In the following decades, other homologues (CB[5,7,8]) were discovered and isolated by Kim and Day.[33–35] Then in 2005, Isaacs and co-workers[24] successfully isolated a new homologue CB[10] from a complex of CB[5] inside CB[10]. In the mean time, singly and multiply substituted CB[n]s have been synthesized in order to modify their solubility in different solvents and provide precursor for further functionalization. Substituted CB[n]s can be obtained from two routes. One approach starts from the modification of glycoluril units, followed by the condensation in hydrochloric

acid.[36] This method has limited yield and most homologues are CB[5] with a very small amount of CB[6]. An alternative method is to directly functionalize pure CB[n]s through a direct oxidation reaction. By optimising the reaction and purification procedures, monofunctional CB[n]s can be obtained, which can be easily modified to desired functional groups with good solubility in common solvents.[37,38] In 2003, Kim *et al.* successfully introduced hydroxyl moieties at the equatorial positions of CB[6], which was used to study a dye-labelled pattern on glass substrate.[39]

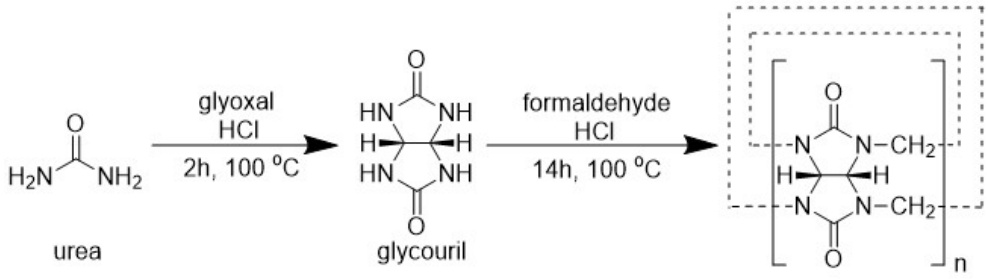

Figure 1.3: Synthetic scheme of CB[n]s homologues.

The structural dimension of CB[n] are shown in Figure 1.4.[40] The height of a single glycouril is fixed, and all CB[n] homologues share a common depth of 9.1 Å. Increasing glycoluril units from CB[5] to CB[10] leads to an increase in cavity diameter from 4.4 to 12.6 Å, and portal size from 2.4 to 11 Å. Therefore, the resulting cavity volumes vary from 83 to 870Å^3, respectively (Table 1.2). This results in discernible features in the host-guest chemistry in different CB[n] homologues. Interestingly, the water solubility of CB[n]s varies across the family in an odd–even fashion, presumably on account of the altered arrangement of H-bonding water molecules between the homologues in aqueous solution. CB[5] and CB[7] show relatively high solubilities of 20–30 mM in neutral water, whereas CB[6] and CB[8] have much lower solubility of 0.018 mM and less than 0.01 mM, respectively. All CB[n]s are soluble in acidic pH or aqueous solutions of alkali metals on account of protonation or coordination of the metal ions to the carbonyl oxygen atoms. In addition, CB[n] are insoluble in organic solvents (less than 10^{-5}), hence CB[n] complexes have mainly been studied in an aqueous phase.

The binding activity of CB[n] has been extensively studied.[41–43] It is a well-known concept that combines the primary hydrophobic interaction and the ion-dipole interac-

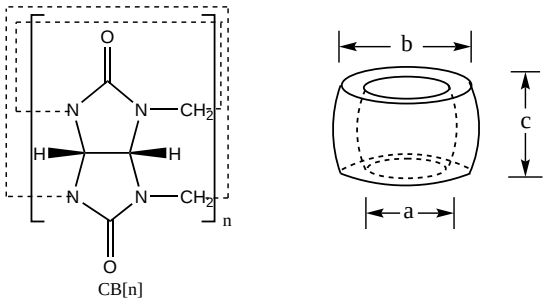

Figure 1.4: Chemical framework and dimensional structure of CB[n].[40]

CB[n]	a [Å]	b [Å]	c [Å]	V [Å]	S_{H_2O} [mM]	pK_a
CB[5]	2.4	4.4	9.1	82	20-30	-
CB[6]	3.9	5.8	9.1	164	0.018	3.02
CB[7]	5.4	7.3	9.1	279	20-30	-
CB[8]	6.9	8.8	9.1	479	$<$0.01	-
CB[10]	9.0-11.0	10.7-12.6	9.1	870	-	-

Table 1.2: Dimensions and solubility of CB[n] homologues.[40]
a: portal diameter; b: outer cavity diameter;
c: height of torus; V: volume of cavity; S_{H_2O}: solubility in water.

tions between the guest molecule and CB[n]s (Figure 1.5). More recently, this favourable binding event has been studied from the energy point of view, which attributes to the release the 'high-energy' water molecules upon inclusion of nonpolar organic residues. In another word, the 'guest' entering the CB[n] leads to an energy loss from the reconstruction of the hydrogen bonding network. This is on account of the occupied 'guest' and the release of the trapped water molecules inside the CB[n]s cavity that further promotes the net enthalpy from the system (Figure 1.6).[44,45] The negative electrostatic potential of the carbonyl rims explains the preference of CB[n] towards cationic species as guest molecules. The overall dimension of the CB[n]s on account of different number of repeating unit determines their molecular recognition properties. Specifically, CB[5], the smallest analogue in the CB[n] family, only binds with protons, metal and ammonium ions, gas

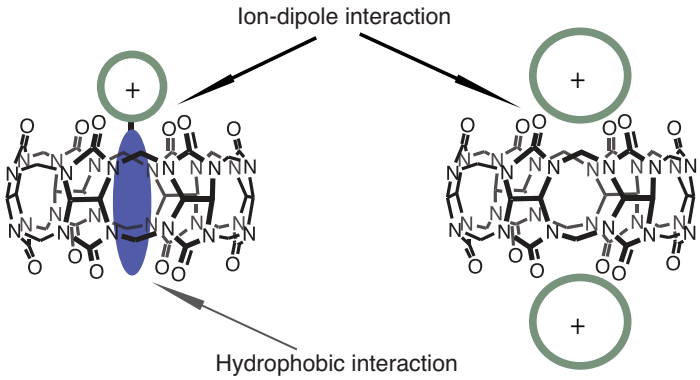

Figure 1.5: Two major types of interactions of CB[n] with guest molecules.[41,42]

molecules (Kr, Xe, N_2, O_2, Ar, N_2O, CO, CO_2) and solvent molecules (methanol and acetonitrile).[36,38,46] CB[6], with a larger cavity volume, is able to encapsulate aliphatic guests with alkyl chains such as ω -amino acids and ω -amino alcohols, aliphatic alcohols, acids and nitriles, alkyl ammonium ions, and poly(ethylene glycols) (PEG).[47–49] A highly sensitive fluorescence-based method was reported in 2011 for the quantification of volatile hydrocarbon binding with CB[6].[50] CB[7] has been reported to bind with a variety of positively charged compounds such as adamantane amine and bicyclooctanes.[51–53] In 2005, the formation of inclusion complexes between CB[7] and ferrocene and its derivatives has been investigated by Kim and co-workers.[51,54] The NMR spectroscopic, calorimetric and electrochemical data reveal that the surveyed ferrocene derivatives can form very stable inclusion complexes with the CB[7] host. While these complexes show thermodynamic association constants in the range of 10^9-10^{13} M^{-1}, much higher than the same ferrocene derivatives with cyclodextrin.

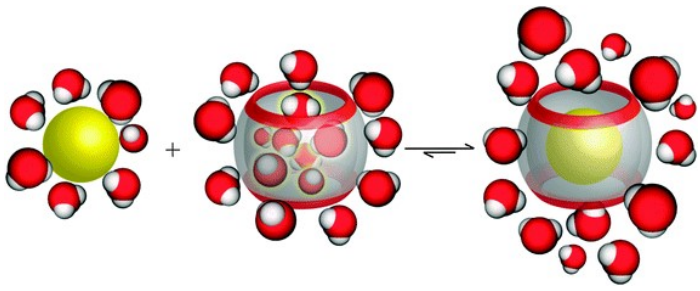

Figure 1.6: Schematic illustration of the release of high-energy water molecules from the CB7 cavity upon binding of a hydrophobic guest. Adapted from reference.[44]

With further increased cavity volume, CB[8] (479 $Å^3$) shows remarkable binding affin-

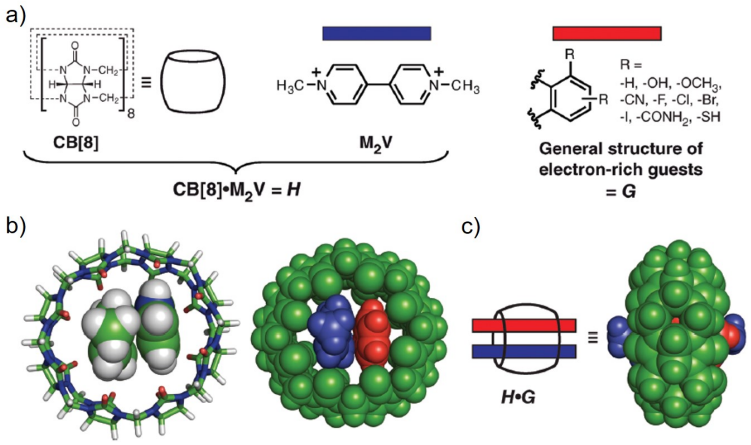

Figure 1.7: a) Cucurbit[8]uril (CB[8]) can accommodate sequentially the electron-poor M_2V and a multitude of electron-rich aromatic guests, **G**. b) The heteroinclusion complex of CB[8], M_2V (MV^{2+}) , and indole is shown as 3D renderings. c) Side view of the complex shows indole (red) well-encapsulated inside of **H**.

ities towards positively charged and relatively larger guests such as adamantane derivatives, cyclen and long alkylammonium aliphatic chains. More interestingly, different form CB[5-7], CB[8] can accommodate two guest molecules simultaneously forming strong yet dynamic ternary complexes.[55–57] For example, an electron-deficient first guest methyl viologen (MV^{2+}) and an electron-rich second guest 2-naphthol (Np) can form a stable 1:1:1 ternary complex (MV^{2+}/Np/CB[8]) with CB[8], with a total binding constant up to 10^{12} M^{-2} in aqueous buffer solution. The guest molecules aligned in parallel orientation inside the CB[8] cavity as shown in the computational indole model (Figure 1.7b-c). Other complementary guest molecules also show high affinities towards CB[8] with interesting binding features. For instance, for a 1:1:1 ternary complex with methyl viologen (MV^{2+}) and *trans*-azobenzene (or its derivatives) as a second guest, the complex shows a reversible de-assembly feature under UV light at 365 nm which causes the transformation of *trans* to *cis* conformation. In addition, CB[8] could form a 2:1 complex with two phenylalanine molecules, with a binding constant up to 10^{11} M^{-2}. The dynamic ternary complexes of CB[8] can be dissociated by introducing a competitive guest that has a higher binding constant. For example, adamantane amine (ADA) can bind with CB[8] with a binding constant K_{eq} = 10^{12} M^{-2}, so ADA would dissociate the complexes and release the encapsulated guests from CB[8].

1.1.2 Supramolecular 'hand-cuff' Based on CB[*n*]s

The interesting binding features of CB[*n*]s provide a promising platform for fabricating supramolecular self-assemblies, where CB[*n*]s, primarily CB[8], could act as a supramolecular 'hand-cuff' to join two synthetically designed units together, creating new functional materials with emergent properties. This binding motif has been shown in complexing small molecules,[58–60] functional polymers,[61–63] nano particles[64] and surfaces.[65] In 2010, Scherman and co-workers reported the high-water content supramoleuclar hydrogels assembled from functional polymers and CB[8].[66] Commercially available poly(vinyl alcohol) (PVA) and cellulose derivatives (hydroxyethyl cellulose, HEC) were functionalised with MV^{2+} and NP, respectively. The addition of CB[8] induces the dynamic crosslinks between two polymers on account of the formation of the ternary complexes. The resulting hydrogel exhibits high mechanical tenability and good self-healing properties, which is promising for injectable soft-materials. The self-assembly between polymers *via* CB[8] can also take place at water/oil interfaces.[63] In 2014, the fabrication of microcapsules was reported where complementary functionalized hydrophilic and hydrophobic copolymers were assembled at the water/chloroform interface of a microfluidic droplet, by forming a robust ternary host–guest complex with CB[8] (Figure 1.9). These template free, interfacially assembled microcapsules are monodisperse in size and composition, with a high cargo encapsulation efficiency, which extends the range of potential application into new areas, such as drug delivery. Importantly, these interfacially assembled bilayer microcapsules afford a unique platform with which one could quantitatively investigate the mechanism and kinetics of self-assembly at liquid–liquid or soft matter interfaces, which is of great relevance in all biological systems.

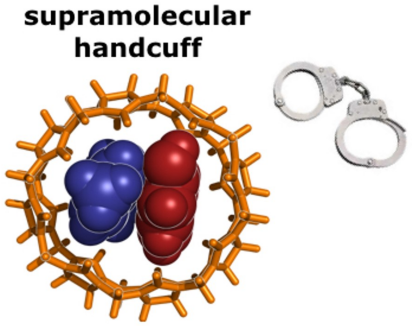

Figure 1.8: CB[8] as a 'hand-cuff'.

Substrates with patterned nano-structures are crucial in the development of smart surfaces on account of its controlled roughness and interfacical functions.[65] In 2010,

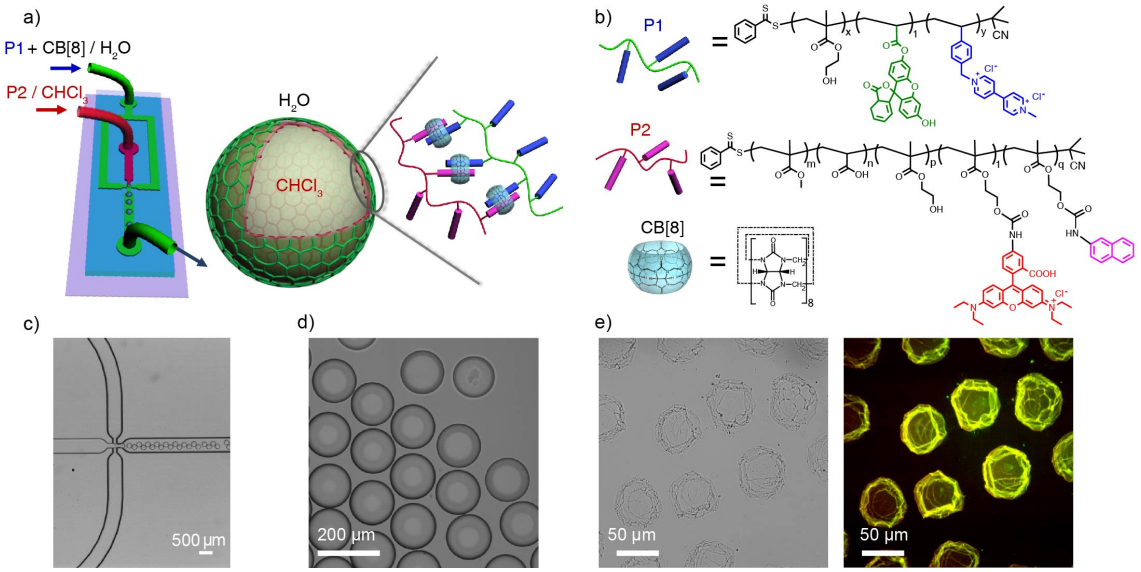

Figure 1.9: a) Schematic representation of the microdroplet generation process using a microfluidic flow-focussing device, where an aqueous continuous phase containing CB[8] and copolymer **P1** (functionalized with MV^{2+} and FOA: fluorescein-o-methacrylate) intersects an immiscible chloroform phase containing copolymer **P2** (functionalized with Np and Rhodamine, at a flow-focussing microchannel junction to form a periodic flow of oil-in-water microdroplets. b) The chemical structures of hydrophilic poly(HEMA-*co*-StMV-*co*-FOA), **P1**; hydrophobic poly(MMA-*co*-AA-*co*-HEMA-NP), **P2** and CB[8]. c) Micrograph of oil-in-water microdroplets generated at the microfluidic flow-focussing channel junction. d) The high monodispersity of the formed microdroplets is demonstrated by the narrow size distribution (D = 102.4 ± 0.5 mm). e) Bright field (left) and fluorescence (right) images of microcapsules formed after evaporation of the chloroform droplet, resulting in a collapsed capsule-like structure. Adapted from reference.[63]

hierarchical supramolecular structures in the formation of colloidal arrays was reported by immobilizing monodispersed naphthalene-functionalized colloids onto Au substrates bearing viologen moieties using the macrocyclic host molecule cucurbit[8]uril as a supramolecular "handcuff" (Figrue 1.10). This facile supramolecular approach is believed to facilitate the progress in the field of smart materials and wet nanotechnology, and leads to the preparation of controlled reversible architectures on surfaces. In addition, the materials serve as a new class self-assembled surface bound structures that are valuable to areas ranging from condensed matter physics to photonics.

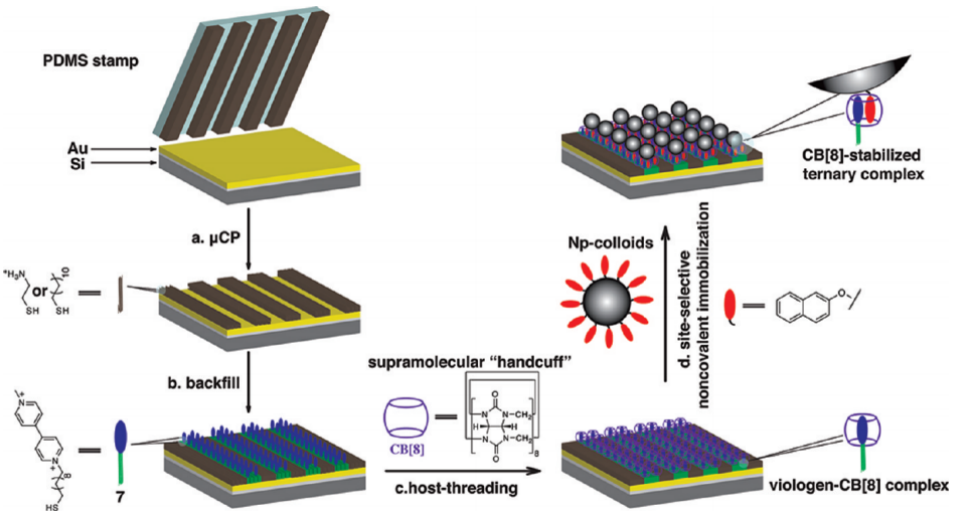

Figure 1.10: (a) Micro-contact printing a Au substrate by gently placing a PDMS stamp "linked" by protecting thiol for 30 s; (b) backfilling the viologendecanethiol by immersing the partially protected Au substrate in an EtOH solution of viologendecanethiol (**7**) for 2 min; (c) threading the macrocyclic host molecule as a supramolecular "handcuff" by immersing the Au substrate in a supersaturated CB[8] aqueous suspension for 5 min; (d) immobilizing the Np-colloids onto specific sites by immersing the Au substrate into an aqueous suspension of Np-colloids for 30 s. Adapted from reference.[65]

1.2 Supramolecular Colloidal Self-Assemblies

An early example of artificial colloids can be traced back to ancient times, when the lycurgus cup (4^{th}-century Roman glass cage cup) was fabricated. Depending on the location of the light source, the glass cup can display different colors, on account of the existence of small gold particles in the colourless glass (Figure 1.11).[67] Yet this discovery was not well interpreted until hundreds of years later. In nineteenth-century, Thomas Garham pioneered the work in dialysis and the diffusion of gases. These studies were foundational in the filed of colloid chemistry. Then the term "colloid science" was defined by Wolfgang Ostwald in 1927, which he explained as 'the world of neglected dimensions'.[68] Generally, the colloidal domain is characterized by the dimensions in the range from several nanometers to micrometers (Figure 1.12).[69] Particles were microscopically dispersed in another medium such as milk, smoke and cream. Research in colloidal science has grown rapidly with unmerous applications in the fields of catalyst, food chemistry and biomaterials.[70,71] Since in the nanometer-size regime, the properties of materials, such as optical, electric, magnetic and mechanical, can be tuned merely by varying their physical sizes, creating unique phenomena found in neither bulk nor molecular systems.

Figure 1.11: Lycurgus cup in Roman times.[67]

The Interaction betweens colloidal particles are crucial in terms of their stability and assembling activities.[72,73] On the one hand, the stabilisation of colloids suggests particles remaining suspended in solution at equilibrium. For example, milk expires due to the aggregation of the colloidal butterfat. There exist various types of forces between colloids including van der Waals forces, double layer interactions (electrostatic repulsion) and steric interactions. The Van der Waals force is usually an attractive force that varies with the distance between particles. Electrostatic attractions arises form the particles

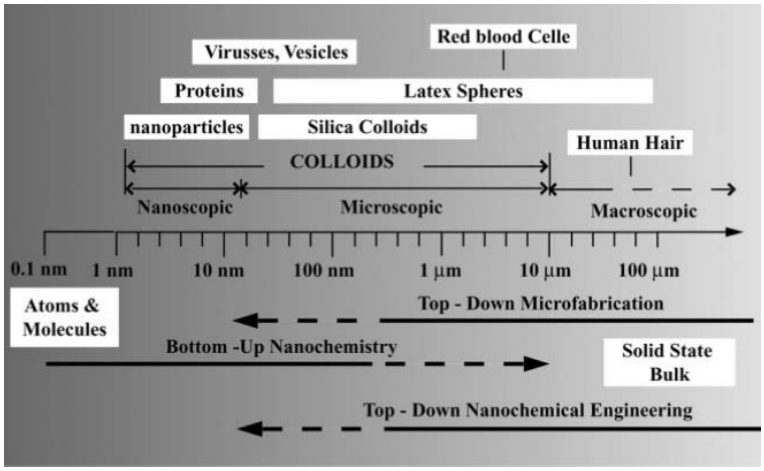

Figure 1.12: Overview of typical dimension ranges of colloids, together with some representative colloidal systems.[69]

with opposite charges. Double layer interactions is likely a repulsive force that occurs from the double layer of charged colloids. A well-known theory called the DLVO theory (Named after Derjaguin, Landau, Verwey and Overbeek) explains the aggregation of charged particles in aqueous medium, it combines the effects of the van der Waals and double layer interaction as shown in Figure 1.13.[74] When two particles approach closer, the electrostatic repulsion starts to dominate over van der Waals forces and generate a energy barrier that prevents particles from 'bumping' into together. Once the energy has been surpassed, agglomeration occurs.

In addition, steric interactions could be either attractive or repulsive on account of the surface chemistry of colloids and the DLVO theory dose not apply here. For example, polymer-grafted surfaces can modulate interparticle forces, producing forces and aggregating the particles.

On the other hand, the assembly of colloidal particles remains a key challenge in material chemistry and technology on account of its structural hierarchies built from mesoscopic length scale (nm and μm).[75–77] Its potential has shown widespread interests[78] in the fields of fundamental physics,[19,79,80] material science,[81,82] energy transport[71] and biosensing.[72,83,84] Conventionally, mesoscopic structures are fabricated by the strategy called 'top-down',[69] where the matter is sheared from larger to smaller length scales, such as shaking, high frequency shearing. While the 'bottom-up' approach focuses on assem-

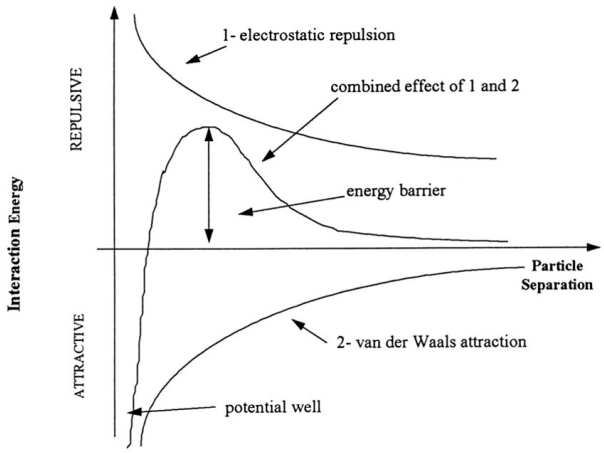

Figure 1.13: Schematic plot of a typical double layer repulsion between charged colloidal spheres (top), of the Van der Waals attraction (bottom) and their sum, which is the DLVO interaction potential. Adapted from reference.[74]

bling colloidal structures as building blocks from smaller dimensions (molecular level or nano-level) to macroscopic structures. The main advantages of 'bottom-up' methods compared to 'top-down' methods include low-energy input, spontaneous process and the hierarchical order of resulted materials with high levels of control.[85]

In 2003, Xia and co-workers reported the self-assembly of spherical colloids into helical chains (Figure 1.14).[86] Physical confinement was applied by V-grooves and capillary force to assemble mesoscale, achiral building blocks (spherical colloids) into helical chains. The handedness of these helical structures could be controlled by changing the relative orientation of the capillary force with respect to the longitudinal axis of the V-grooves. Moreover, the physical constraint provided by the walls of these grooves can drive monodisperse spherical colloids to assemble into helical chains (Figure 1.14 e). Another example illustrates the self-assembly of colloidal particles based on complementary shapes. Figure 1.15 indicates the colloidal assemblies mediated by Fischer's lock-and-key principle.[87] One of the colloidal spheres was applied as a key and the other monodisperse colloidal particles with a spherical cavity acted as locks that bind spontaneously and reversibly *via* the depletion interaction. The lock-and-key binding is specific because it is controlled by the close match between the size of a spherical colloidal key particle and the radius of the spherical cavity of the lock particle.[88] The composite assemblies have the

unique features of having flexible bonds, that allow the production of flexible dimeric, trimeric and tetrameric colloidal molecules as well as more complex colloidal polymers.[89]

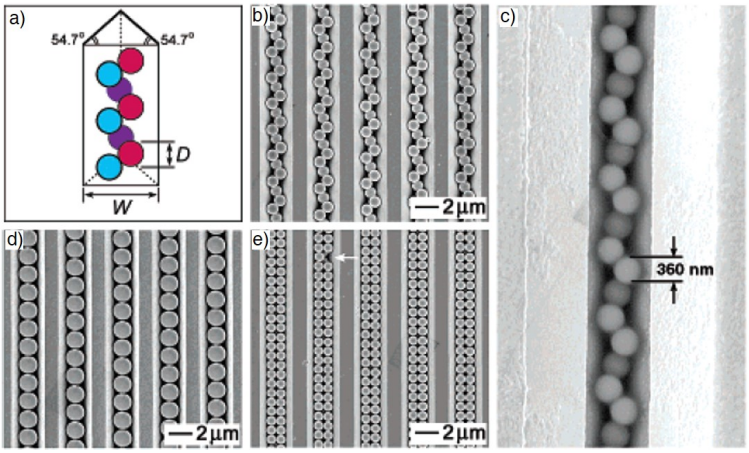

Figure 1.14: Self-assembly of spherical colloids in V-shaped grooves. a) Schematic illustration showing the formation of a helical structure. b-d) SEM images showing three typical chainlike aggregates assembled in 2D arrays of V-grooves that had W = 2.72 μm. The polystyrene beads were 1.0, 1.6, and 0.8 μm in diameter, respectively. Helical structures only formed at an appropriate ratio between W and D. The arrow in d) indicates a defect, where one can clearly see the colloids underneath the top layer of the structure. e) A helical chain of 360-nm silica colloids that was assembled in a V-groove whose dimension had been reduced by forming hydrophobic thiolate monolayers on gold films prepared by shadow sputtering. Adapted from reference.[86]

Apart from template or comlementary shapes assisted strategies, directional and specific supramolecular interactions have been applied in assembling colloidal building blocks in aqueous media,[90] such as van der Waals forces, electrostatic interactions,[91] steric interactions.[92] Essentially, this substantially relies on the surface chemistry of colloidal particles (or interface). Some colloidal particles acquire certain surface features that could be applied to their self-assembly, such as polystyrene nanoparticles with the hydrophobic colloidal surface, silica nanoparticles with a negative surface potential. In addition, the decoration of functional groups affords colloids with more interesting surface features that provides new opportunities for emerging colloidal assemblies. These functional groups vary from small molecules (that could tune the surface potential) to oligomers (such as DNA, peptides) and macromolecules (polymer brushes) etc. For example, Mirkin *et al.* reported using DNA chains as linkers between nanoparticles to build a revers-

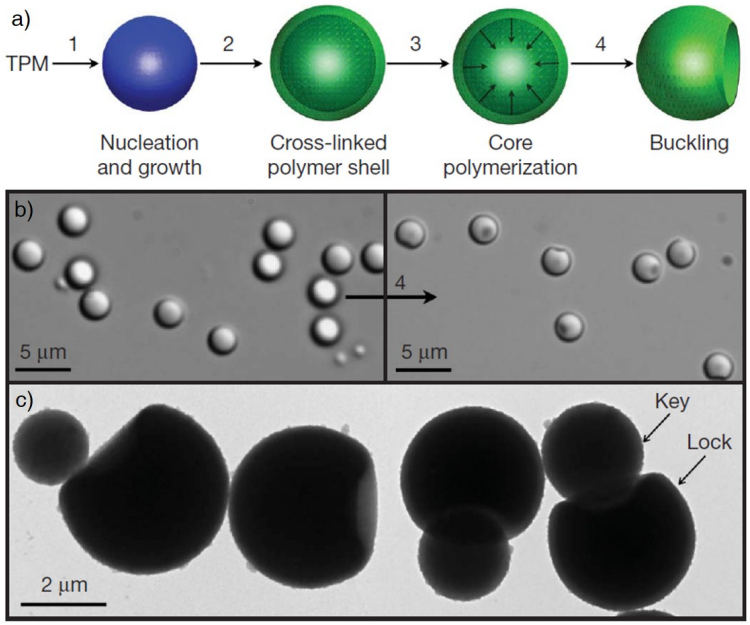

Figure 1.15: a) Diagram showing the synthetic steps involved in the preparation of particles with well-defined spherical cavities. Monodisperse silicon oil droplets are (1) nucleated from a homogeneous solution of hydrolysed 3-methacryloxypropyl trimethoxysilane monomer, and (2) encapsulated into cross-linked polymer shells. The liquid core (3) contracts when polymerized and (4) drives a controlled shell buckling that forms spherical cavities. b) This last step is easily followed by optical microscopy. After polymerization, cavities are visible as darker spots on the particles surfaces. c) The complementary fit between the locks and the spherical keys (here silica), is clearly visible in this transmission electron microscope image. Adapted from reference.[87]

ible DNA-mediated assembly of gold nanoparticles (Figure 1.16).[93] This method involves attaching to the surfaces of two batches of gold nanoparticles with non-complmentary DNA strands through end-functionlised thiols. When the solution of oligouncleotide duplex that are complementary to those two grafted sequences are introduced, the functionlised gold nanoparticles self-assemble. In addition, the thermal denaturation of the DNA strands enable the disassembly of gold nanoparticles indicating controllable reversibility.

More importantly, supramolecular colloidal assemblies enables versatile categories of building blocks assembling together to achieve the fabrication of emerging hybrid materials.[94] Apart from the colloidal crystals prepared from uniformly functionalised particles,[95] nanocomposites can be fabricated with a hybrid of nano-structured entities that were in-

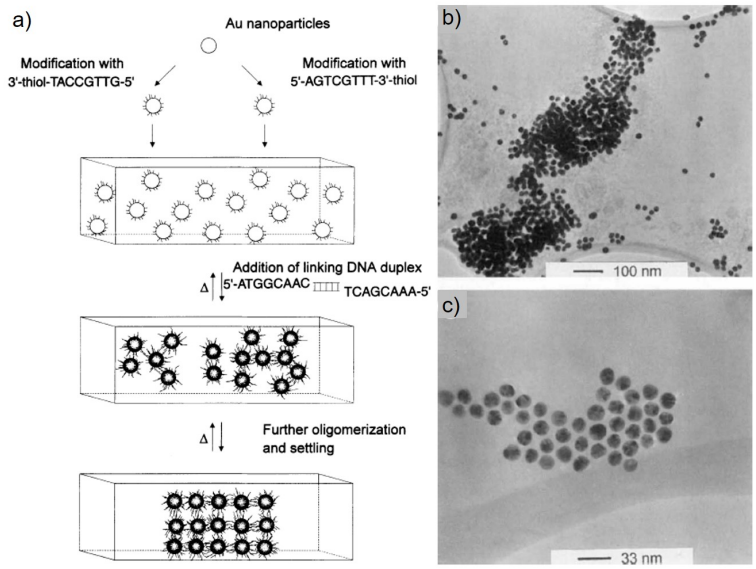

Figure 1.16: a) Scheme showing DNA-based colloidal nanoparticles assembly. TEM images of b) an aggregated DNA/colloid hybrid material; c) a two dimensional colloidal aggregate showing the ordering of the DNA-linked Au nanoparticles. Adapted from reference.[93]

compatible before surface functionalisation.[96,97] For instance, metallic nanoparticles stabilized by functional polymers, carbon nanotubes delivering an anti-cancer drug and gold nanoparticle assemblies demonstrating enhanced Raman spectroscopy.[96,98] The resulting nanocomposites show combined properties from each component. Over the past decades, research on supramolecular colloidal assemblies has brought remarkable interests to the fields including catalysis, biomaterials,[84] bionics,[82] nanoscience,[99,100] electronics,[71] photonics and green energy resources.[101,102]

1.3 Aim

The macrocyclic cucurbit[n]urils (supramolecular 'hand-cuff') have been exploited with interesting supramolecular binding motifs. Essentially, this can be elaborately applied into the self-assembly between colloidal particles and different functional nano-materials. Therefore, in the following chapters, we investigate the preparation of hybrid supramolecular self-assemblies mediated by CB[n]s host-guest interactions at colloidal interfaces.

Chapter 2 studies the hybrid raspberry-like nano-structures *via* CB[8] host-guest complexation, where the inorganic functional silica nanoparticles serve as the core and the soft polymeric colloids serve as the corona. This facile supramolecular method provides a platform for the synthesis of colloids with topological complexity in material chemistry.

Chapter 3 explores a supramolecular approach to immobilize meta-stable metallic nanoparticles on targeted colloidal substrate using CB[7], the formed nanocomposites is expected to show great potential in heterogeneous catalysis.

Chapter 4 focuses on self-assembly of suprastructures with complexed topology. Functional nanoparticles are complexed to the Janus particles selectively and asymmetrically. A facile approach was employed that nanoparticles were assembled in the compartmental microdroplets to achieve high level of control.

Chapter 5 studies the influence of nano-objects in a supramolecular polymer-network mediated *via* CB[8] host-guest chemistry. Supramolecular polymer-colloidal hydrogel (SPCH) was fabricated comprising 98 wt% water that can be drawn into uniformed fibers. The fibers exhibits a unique combination of stiffness and high damping capacity. This hydrogel represents a new class of hybrid supramolecular composites, opening a window into fiber technology through low-energy manufacturing.

Chapter 6 further explores the fiber network and introduce a covalent network into the fiber polymeric matrix. The resulting hydrogel fiber is showing high resilience in water. More interestingly, the supercontraction behaviour of the fiber is investigated. This resembles spider silk that contracts itself significantly in length at changing humidity, with corresponding variation of mechanical properties.

In the end, a concluding and perspective chapter summarizes the presented work . It highlights the importance of supramolecular interactions where building blocks are assembled at colloidal interfaces and the great potential of supramolecular materials in the near future.

Chapter 2

Hybrid Raspberry-like Colloids Based on Host-guest Interactions

Hybrid raspberry-like colloids (HRCs) were prepared by employing cucurbit[8]uril (CB[8]) as a supramolecular linker to assemble functional polymeric nanoparticles onto a silica core. The formed HRCs are photoresponsive and can be reversibly disassembled upon light irradiation. This facile supramolecular approach provides a platform for the synthesis of colloids with topological complexity in material chemistry.

This work has been published in the following peer-reviewed journal articles:

- Lan, Y.[‡]; **Wu, Y.**[‡]; Karas, A.; Scherman, O. A.* "Photoresponsive Hybrid Raspberry-Like Colloids Based on Cucurbit[8]uril Host-Guest Interactions", *Angew. Chem.*, **2014**, 53, 2166.

  [‡] These authors contributed equally to this work.

2.1 Introduction

Research on functional polymeric particles has been receiving increasing attention in the past few decades.[103] Functional polymeric particles have been widely applied in the areas of drug-delivery systems,[104] industrial processes[105] and opto-electronics.[106] This is owing to the special properties of polymeric functional particles including their small size and volume, large specific surface area, high diffusibility, stability, uniformity, and great tunability[103] etc. Generally, functional polymeric particles are fabricated using heterogeneous polymerization. Several polymerization methods have been employed such as emulsion polymerization,[107] soap-free emulsion polymerization[108] and suspension polymerization,[109] which allow one to tune the size or other functionalities of the polymeric particles.[103] With the development of synthetic methods and technology, the structure of particles can also be diversified. Porous microspheres,[110] hollow microspheres[111] and core-shell microspheres[112,113] have drawn great attention, not only because of their physicochemical properties, but also their diversified morphology.

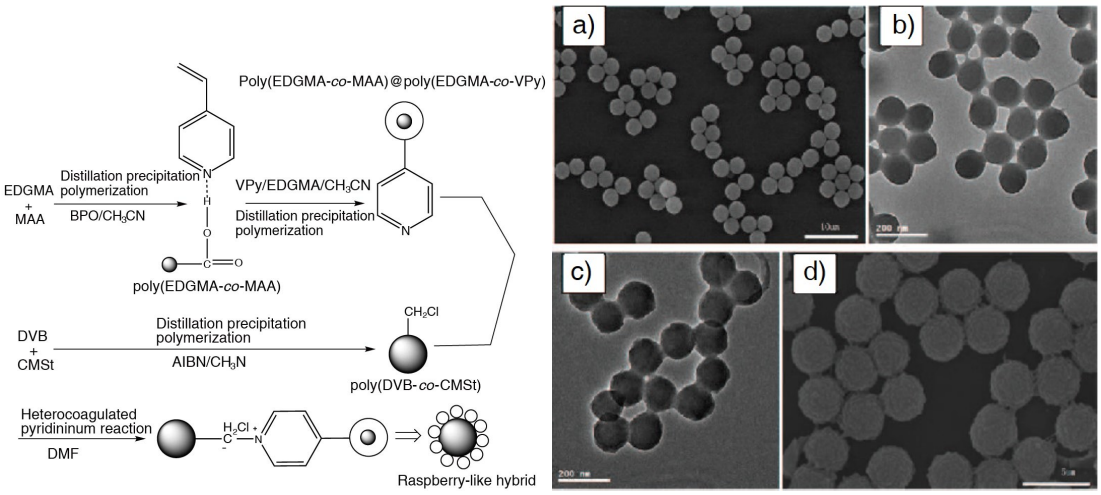

Figure 2.1: Scheme of the preparation of the core-corona polymer hybrids with a raspberry-like structure and morphology of the polymer particles:[114] a) SEM of poly(DVB-*co*-CMSt); b) TEM of poly(EGDMA-*co*-MAA); c) TEM of core-shell poly(EGDMA-*co*-MAA)@poly(EGDMA-co-VPy); d) SEM of core-corona hybrids. Adapted from references.[114]

Raspberry-like particles are one of the structures with higher topological complexity, which many research groups across the world have attempted to fabricate. These are

structures with a large core particle surrounded by a layer of smaller spheres so that the whole object resembles a 'raspberry' fruit. During the past few years, a vast array of different materials have been used to prepare this kind of structure. In particular, hybrid raspberry-like colloids (HRCs) containing different materials in both the core and corona components, are very promising materials, and generate wide applications in super hydrophobic surfaces,[115] optics,[116] UV-shielding materials,[117] hierarchically structured catalysis,[117] etc. Generally, the predominant method for fabricating HRCs is through coagulating corona particles onto the preformed core particles. For example, Wang *et al*[114] demonstrated the synthesis of core-corona polymer HRCs by the heterocoagulated pyridinium reaction shown in Figure 2.1. The linkages between the core and the corona spheres are covalent. However, the synthetic procedures often require multiple steps and harsh conditions, which lead to high complexity in fabrication methods.

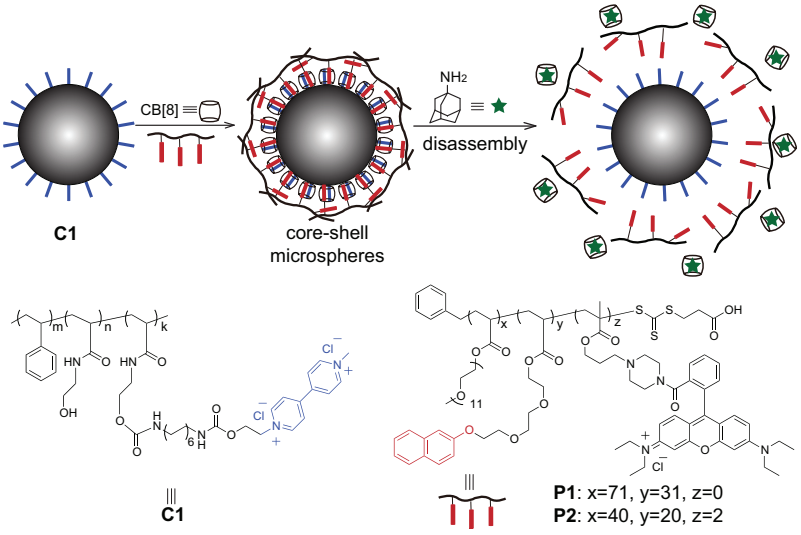

Figure 2.2: Schematic illustration of fabricating core-shell polymeric microspheres *via* CB[8]. Adapted from reference.[99]

On the other hand, supramolecular approaches have been applied to prepare HRCs, in which corona particles are anchored onto the preformed core particles *via* supramolecular interactions including hydrogen bonding, hydrophobic-hydrophilic interactions and electrostatic interactions. These approaches allow for a spontaneous self-assembly process with no additional energy input in aqueous media. Moreover, on account of the

dynamic process, HRCs have the potential to be efficiently dissembled with the addition of an external stimuli. Host-guest interactions of CB[n] have also been demonstrated in assembling functional particles. In 2012, Lan *et al.* successfully prepared core-shell polymeric microspheres by grafting Np-functionalized polymer layer onto the surface of a pre-synthesized MV^{2+} functionalized polymer microsphere.[99] CB[8] was used as a "supramolecular glue" through the formation of ternary complexes of MV^{2+}/Np@CB[8] (Figure 2.2). Molecular-recognition driven self-assembly is a promising technique, which can efficiently afford core-shell polymeric microspheres with various functional shells by specifically recognizing and binding different types of polymers onto the surface of polymeric microspheres. Moreover, the non-covalent nature of the supramolecular interactions provide the possibility of reversible control, meaning that the core-shell polymeric structures can be easily dissembled by addition of a competitive guest.

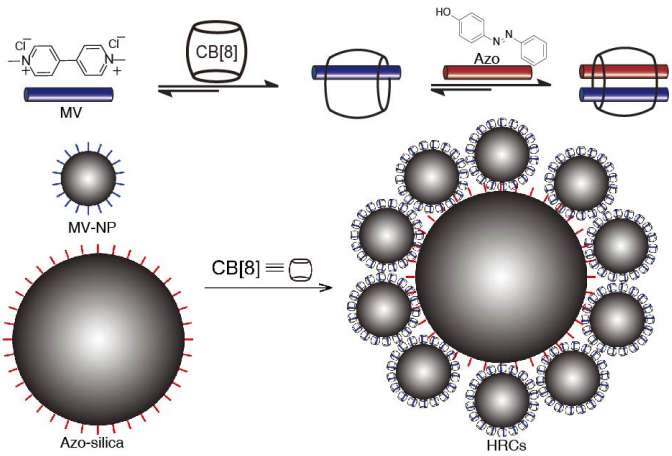

Figure 2.3: Schematic description of fabricating hybrid raspberry-like composites (HRCs).

Inspired by this approach, we report a facile fabrication route for hybrid raspberry-like colloids by taking advantage of the CB[8] mediated host-guest complexation. Corona polymeric microspheres (MV-NP) with MV^{2+} moieties on the surface and functionalized silica particles with pendent azo-benzene moieties were synthesized separately. CB[8] serves as the supramolecular 'handcuff' that encapsulate a MV^{2+} (methyl viologen) guest and an azo-benzene guest on the surface of both microspheres, thereby constructing the hybrid raspberry-like particles (Figure 2.3). In addition, the non-covalent nature of CB[8]

host–guest interactions affords the supramolecular HRCs a novel property of reversible assembly controlled by light. This means that for the first time, HRCs can be assembled and disassembled in an efficient and controllable manner. This opens a new way of building topological structures in material chemistry.

2.2 Results and Discussion

2.2.1 Synthesis and Characterisation of Functional Nanoparticles

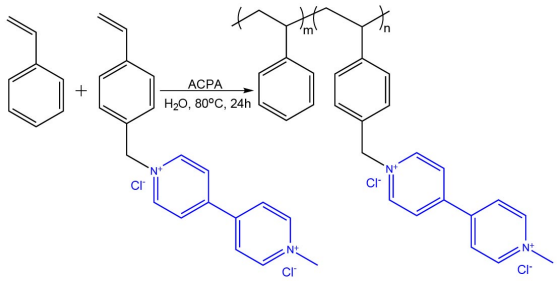

Figure 2.4: Reaction scheme of MV-NP (PSt-*co*-StMV).

Corona polymeric MV-NP (PSt-*co*-StMV) was synthesized by soap-free-emulsion polymerisation (Figure 2.4). The mixture turned cloudy after the initiation, indicating the formation of microspheres in water. The prepared dispersion was then purified by dialysis for a week to remove un-reacted monomer. Monodisperse MV-NPs with a size of 42 ± 2 nm were clearly observed under the TEM (Figure 2.5a). Figure 2.5b shows the hydrodynamic diameter distribution of MV-NPs in the neutral aqueous solution measured by dynamic light scattering (DLS). The average hydrodynamic diameter (D_h) of MV-NPs is 50 nm with a low PDI of 0.013. The D_h of MV-NPs is slightly larger than the size measured by TEM on account of the hydration layer of MV-NPs.

The molar ratio between styrene and StMV was kept above 25:1, and interestingly as more molar equivalents of StMV were added, the resulting colloids became smaller. As observed from the TEM images (Figure 2.6), MV-NPs with size of 50 nm to 110 nm were successfully prepared. The reason for the change in size could be attributed to the addition of the monomer StMV. This StMV molecule has a double positive charge at one end

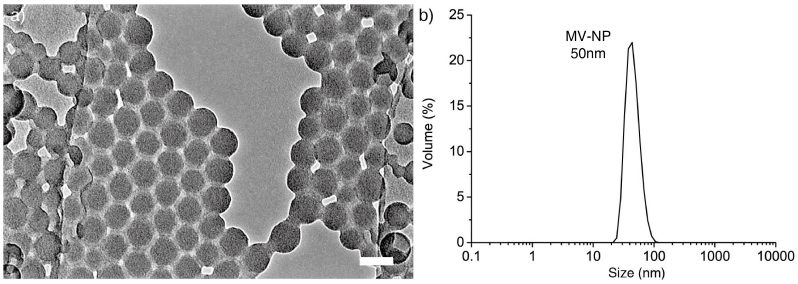

Figure 2.5: a) TEM image of MV-NP (scale bar is 50 nm); b) and corresponding hydrodynamic diameter distribution.

that make it water soluble and a hydrophobic styrenic moiety. Thus the monomer StMV can also act as a surfactant to stabilise the growing particle (hydrophobic propagating chain of styrene, oligomer), where positively charged viologen parts point towards the aqueous phase while the styrenic part points towards the centre particle (hydrophobic phase). As the amount of StMV increases, more stabilised particles (aggregated oligomers) would be generated, therefore, the size of resultant colloids becomes smaller after initiation.

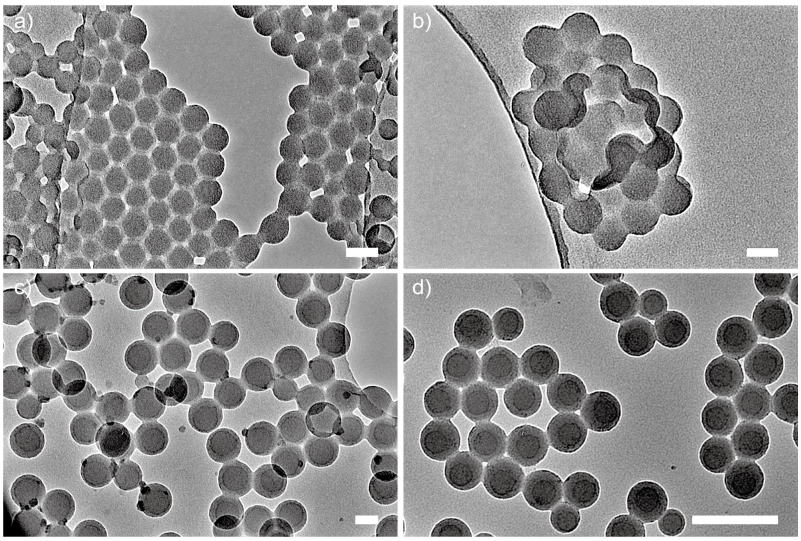

Figure 2.6: TEM images of MV-NPs prepared with varying diameter. (Scale bar a-c) is 50 nm and d) is 200 nm).

The MV-NPs were further tracked by FTIR spectroscopy. The IR spectra is shown in Figure 2.7. The characteristic IR bands at 1600, 1493, 1452, 757, and $697 cm^{-1}$ are attributed to the polystyrene segment, and the absorption between 2820 and $2780 cm^{-1}$ rep-

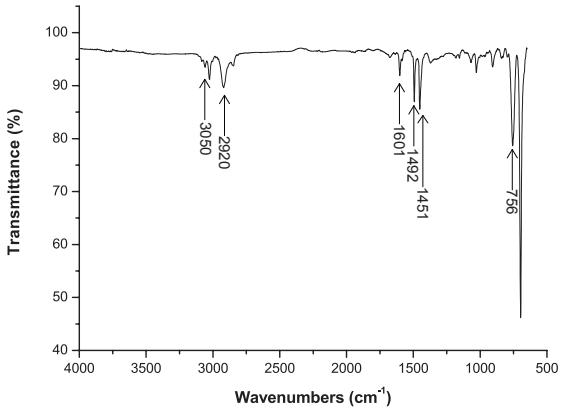

Figure 2.7: FTIR of MV-NPs.

resent the C-H stretch adjacent to the nitrogen group confirming the existence of MV functional groups on the surface of MV-NPs. Moreover, the concentration of MV on the surface was calculated to be 3 mM in the solution using UV-vis spectroscopy, the calibration curve is shown in Figure 2.8. To illustrate, CB[8] is able to enhance the UV-vis absorption of perylene diimide (PDi)[118] in aqueous solution through the formation of an inclusion complex, and the absorption is linear with the concentration of inclusion complex. The addition of MV functionalised colloids would induce further formation of the ternary complex, *i.e.* CB[8]/PDi/StMV. After filtering out these colloids, the uncoordinated perylene diimide is left in the solution. The concentration of the leftover PDi can be estimated from the UV-*vis* calibration plot. This allows for the calculation of the concentration of MV in the colloidal dispersion.

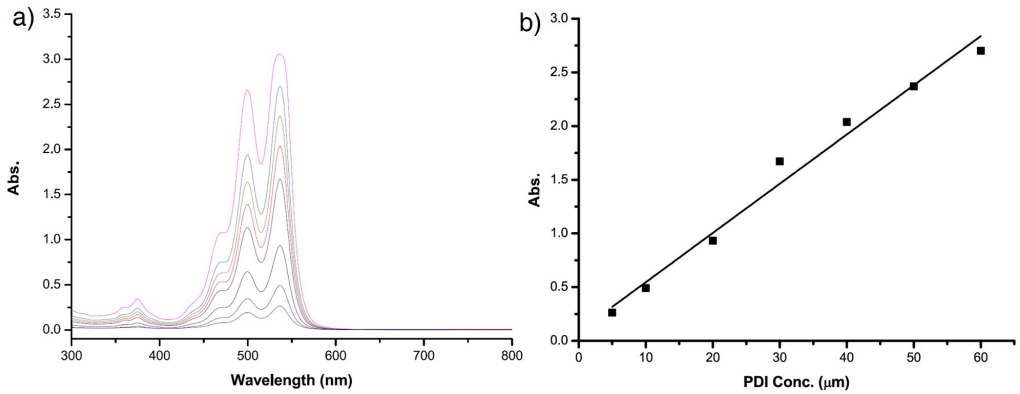

Figure 2.8: UV calibration plot of CB[8]/PDI solution.

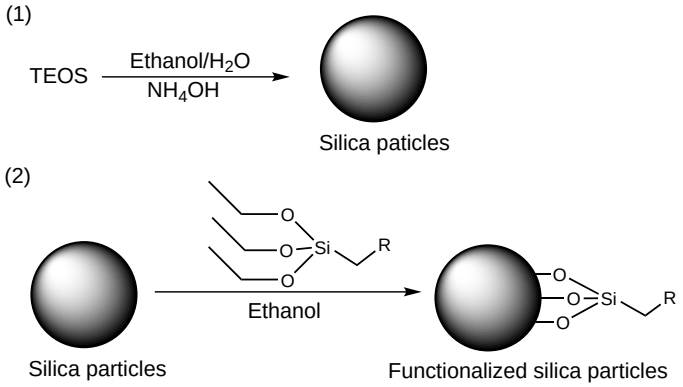

Figure 2.9: Reaction scheme for preparing Azo-silica nanoparticles .

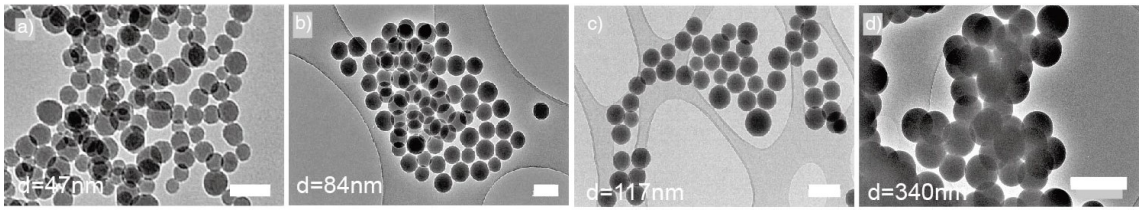

Figure 2.10: TEM images of bare silica nanoparticles of different sizes, scale bar of a-b) is 100 nm; c) is 200 nm; d) is 500 nm.

As shown in Figure 2.9, there are two main steps in the fabrication of Azo-silica nanoparticles. Firstly, SiO_2 particles were synthesized using Stöber's method, then the resulting particles were further functionalized with azo-silane (i.e. the second guest). It is observed that the size of SiO_2 particles can be easily controlled by varying the concentration of reactants (Figure 2.10). Although azo-benzene has a very intense colour (yellow-orange), the final dispersion is still white after purification by centrifugation. Also, these colloids can easily be re-dispersed into water. It can be seen from the TEM (Figure 2.11) that the particles are monodisperse spheres and the morphology is not affected by functionalization. The size determined from TEM is approximately 300 ± 10 nm. This is slightly smaller than that measured by DLS on account of water layer. In addition, FTIR measurements confirmed the existence of azo-benzene after functionalization. Figure 2.12 shows a comparison between unfunctionalized and azo-silica nanoparticles. The additional peak at 1625 cm^{-1} in spectra b) indicates the presence of an azo-benzene group

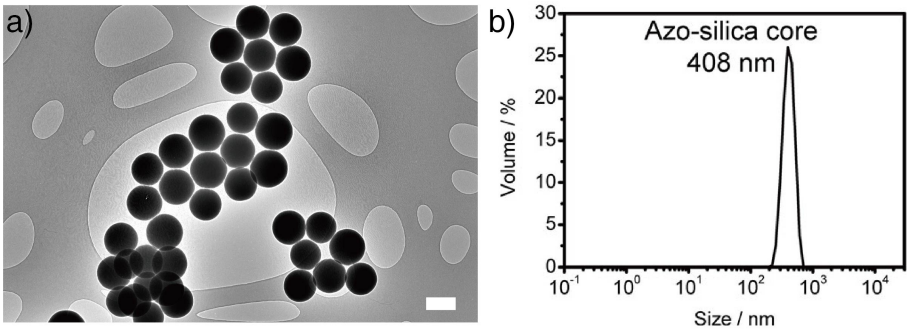

Figure 2.11: a) TEM image of Azo-silica NPs (scale bar is 200 nm); b) and corresponding hydrodynamic diameter distribution.

while the peak at 3350 cm^{-1} shows the N-H stretch. Using the same UV-*vis* spectroscopic method as mentioned previously, the concentration of azo-benzene was determined to be 0.1 mM.

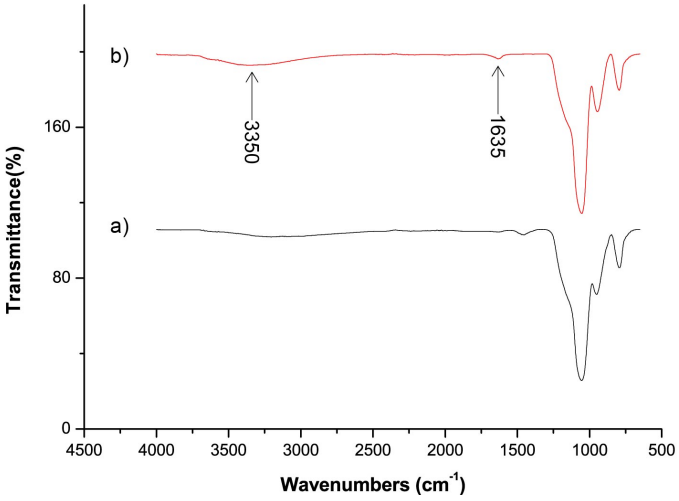

Figure 2.12: FTIR of unfunctionalized a) and functionalized b) SiO_2 particles.

2.2.2 Fabrication of Hybrid Raspberry-like Colloids (HRCs)

The HRCs were prepared by adding an aqueous dispersion of Azo-silica into an aqueous dispersion of MV-NP that was pre-complexed with CB[8] forming the inclusion complex of MV-NP@CB[8]. More importantly, the ratio between the number of MV-NP and Azo-silica is crucial, since mixing dispersions with random concentrations would end up forming uncontrolled structures (Figure 2.13). To optimize this, the titration of Azo-silica

dispersion (0.67 g L^{-1}) into MV-NP@CB[8] (0.24 g L^{-1}) was performed and characterised using DLS (Figure 2.14). Upon the addition of Azo-silica core, two peaks at 50 and 554 nm respectively were observed in the DLS measurements (Figure 2.14b). The 554 nm peak represents the formation of the HRCs and the 50 nm peak indicates the presence of free MV-NP@CB[8] in the dispersion. As more Azo-silica dispersion was added, the volume percentage (VP) of MV-NP in the DLS measurement decreased since they were complexing with the additional Azo-silica NPs. Until the point where 11 mL of Azo-silica dispersion was added, most of the MV-NP were already complexed. After this, New peaks above 1000 nm appeared (Figure 2.14c), this likely occurred on account of an excess of azo-silica core leading to the aggregation of the formed HRCs. A sample was prepared before any aggregation had occurred and the structure of the HRCs was clearly observed under both TEM and SEM as shown in Figure 2.15 and Figure 2.16.

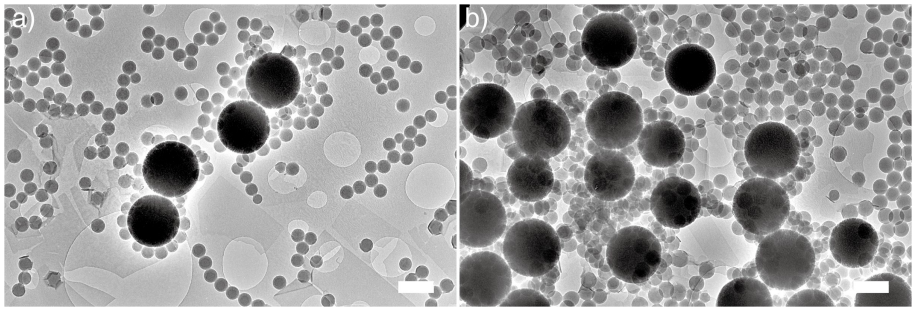

Figure 2.13: TEM of raspberry structures by mixing random amount of NV-NP and Azo-silica nanoparticles, scale bar is 200 nm.

The dynamic bonding of CB[8] enables the dissociation of HRCs by addition of a competitive guest. When 1-Adamantylamine (ADA) was added to the HRCs dispersion, the structures were dissembled and aggregation of the particles was induced (Figure 2.17a). When the HRCs were prepared in the absence of CB[8] from the procedure, or replaced by the smaller homologue CB[7], which is only able to accommodate one MV molecule, flocculation of the particles occurred (Figure 2.17b-c). Additionally, the flocculation samples were studied under TEM, no HRCs can be observed (Figure 2.18). Therefore, the HRCs were exclusively formed by employing CB[8] as a supramolecular hand-cuff to bind within the interface of the MV-NP and Azosilica Nps by the formation of (MV/trans-

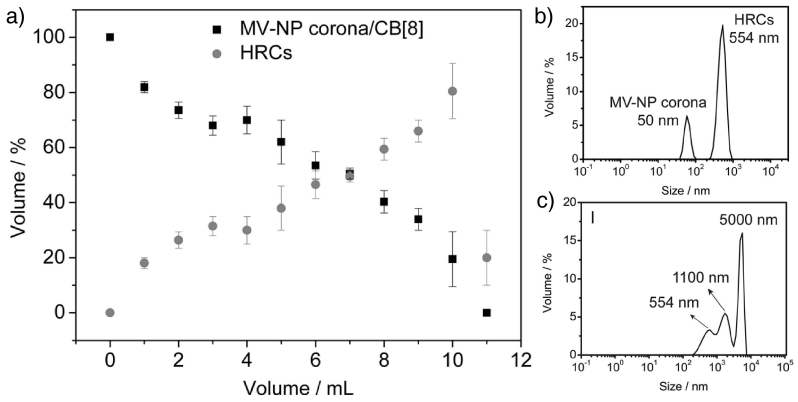

Figure 2.14: a) The variation of the volume percentage of the HRCs and MV-NP corona/CB[8] in the dispersion upon the addition of Azo-silica core; b-c) DLS results of 10 mL and 11 mL Azo-silica core dispersion added into 1 mL MV-NP corona dispersion.

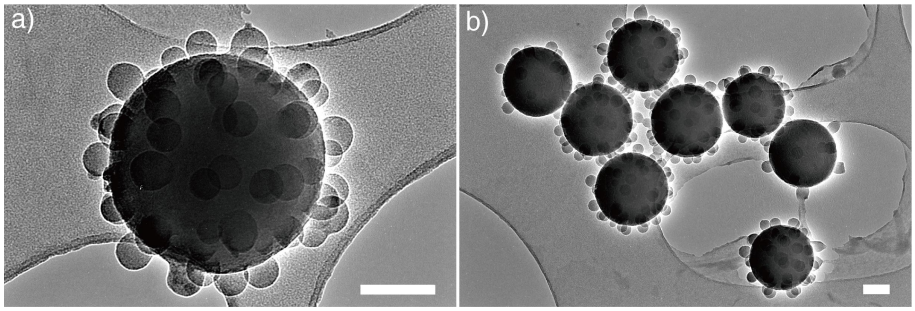

Figure 2.15: TEM images of titrated HRCs structures, scale bar is 100 nm.

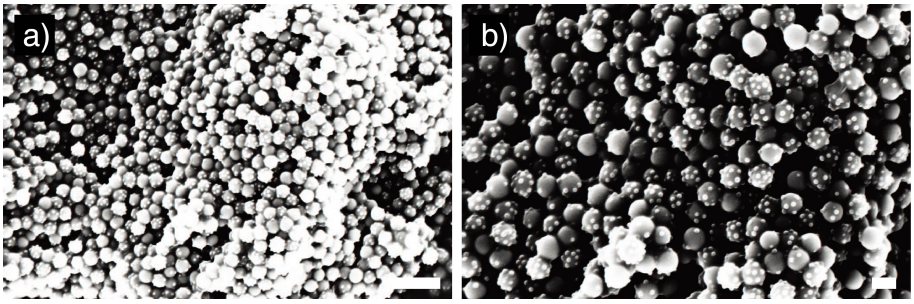

Figure 2.16: SEM images of HRCs structures, scale bar of a) is 1 μm; b) is 300 nm.

Azo)@CB[8] ternary complexes.

The dynamic host-guest complexation of CB[8] results in unstable HRCs structures which are difficult to study in a dry state. Therefore, the ability to coat the particles in order to 'freeze' the HRCs structures is important in many applications. In our case, HRCs

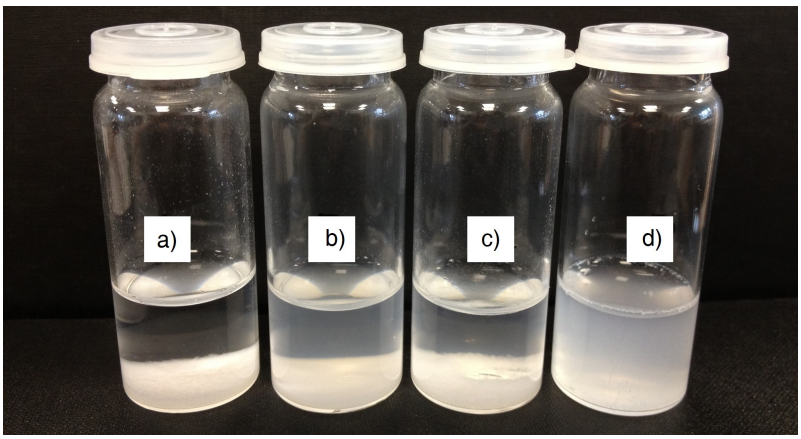

Figure 2.17: Control experiments. a) HRCs with addition of adamantane amine (ADA). b) Mixture of colloids in presence of CB[7]. c) Mixture of colloids in absence of CB[8]. d) HRCs dispersion.

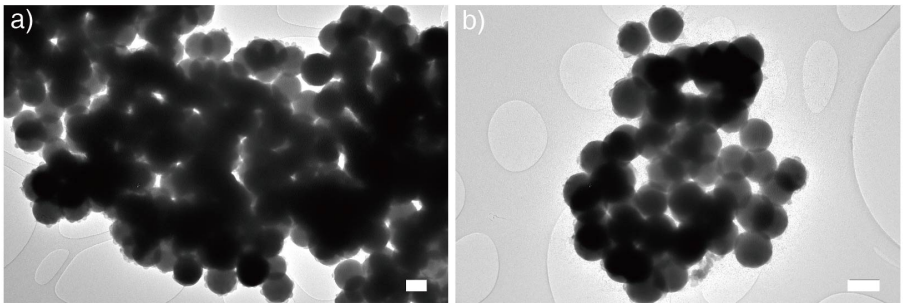

Figure 2.18: TEM of control experiment, mixture of microspheres in the absence of CB[8] shows agglomeration of the particles, scale bar is 200 nm.

were coated with a thin layer of silica. Silica coating affords materials with a rigid and stable outer-shell that can effectively avoid structural deformations caused by the change in external conditions such as high temperature.[119] Particles were coated following DLS titration by heating a dispersion with TEOS at 60°C for one hour. Figure 2.19 shows the TEM image of silica-coated HRCs where rigid raspberry structures can be observed. This is also consistent with the SEM results indicated in Figure 2.20.

The noncovalent nature of supramolecular interactions offers an opportunity to reversibly control complexation. The (MV/*trans*-Azo)@CB[8] ternary complexes could be reversibly disassembled in a controlled manner. Upon UV irradiation at 350 nm, the ternary complexes dissociated into MV@CB[8] binary complexes and free *cis*-Azo. The reverse process could be readily achieved by visible light irradiation at 420 nm. Since

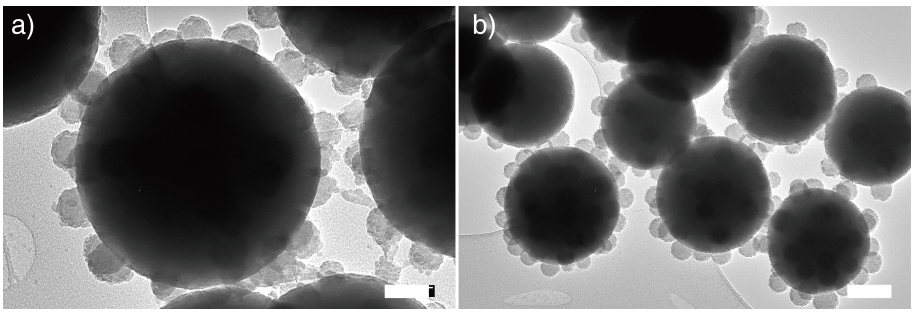

Figure 2.19: TEM of raspberry coating, scale bar of a) is 50 nm; b) is 100 nm..

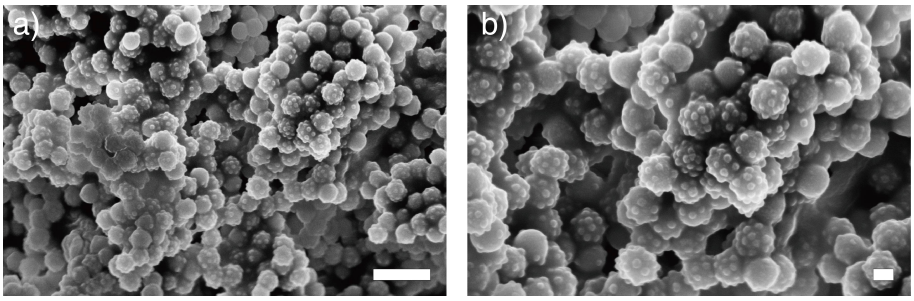

Figure 2.20: SEM of raspberry coating, scale bar of a) is 1 μm; b) is 300 nm.

the HRCs are assembled through the formation of (MV/trans-Azo)@CB[8] ternary complexes, the photo responsivity of the HRCs was tested. An aqueous dispersion of HRCs was stirred under 350 nm UV irradiation for 10 minutes before taking DLS measurements. Two peaks centred at 50 and 400 nm, which represent the sizes of the MV-NP corona/CB[8] and the Azo-silica core, respectively, can be clearly observed (Figure 2.21a). No peak centred at 554 nm can be observed. The DLS result indicated that the HRCs were totally disassembled.

TEM images also confirmed the disassembly of HRCs. As shown in Figure 2.21c, free MV-NP corona and bare Azo-silica core particles can be observed in the TEM image. Consequently, the reverse process could also be performed by stirring the disassembled HRCs dispersion with 420 nm irradiation for 10 minutes. The morphology of the re-formed colloids (re-HRCs) was detected using TEM (Figure 2.21d), where raspberry-like colloids can be clearly observed. Compared to the original HRCs, the re-HRCs contain slightly fewer MV-NP corona on the core. Moreover, the DLS result shows two peaks centred at 50 and 658 nm, respectively (Figure 2.21b). The 658 nm peak indicated the re-

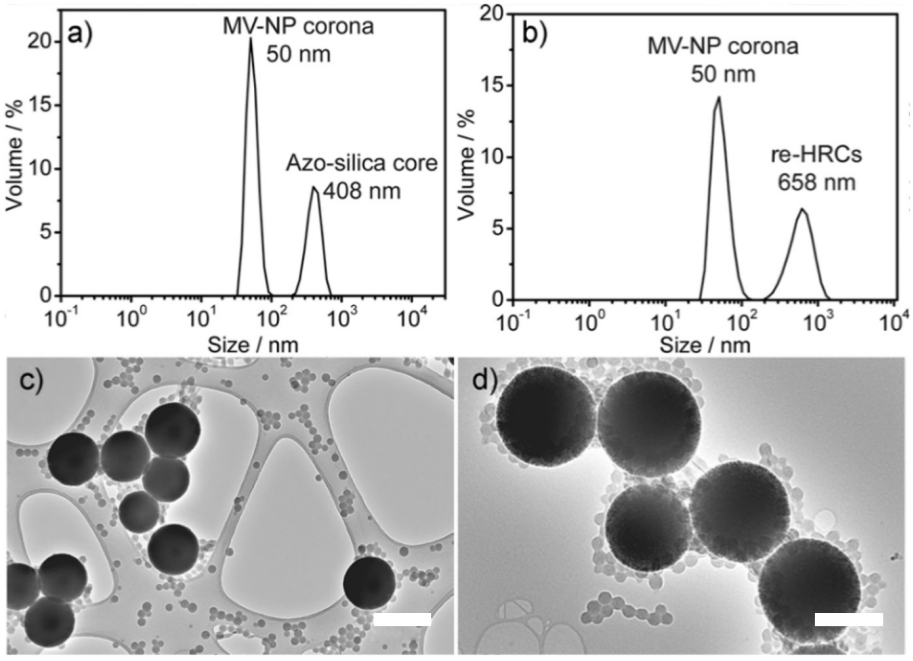

Figure 2.21: a) DLS result of the disassembled HRCs upon UV irradiation at the wavelength of 350 nm for 10 minutes. b) DLS result of the re-HRCs upon visible-light irradiation for 10 minutes. c) TEM images of the disassembled HRCs (the scale bar is 300 nm) and d) of re-HRCs (the scale bar is 200 nm).

formation of the HRCs with a small amount of aggregation and the 50 nm peak indicated that some free MV-NP corona remained in the dispersion. All these experimental results show that the HRCs prepared using the CB[8] host–guest supramolecular method are photo-responsive and the HRCs can be reversibly disassembled in a controllable manner.

2.3 Conclusion and Outlook

A novel and facile method for the preparation of hybrid raspberry-like colloids *via* supramolecular interactions was developed. The polystyrene-based outer shell particles with a diameter of 50 nm were functionalised with MV as a first guest while the silica-based core particles with a diameter around 300 nm were functionalised with azo-benzene as a second guest. The subsequent addition of CB[8] induces the formation of raspberry-like structures through a stable ternary complex between CB[8] and the guest molecules. Moreover, the formation of the HRCs is completely reversible and the disassembly pro-

cess was achieved by light irradiation and introducing the competitive guest 1-aminoadamantane amine, which are able to dissociate the ternary complex MV^{2+}/Azo@CB[8]. Lastly, coating studies allowed for the observation of HRCs in an improved manner and it was used as a good control experiment to demonstrate the favourable host-guest interactions of CB[8]. Raspberry-like colloids with hollow corona nanoparticles can also be prepared through the calcination of SiO_2-coated HRCs, which may prove useful in a number of potential applications including compartmentalized catalysis and cargo delivery. This facile supramolecular approach provides a platform to prepare sophisticated structures under mild conditions.

2.4 Experimental Appendix

2.4.1 Materials and General Methods

All starting materials were purchased from Alfa Aesar and Sigma Aldrich and used as received unless stated otherwise. CB[7] and CB[8] were prepared as documented previously.[120]

^{1}H NMR (400 MHz) spectra were recorded using a Bruker Avance QNP 400. ATR FT-IR spectroscopy was performed using a Perkin-Elmer Spectrum 100 series FT-IR spectrometer equipped with a universal ATR sampling accessory. UV-*vis* studies were performed on a Varian Cary 4000 UV-*vis* spectrophotometer. Transmission electron microscopy (TEM) characterisation was carried out on a FEI Philips Tecnai 20 TEM under an accelerating voltage of 80 kV. Samples were prepared by applying one drop of the as-synthesised microspheres onto a Holey R carbon coated copper TEM grid (400 mesh) drying overnight. Dynamic light scattering (DLS) and zeta potential (ZP) measurements were performed on Malvern Zeta-sizer NS90 instrument.

2.4.2 Synthesis of StMV

STMV was synthesized by a one-step electrophilic substitution (Figure 2.22). Typically, 1-methyl-4,4'-bipyridinium iodide (6.02 g, 20 mmol) was placed in a 500 mL flask with

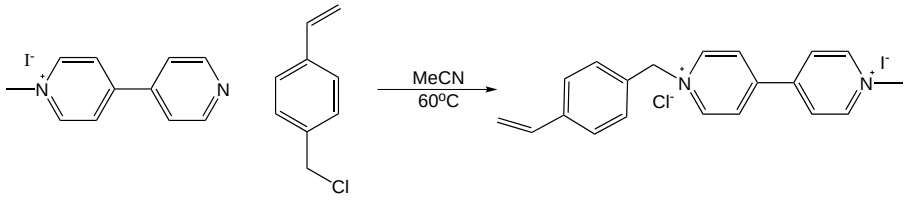

Figure 2.22: Reaction scheme of STMV synthesis.

addition of acetonitrile (260 mL). The mixture was heated to 80 °C until all 1-methyl-4,4'-bipyridinium iodide dissolved. Then 4-cholomethylstyrene (10 mL, 60 mmol) was added into the system and it was heated with stirring at 60 °C for 24 hours. After cooling to room temperature, the orange crude product was filtered, washed with acetonitrile and dried under reduced pressure to give a yellow-orange powder (5.4 g, 60%). ^{1}H NMR (400 MHz, D_2O),9.09(d, 2H), 9.0 (d, 2H), 8.46 (q, 4H), 7.56 (d, 2H), 7.45 (d, 2H), 6.77 (dd, 4H), 5.85 (t, 4H), 5.37 (d, 2H), 4.46 (s, 1H).

2.4.3 Synthesis of MV-NP (PSt-*co*-StMV)

Polymeric microspheres of PSt-*co*-StMV were synthesized by soap free emulsion polymerisation (SFEP) technique. To a 250 mL flask, 1-methyl-1'-(4-vinylbenzyl)-[4,4'-bipyridine]-1,1'-diium chloride iodide (StMV) (0.92 g, 2.0 mmol) was first dissolved in water (100 mL) to form a homogeneous solution. Subsequently, styrene (St) (5.21 g, 50.0 mmol) was added dropwise. Nitrogen was purged into the mixture for 1 h before elevating the temperature, and the nitrogen blanket was maintained throughout the polymerization. After stabilizing at 80 °C, polymerization was initiated by addition of 2,2'-azobis(2-methylpropionamide) dihydrochloride (AIBA) (0.27 g, 1.00 mmol). After 24 h polymerization, the product of the PS-*co*-PStMV nanospheres was purified by dialysis and dispersed in 100 mL water.

2.4.4 Synthesis of Azo-silica NPs

4-Aminoazobenzene (1.97 g, 10.00 mmol), 3-(triethoxysilyl)propyl isocyanate (0.25 g 1.00 mmol) and anhydrous acetonitrile (20 mL) were added into a 50 mL dry flask (Figure 2.23). A drop of dibutyltin dilaurate (TDL) was added and the mixture was stirred

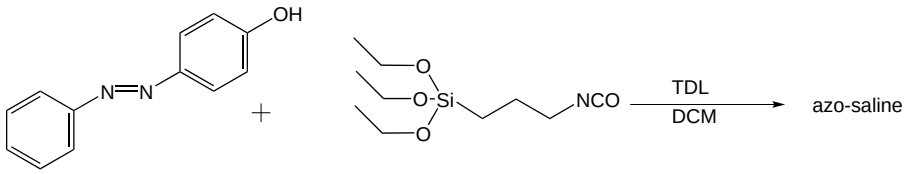

Figure 2.23: Reaction scheme of azo-saline synthesis.

for 48 h at room temperature.

Bare silica particles were prepared using Stober's method. A mixture containing NH_4OH (40%, 10.0 mL), H_2O (30.0 mL), and ethanol (270.0 mL) was prepared in a 500 mL flask. Then tetraethyl orthosilicate (TEOS) (10.0 mL) was added with vigorous mechanical stirring at 500 rpm for 12 h.

The resultant silica particle dispersion was heated to 60 °C until all NH_4OH vaporized. The prepared azobenzene silane solution (20 mL) was then added into the silica particles dispersion and stirred for 1 h at 60 °C. The final product was washed by three cycles of centrifugation/redispersion using ethanol (150 mL) and deionized water (150 mL). Finally, the product of azobenzene-functionalised silica microspheres was dispersed in 300 mL water.

2.4.5 Preparation of Hybrid Raspberry-like Colloids

The procedure was carried out in a stepwise fashion. Firstly, CB[8] (1.7 mg, 1×10^{-3} mmol) was dissolved into 10 mL of H_2O. After sonicating for 5 minutes, 50 μL of PSt-*co*-StMV nanoparticles' dispersion was added to mixture with sonication for an additional 5 minutes. 1 mL sample solution was taken and titrated with 10-fold diluted Azo-SiO_2 nanoparticles then characterised by DLS (dynamic light scattering).

2.4.6 Control Experiments of Raspberry-like Microspheres

50 μL of PSt-*co*-StMV nanoparticle dispersion was added to 10 mL of H_2O with sonication for 5 minutes. 1 mL of sample solution was taken to mix with 11 mL of 10-fold diluted Azo-SiO_2 nanoparticles. The mixture was sampled and observed by TEM.

A further control sample was prepared in the same way with addition of CB[7], the

mixture was sampled and observed by TEM.

2.4.7 Coating of Raspberry-like Microspheres

The procedure contains two parts. Typically, a mixture of H_2O (5 mL), TEOS (1 mL), EtOH (15 mL) were prepared in a flask, NH_4OH (40%, 1 mL) was then added to the mixture with stirring. Before the mixture became opaque, 300μl of the mixture was added to the previously prepared 'raspberry' solution with vigorous stirring at 60 °C for 30 minutes. The final solution was sampled and observed by TEM.

2.4.8 Control Experiments of Coating Raspberry-like Microspheres

A set of control experiments were performed. (1) A mixture of H_2O (5 mL), TEOS (1mL), EtOH (15 mL) were prepared in a flask, NH_4OH (1 mL) was then added to the mixture with stirring. Before it turned cloudy, 300μ L of the mixture was added to the previously prepared control solution (mixture without CB[8]) with vigorous stirring at 60 °C for 30-minutes. The final solution was sampled and observed by TEM.

(2)The procedure was repeated with the second control solution (with CB[7]), and a sample was to taken for TEM.

(3)PSt-*co*-StMV nanoparticles and Azo-SiO_2 nanoparticles were coated respectively in the same conditions.

Chapter 3

Catalytic Polymeric Nanocomposites *via* Cucurbit[n]uril Host-guest Interactions

Polymeric nanocomposites were prepared by using cucurbit[7]uril as a 'supramolecular anchor', as well as stabilization ligand to immobilise catalytic transitionmetal nanoparticles on the surface of methyl viologen-bearing polymeric colloids. This facile and spontaneous supramolecular approach allows for control over size, morphology and composition of the nanocomposites. Such small metallic nanoparticles impart the nanocomposites with great potential in catalysis.

This work has been published in the following peer-reviewed journal articles:

- **Wu, Y.**[‡]; Lan, Y.[‡]; Liu, J.; Scherman, O. A.* "Catalytic polymeric nanocomposites via cucurbit[n]uril host-guest interactions", *Nanoscale*, **2015**, 7, 13416.

3.1 Introduction

Transition-metal nanoparticles (TMNPs) have attracted much attention for catalysis on account of their heterogeneous nature, which allows for facile removal from reaction mixtures and recyclability.[121–123] Moreover, their unique large surface-to-volume ratio endows metallic nanoparticles with high catalytic activity (Figure 3.1).[124,125] Unfortunately, most TMNPs are unstable and tend to aggregate, suppressing their catalytic efficiency substantially.[126,127] Over the past few decades, various materials have been employed to stabilise metallic nanoparticles (NPs), such as polymeric nanofibers,[124] mesoporous silica,[128] micelles and graphene derivatives.[129,130] Such structures are mainly based on the conjugation between metallic NPs and the functional moieties in the supporting matrix, for example, thiols,[131] pyridine,[129] phenylenediamine,[130] and carbonyl groups in macrocyclic molecules.[132]

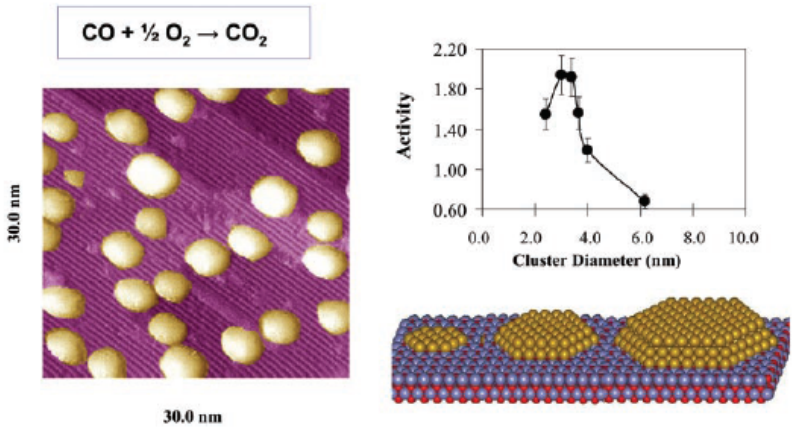

Figure 3.1: Effects of particle size on the activity of titania-supported Au for the oxidation of CO. Adapted from references.[124]

There are a few studies on metal nanoparticles and cucurbit[n]uril in the past ten years. Lee in 2009,[133] reported the supramolecular capping of cucurbit[5]uril (CB[5]) by gold nanoparticles. CB[5]-AuNP composites were successfully synthesised by reducing an aqueous solution of tetrachloroauric acid with sodium borohydride in the presence of CB[5]. Moreover, the capping process is attributed to interaction between electron-rich carbonyl portals and the surface of gold nanoparticles as shown in Figure 3.2. This is confirmed by the FTIR spectra, the observed red-shift of the carbonyl stretching band

indicates weakening of the C=O bond, due to the electron donation to the gold surface (Figure 3.3). This binding versatility is unique for CB[*n*] molecules and has not been observed for other macrocyclic hosts, such as cyclodextrins and calixarenes, with gold nanoparticles/surface.

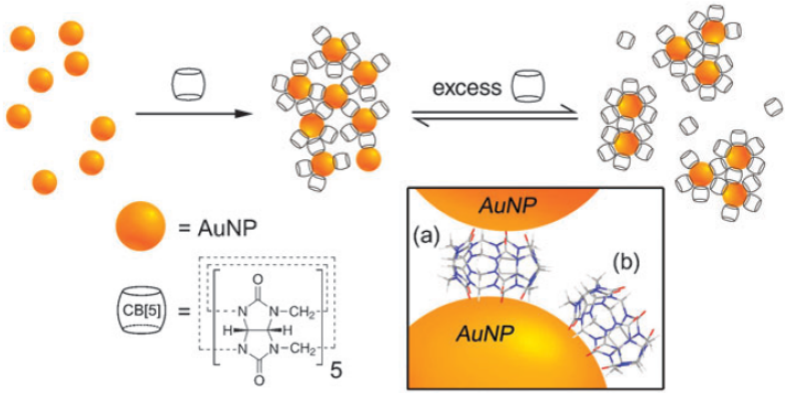

Figure 3.2: Formation of dynamic aggregates of AuNPs mediated by CB[5] in aqueous media. Inset showing CB[5] (a) doubly and (b) singly capped by AuNPs. Adapted from references.[133]

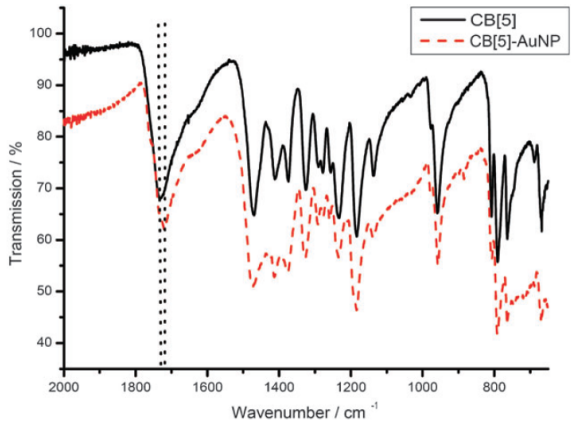

Figure 3.3: Fourier transform infrared spectra of CB[5] and CB[5]-AuNP composite.[133]

Inspired by this research, the host-guest supramolecular chemistry can be further employed to prepare nanocomposites. Herein, we report a facile fabrication route for immobilizing metal nanoparticles onto functional polymeric colloids using CB[7] host-guest approaches as shown in Figure 3.4. Functional polymeric particles are promising for stabilising metallic NPs on account of its monodispersity, mobility and simplicity of func-

tionalization. The essence of this approach lies in the complexation between CB[7] and MV guest moieties on the surface of the polymeric colloids and the strong portal affinity of CB[7] towards metallic NPs. Hence CB[7] is acting both as a stabilization ligand as well as a supramolecular anchor. Moreover, such an approach can be applied to immobilise a wide variety of transition-metal nanoparticles, such as silver, gold and palladium, which have been applied in a variety of catalytic applications. This represents a novel approach where bare metallic NPs are stabilised on colloids *via* host-guest chemistry.

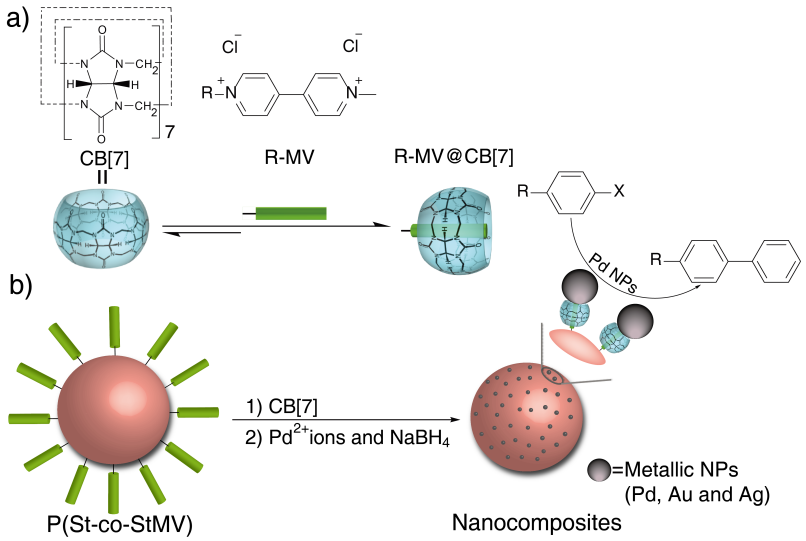

Figure 3.4: Complexation between viologen derivative and CB[7]; b) schematic formation of polymeric nanocomposites by an *in situ* reduction of metallic ions in an aqueous suspension of the poly(styrene-*co*-styrene methyl-viologen) [P(St-*co*-StMV)]/CB[7].

3.2 Results and Discussion

3.2.1 Fabrication of Polymeric Nanocomposites

The MV-bearing polymeric colloids of poly(styrene-*co*-styrene methyl viologen) [P(St-*co*-StMV)] were prepared to stabilize metallic Nps (synthetic details are referred to chapter 2). An average diameter of 42 $\pm$ 2 nm is confirmed by TEM (Figure 3.5a), and a narrow size distribution (PDI of 0.005) indicated by dynamic light scattering (DLS) analysis (Figure 3.6a). On account of the hydrophilic StMV moieties, the as-formed colloids could be

readily dispersed in aqueous solution.

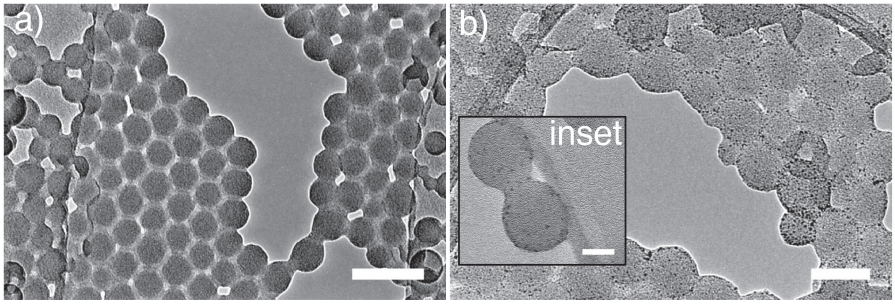

Figure 3.5: TEM images of a) P(St-*co*-StMV) colloids (scale bar: 100 nm), b) Pd@P(St-*co*-StMV) nanocomposites (scale bar: 50 nm) and inset (scale bar: 20 nm). Average size of Pd NPs: 2.4±0.4 nm.

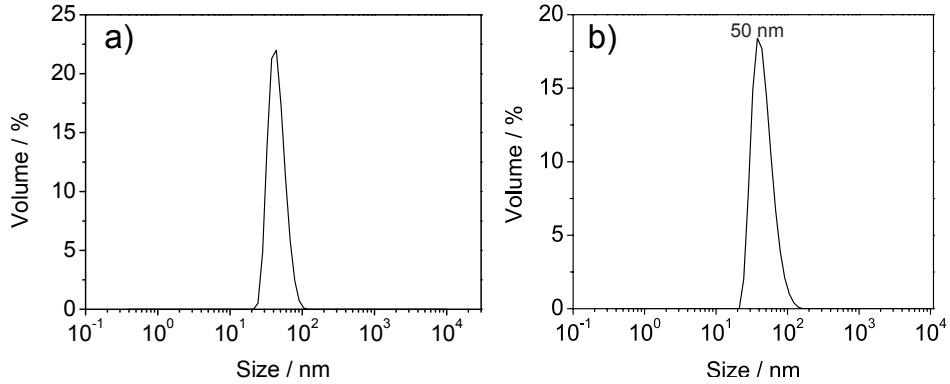

Figure 3.6: Hydrodynamic distribution of a) PSt-*co*-StMV and b) PSt-*co*-StMV/CB[7] in water.

The fabrication of nanocomposites was carried out by reducing the metallic ions *in situ* in an aqueous mixture of P(St-*co*-StMV) and CB[7]. CB[7] was first added into the P(St-*co*-StMV) suspension at a 1:1 molar ratio with respect to quantified StMV, leading to a host-guest binary complexation with MV moieties. The UV spectra (Figure 3.7) shows a blue shift upon addition of Pd ions from 237 to 232 nm. This could indicate the preliminary interactions between Pd ions and CB[7], possibly through the carbonyl portals.

As shown in the TEM images of the Pd@P(St-*co*-StMV) nanocomposites (Figure 3.5b), the Pd NPs are immobilised onto the surface of P(St-*co*-StMV) colloids. The average size of the Pd NPs is approximately 2.5 nm with a narrow size distribution. Further attempts on the different feed ratio of CB[7] were studied, and the results indicate excess of free CB[7] poses tiny impact on the formation of Pd nanocomposites (Figure 3.8). Under re-

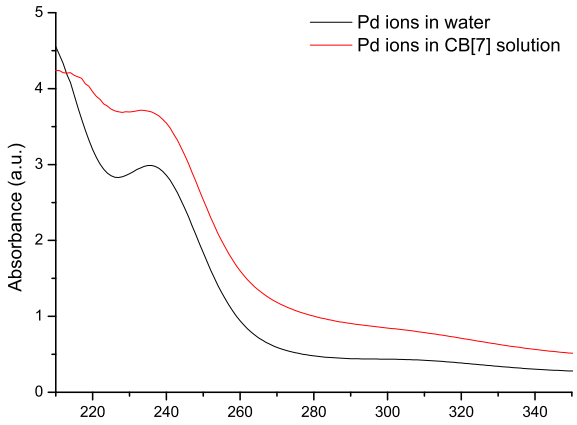

Figure 3.7: UV/vis spectra of Na_2PdCl_4 (1.2 mM) in water (red line) and Na_2PdCl_4 (1.2 mM) in CB[7] (1 mM) solution (black line). A blue shift of 5 nm was observed for the Pd/CB[7] solution (red line) at 232 nm compared to the aqueous Pd solution alone (black line), indicating the complexation between the CB[7] and Pd ions.

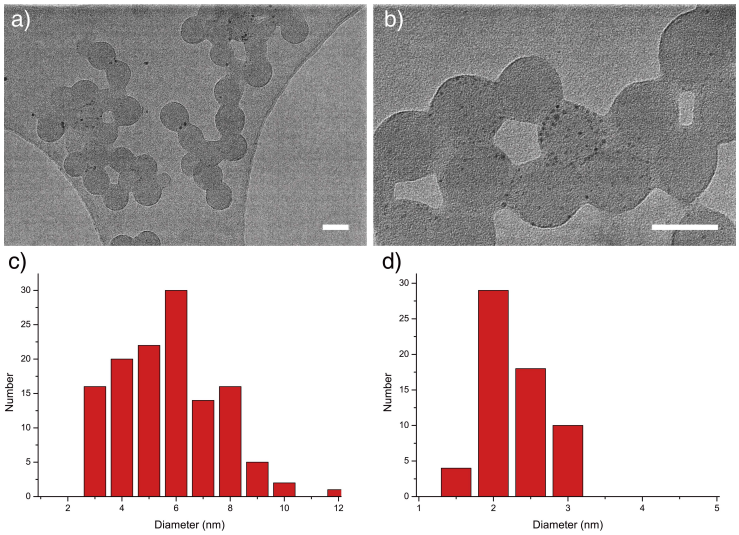

Figure 3.8: TEM images of a) Pd@PSt-*co*-StMV with 1:2 molar ratio of CB[7]/MV (scale bar: 50 nm) b) Pd@P(St-*co*-StMV) with 10:1 molar ratio of CB[7]/MV (scale bar: 50 nm) and c-d) Size distribution of Pd NPs 5.6±1.8 nm and 2.3±0.4 nm respectively. This indicates when the feeding amount of CB[7] is limited compared to the available MV moieties in the solution, the resulted Pd NPs show a wide size distribution. In addition the excess of free CB[7] has little impact on the formation of Pd nanocomposites and the size of Pd NPs.

ducing conditions, Pd NP form and immediately bind to the carbonyl portals of CB[7]. The hypothesis was further investigated in corresponding control experiments. In the absence of CB[7], aggregation of Pd NPs up to 10 nm in diameter was observed (Figure 3.9). This is probably due to a lack of stabilisation as metallic NPs cluster to avoid high surface area. This is in agreement with further visual observation, whereas the dispersion of Pd@P(St-*co*-StMV) nanocomposties remains well-dispersed for months (Figure 3.10a), moreover the corresponding dispersion in the absence of CB[7] results in a precipitate after 12 hours, as shown in Figure 3.10b.

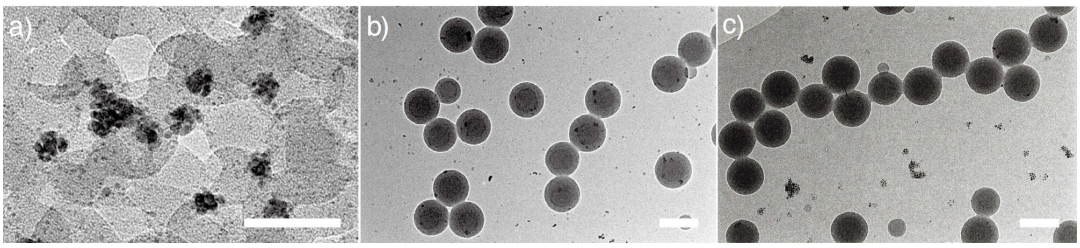

Figure 3.9: TEM images of a) the formed aggregates when CB[7] is absent during the preparation of the palladium nanocomposite (scale bar is 50 nm); b) the formed aggregates when Pd ions are first reduced and subsequently added to the mixture of CB[7] and PSt-co-StMV$_{70nm}$ (scale bar is 100 nm); c) the formed aggregates when Pd ions are reduced in the CB[7] solution followed by addition of the PSt-*co*-StMV$_{70nm}$, the gap between metallic NPs indicates the CB[7] bridging (the scale bar is 100 nm).

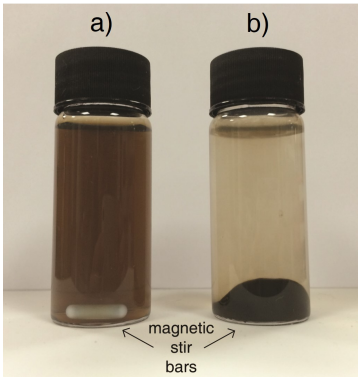

Figure 3.10: Images of a) Pd@P(St-*co*-StMV) dispersion prepared with CB[7]; b) Pd@P(St-*co*-StMV) dispersion prepared without CB[7].

When the reduction of Pd ions was carried out *ex situ* and subsequently added to the mixture of CB[7] and P(St-*co*-StMV), aggregation was observed and Pd clusters were not

immobilised onto the surface of the colloids, as shown in Figure 3.9b. Conversely, when the reduction of Na_2PdCl_4 was carried out in the CB[7] solution followed by addition into the P(St-*co*-StMV) dispersion, Pd NPs formed flocculates through portal interactions of CB[7] (Figure 3.9c). The gaps (approx. 1 nm) in the Pd aggregates indicated the presence of CB[7], in agreement with literature. These aggregated structures resemble work on honeycomb-like palladium nanostructures, in which CB[7] was employed as a capping agent to stabilise Pd nanoclusters and applied in catalysis. However, in this work by Geckeler *et al.* Pd NPs formed large aggregates bridged *via* CB[7], consequently reducing the total active surface area of Pd NPs that could substantially decrease its catalytic performance. In our case, the CB[7] was first bound strongly onto the polymeric colloids *via* MV@CB[7] host-guest complexation, leaving only one side of the carbonyl portals available to stabilise the Pd NPs as shown in Figure 3.4b. Therefore, aggregate formation through CB[7] bridging was avoided. Polymeric colloids are critical in immobilising these Pd NPs and preventing them from aggregating. This is a versatile approach to fabricate polymeric nanocomposites with other transition metals. Using a similar protocol, gold and silver nanocomposites were prepared as indicated in Figure 3.11-12, where the resultant Au@P(St-*co*-StMV) and Ag@P(St-*co*-StMV) also show immobilised metallic NPs through conjugation with CB[7].

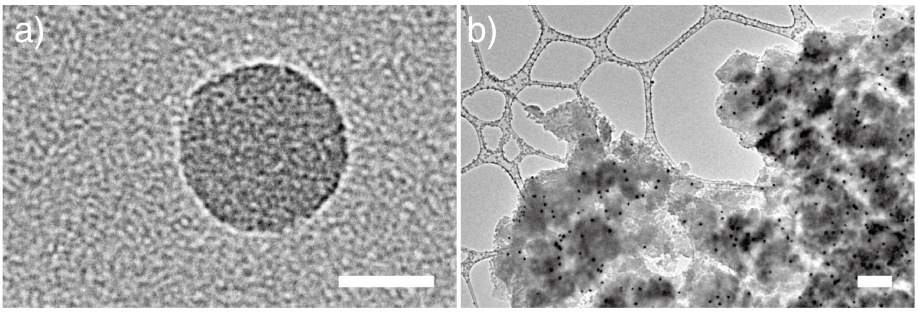

Figure 3.11: TEM images of a) Au@PSt-*co*-StMV (scale bar: 50 nm) and b) the formed aggregates when CB[7] is absent during the preparation of the gold nanocomposite (scale bar: 500 nm).

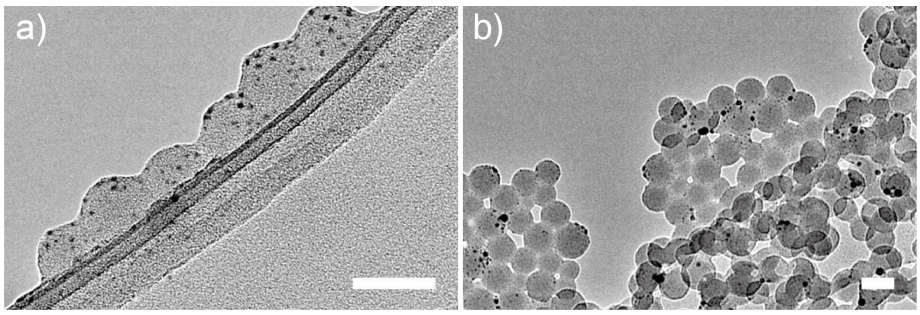

Figure 3.12: TEM images of a) Ag@PSt-co-StMV (scale bar: 50 nm) and b) the formed aggregates when CB[7] is absent during the preparation of the silver nanocomposite (scale bar: 100 nm).

3.2.2 Catalysis with Palladium Nanocomposites

In light of the extensive use of metallic NPs in catalysis, we chose the Pd@P(St-*co*-StMV) nanocomposites with a focus on the Suzuki coupling reaction. This is one of the most successful methods for generating asymmetric biaryls on an industrial scale. Many intermediates for pharmaceuticals or fine chemicals are obtained through this carbon-carbon coupling reaction. The model reaction between 4-iodophenol and benzyl boronic acid was tested initially. Water was chosen as the reaction media for its low cost and 'green' nature. With a low loading of 0.15 mol% Pd catalyst, the reaction reached completion after 15 min, as shown in the plot in Figure 3.13b, and a yield as high as 99% was achieved in comparison of the control experiment of commercial catalyst Pd/C as shown in table 3.1. The products were collected by simple organic extraction followed by reloading of the starting materials. The Pd@P(St-*co*-StMV) nanocomposites were fully recyclable, as shown in Figure 3.13c. Yields higher than 90% could still be detected after six cycles. Slight surface deformation of the supporting colloids was observed after a few cycles (Figure 3.14), which may be due to swelling during the organic extractions, could possibly lead to the slight decrease in yield as observed in Figure 3.13b.

It is known for Suzuki coupling that more economical aryl chlorides and aryl bromides are less reactive than aryl iodides, and there are few reactions conducted in water. Some Suzuki coupling reactions catalysed by other palladium nanoparticles generally do not work with aryl chlorides. We therefore attempted Suzuki coupling on a number of different aryl halides with Pd@P(St-*co*-StMV) as the catalyst. Various asymmetric bi-

aryl derivatives were synthesized with high yields (Table 3.1). Apart from palladium, gold and silver NPs are also extensively applied in catalysis. For example, Lambert *et al*. reported using small gold entities (1.5 nm) in the selective oxidation of styrene. On account of the versatility of the CB[7]-based supramolecular approach, we have shown extended work in fabricating gold and silver nanocomposites with catalytic NPs range of 2 nm. Thus, these nanocomposites are expected to show great potential in other catalysis systems.

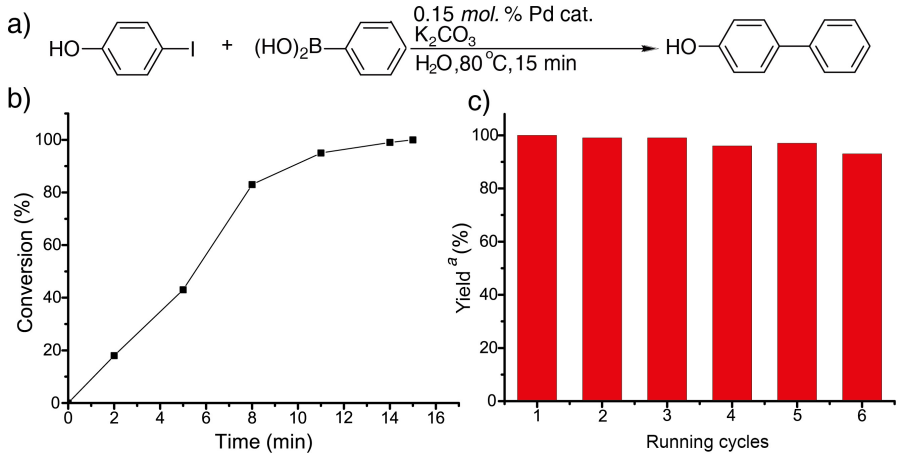

Figure 3.13: a) Typical Suzuki reaction between 4-iodophenol (1 mmol) and phenylboronic acid (1.5 mmol); reaction condition: aqueous dispersion 20 ml containing Pd@P(St-*co*-StMV) catalyst (0.15 mol%), K_2CO_3 (3 mmol) and 80 °C. b) Kinetics plot of conversion against reaction time. c) Recycle test of the Pd@P(St-*co*-StMV) catalyst for the reaction between 4-iodophenol and phenylboronic acid; [a]yields determined by HPLC analyses.

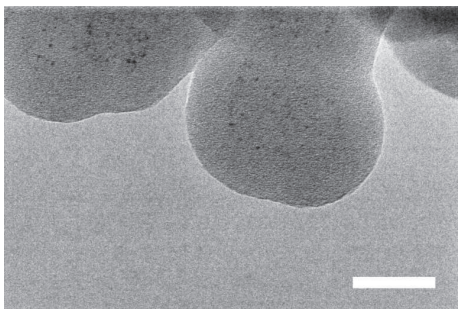

Figure 3.14: TEM images of the Pd nanocomposite after the Suzuki coupling reaction (scale bar: 20 nm).

Table 3.1: Suzuki coupling of aryl halides and $PhB(OH)_2$.

Entry [a]	Substrate	Catalyst	Time (h)	Yield [b]
1	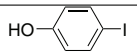	A	0.25	99%
2	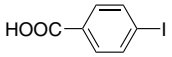	A	0.25	100%
3	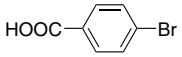	A	4	95%
4	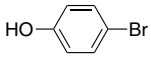	A	4	95%
5	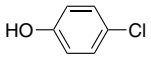	A	6	88%
6	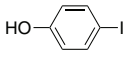	Pd/C [c]	0.25	72%

[a]Reactions 1-5 were carried out in water using 1.0 equiv. of aryl halide, 1.5 eq. of phenylboronic acid and 3.0 eq. of K_2CO_3 in the presence of Pd@P(St-*co*-StMV) (0.15 mol%) at 80 °C. [b]Yields determined by HPLC analyses. [c]A control reaction using 0.15 mol% of Pd/C (10 wt%).

3.3 Conclusion and Future work

In conclusion, the CB[7]-based supramolecular strategy provides a facile and efficient platform to fabricate nanocomposites of various transition metals under mild conditions. By taking advantage of the dual role (host/guest complexation and portal conjugation) of CB[7], metallic NPs were successfully synthesised with diameters of 2 nm and immobilised onto the polymeric colloids. In addition, the polymeric nanocomposites were used as high-performance catalysts for the Suzuki coupling reaction. This fabrication strategy based on cucurbit[*n*]uril host-guest chemistry may potentially produces nanostructures not only with prescribed morphology but also designed chemical properties that would be useful for diverse applications, such as catalysis and sensing.

3.4 Experimental Appendix

3.4.1 Materials and General Methods

All starting materials were purchased from Alfa Aesar and Sigma Aldrich and used as received unless stated otherwise. CB[7] and CB[8] were prepared as documented previously.[120]

^{1}H NMR (400 MHz) spectra were recorded using a Bruker Avance QNP 400. ATR FT-IR spectroscopy was performed using a Perkin-Elmer Spectrum 100 series FT-IR spectrometer equipped with a universal ATR sampling accessory. UV-*vis* studies were performed on a Varian Cary 4000 UV-*vis* spectrophotometer. Transmission electron microscopy (TEM) characterisation was carried out on a FEI Philips Tecnai 20 TEM under an accelerating voltage of 80 kV. Samples were prepared by applying one drop of the as-synthesised microspheres onto a Holey R carbon coated copper TEM grid (400 mesh) drying overnight. Dynamic light scattering (DLS) and zeta potential (ZP) measurements were performed on Malvern Zeta-sizer NS90 instrument.

The synthesis of StMV and PSt-*co*-StMV were described in previous experimental appendix.

3.4.2 Synthesis of Palladium Nanocomposites

The procedure was carried out in a stepwise fashion. Firstly, CB[7] (22 mg) was dissolved into 18 mL of H_2O. After sonicating for 10 minutes, 1 mL of PSt-*co*-StMV nanoparticles dispersion was added to mixture with sonication for an additional 5 minutes. 700 μL of $PdCl_2$ solution (30 mM) was taken and added into the mixture with vigorous stirring. After 10 minutes, it was treated by reduction with $NaBH_4$ (3.78 mg, 0.1 mmol) dissolved in 1 mL of water.

3.4.3 Control Experiments of Palladium Nanocomposites

1 mL of PSt-*co*-StMV nanoparticles dispersion was diluted into 18 mL water with sonication of 5 minutes. 700 μL of $PdCl_2$ solution (30 mM) was taken and added into the mixture

with vigorous stirring. After 10 minutes, it was treated by reduction with $NaBH_4$ (3.78 mg, 0.1 mmol) dissolved in 1 mL of water. The mixture was sampled and observed by TEM.

3.4.4 Synthesis of Silver Nanocomposites

The procedure was carried out in a stepwise fashion. Firstly, CB[7] (22 mg) was dissolved into 18 mL of H_2O. After sonicating for 10 minutes, 1 mL of PSt-*co*-StMV nanoparticles dispersion was added to mixture with sonication for an additional 5 minutes. 1 mL of $AgNO_3$ solution (20 mM) was taken and added into the mixture with vigorous stirring. After 10 minutes, it was treated by reduction with $NaBH_4$ (3.78 mg, 0.1 mmol) dissolved in 1 mL of water.

3.4.5 Synthesis of Gold Nanocomposites

The procedure was carried out in a stepwise fashion. Firstly, CB[7] (22 mg) was dissolved into 18 mL of H_2O. After sonicating for 10 minutes, 1 mL of PSt-*co*-StMV nanoparticles' dispersion was added to mixture with sonication for an additional 5 minutes. 1 mL of $AuCl_3$ solution (6 mM) was taken and added into the mixture with vigorous stirring. After 10 minutes, it was treated by reduction with $NaBH_4$ (3.78 mg, 0.1 mmol) dissolved in 1 mL of water.

3.4.6 General Protocol Used for Suzuki Couplings

Aryl halide (1 mmol), phenylboronic acid (1.5 mmol), and base (3 equiv) were added to 20 mL of deionized water in a Schlenk tube. The solution was purged by nitrogen and stirred at 80 °C. Pd nanocomposites (0.1 mol%) was then added to the stirred solution, and the reaction mixture was stirred for 0.25–4 h. After the reaction mixture had cooled to room temperature, the organic product was extracted with diethyl ether (3×75 mL). The organic fractions were washed with deionized water and then dried with $MgSO_4$. After filtration, the solvent was removed under reduced pressure to give the final product. A sample was analysed with HPLC.

Chapter 4

Compartmentalised Supramolecular Self-assembly of Supra-colloids

The self-assembly of structured colloids is of great importance in materials chemistry and physics. Its complexity is extensively governed by the diversity of building blocks and the assembly strategies. We demonstrate a novel compartmentalised self-assembly approach to fabricate supra-structures of micron-sized Janus particles. One semi-sphere of the micro Janus particles is functionalized by napthol moieties, complexing to polymeric nanoparticles with appended methyl viologen moieties via dynamic cucurbit[8]uril (CB[8]) host-guest interactions. The method is devoted to assembling functional 'building blocks' in a confined microdroplet environment where any non-specific interactions between particles can be avoided. The assembly process is followed by a systematic sorting where targeted structures are screened out according to their implanted fluorescence labels. The molecular recognition of CB[8] successfully directs an asymmetric assembly of supracolloids in a controllable manner, representing a new platform of topological microstructures preparation.

This work has been published in the following peer-reviewed journal articles:

- **Wu, Y.**; Yu, Z.*; Liu, J.; Oliver, J.; Abell, C.*; Scherman, O. A.* "Compartmentalised supramolecular self-assembly of supra-colloids". (submitted)

4.1 Introduction

Evolution in the biological world involves a process of hierarchical assembly from simple matter to higher complexity. Its complexity imparts great potential and versatile functionality. Likewise, in material chemistry, the ability to assemble colloids that mimick simple atoms as building blocks for molecules is a challenging topic due to the difficulty of controlling its selectivity at the nanoscale.[87,134] The past decade has witnessed an explosion in the design of hierarchical supracolloids,[135,136] leading to a variety of new architectures such as, multi-patches, cubes and dimpled colloids.[137,138] The complexity of colloidal assembly is determined by elaborate design of building blocks. Introducing anisotropy,[136,139] surface functionalization[140,141] and complementary geometry[87] are powerful tools for engineering the assembly of targeted structures.[90,137,138] In Chapter 2, we have studied and designed complementary functional particles as building blocks, and assembled them into 'raspberry' structures.

Janus particles with distinct physiochemical properties on both sides have been promising objects for the stabilization of emulsions, and the fabrication of electronic and optical devices.[142–146] The broken symmetry offers an efficient and distinctive means to target complex self-assembled materials and realize the emergence of properties (presently) inconceivable for homogeneous particles or symmetric patchy particles. These particles were named after the Roman god Janus, the god of beginning and ending, doors, and gates. One of the first persons to realize the potential and significance of such particles was P. G. de Gennes who addressed this class of particles in his Nobel lecture.

The self-assembly of Janus particles generates unique assembled suprastructures that could not be accessible from uniformly functionalized particles.[147,148,148–150] Herein, we demonstrate a novel compartmentalised self-assembly approach to fabricate suprastructures of micron-sized Janus particles. One semi-sphere of the micro Janus particles is functionalized by naphthol (Np) moieties, complexing to polymeric nanoparticles with appended methyl viologen moieties *via* dynamic cucurbit[8]uril (CB[8]) host-guest interactions. The method is devoted to assembling functional 'building blocks' in a confined microdroplet environment where any non-specific interactions between particles can be

avoided. The assembly process is followed by a systematic sorting where targeted structures are screened out according to their implanted fluorescence labels. The molecular recognition of CB[8] successfully directs an asymmetric assembly of supracolloids in a controllable manner, representing a new platform of topological micro-structures preparation.

4.2 Results and Discussion

4.2.1 Fabrication and Characterization of Janus Particles

Several methods of fabricating Janus particles have been reported, including controlled surface nucleation,[151] site-specific modification,[149,152] and templated directed self-assembly.[153] Recently, hydrodynamic methods were shown to be a simple single-step, scalable approach for the preparation of Janus Particles.[154] Here, we demonstrate the preparation of functional Janus particles through internal phase segregation of polystyrene/poly(methyl methacrylate) (PS/PMMA), induced by solvent evaporation from micron-sized emulsion droplets. This technique effectively incorporates two incompatible soft homopolymers into a Janus morphology.[155,156] As shown in Figure 4.1, **P1** is a homopolymer of polystyrene and **P2** is a functional co-polymer (poly(MMA-*co*-MANp)) with a fluorescent label. At the microfluidic flow-focussing junction, a solution of dichloromethane (DCM) containing **P1** (0.5 *wt*%), **P2** (0.5 *wt*%) and Nile Red (0.002 *wt*%) intersects a perpendicular aqueous continuous phase containing 1.6 *wt*% of sodium dodecyl sulfate (SDS), resulting in droplets of DCM periodically being sheared (Figure 4.1b). With a water/DCM flow rate ratio 2:1, stable microdroplets were generated with a high level of monodispersity, indicated by the narrow size distribution with a mean diameter (15.8 ± 0.1 μm) and a low variation coefficient (2.1%, Figure 4.1c). Under the fluorescence microscope, the observed signal of green fluorescein isothiocyanate (FITC) labelled on **P2** and the pre-mixed Nile Red were evenly distributed within the microdroplets. The combined yellow signal of the microdroplets suggests that polymers were randomly mixed without any phase separation at the initial droplet formation stage (Figure 4.1d-f). Phase separation between

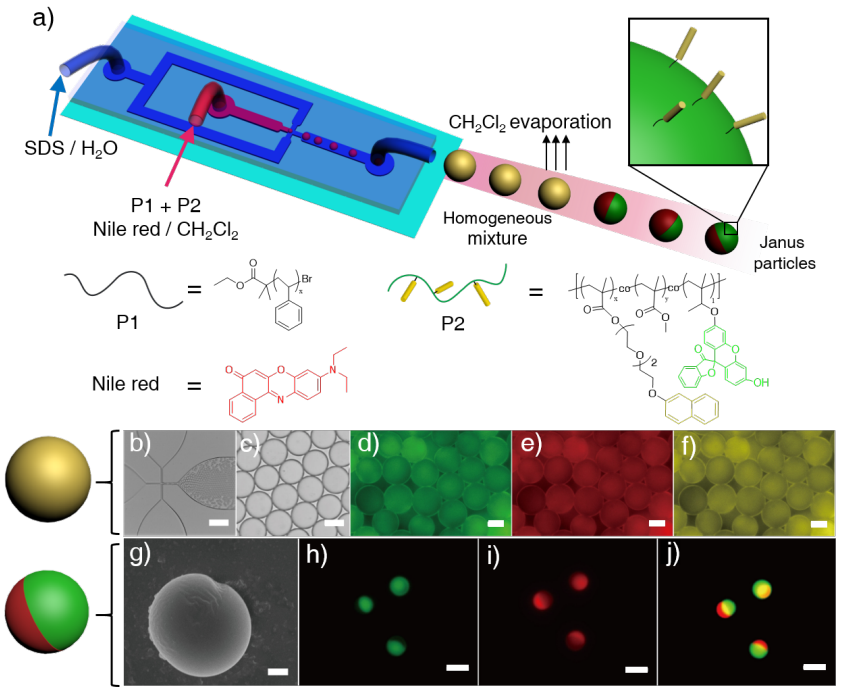

Figure 4.1: a) Schematic representation of the Janus particle fabrication process. An aqueous continuous phase containing the anionic surfactant (SDS) intersects an immiscible DCM phase containing copolymers **P1**, **P2** and Nile red, at a flow-focussing microchannel junction to form a periodic flow of oil-in-water microdroplets, yielding Janus particles by the release of DCM from microdroplets. b) Micrograph of oil-in-water microdroplets generated at the microfluidic flow-focussing channel junction (scale bar: 200 μm). c) Monodispersed microdroplets with a narrow size distribution (d=15.8 $\pm$0.3 μm, scale bar: 10 μm). d-f) Fluorescence micrographs of the microdroplets in green, red and combined yellow channel respectively. g) SEM image of the Janus particle, illustrating two distinctive phases from **P1** and **P2** (scale bar: 1 μm). h-j) Fluorescence micrographs of the Janus particles in green, red and combined yellow channel respectively, illustrating two dye-labelled regions from **P1** and **P2** (the scale bar is 1 μm).

P1 and **P2** occurred during the evaporation of DCM (Figure 4.2), and eventually yielded monodispersed Janus particles (D = 5.2 $\pm$ 0.1 μm). As shown from Figure 4.1h-j, the green signal of the FITC dye partitioned at one side of the particles, implying the phase separation of **P1** and **P2** after solidification. More interestingly, the Nile Red signal was only observed from the other side of the particles (**P1** abundant), which is attributed to the induced stacking between polystyrene and Nile Red due to their structural similarity. The Janus morphology was also confirmed by scanning electron microscopy (SEM) (Figure 4.1g), where the anisotropic contraction of the particle was caused by the electron-

sputtered etching towards **P2**. This microfluidic method ensures Janus particles with a precise control of size distribution (Figure 4.3) in comparison to bulk solution methods.[85,157] Moreover, the incorporation of a functional polymer enables a simple surface functionalisation of Janus particles. The Np moiety on the particles was confirmed by FTIR analysis (experimental appendix Figure 4.17).

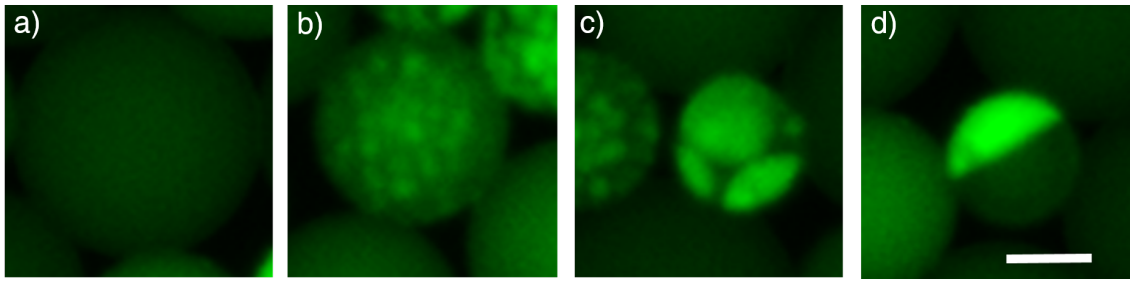

Figure 4.2: Micrographs illustrating the microdroplets of **P1** and **P2** a-d) undergo phase separation and yield the Janus particles upon solvent evaporation (scale bar: 10 μm).

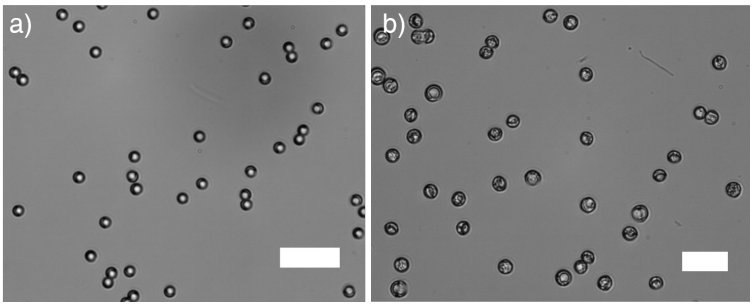

Figure 4.3: Micrographs of Janus particles prepared at different oil/water ratio (scale bar: 40 μm); Mean diameter of Janus particles in a): 3.2 $\pm$ 0.2 μm, b): 7.5 $\pm$ 0.5 μm.

4.2.2 Compartmentalised Assembly of Supra-colloids

Supramolecular self-assembly of Janus particles can be readily achieved by introducing hydrophobic interactions at the colloidal interfaces. To assemble dynamic structures with controlled selectivity, new binding motifs can be employed, such as DNA,[158] or host-guest interactions.[159] In particular, the macrocycle CB[8] is capable of simultaneously encapsulating two guests within its cavity, forming a stable yet dynamic ternary complex (Figure 4.4a). This has been exploited as a supramolecular 'handcuff' to physically

crosslink functional polymers.[56] The surface of Janus particles was functionalised with Np moieties that form a dynamic yet stable ternary complex with CB[8] and methyl viologen (MV^{2+}), K_{eq} is up to 10^{12} M^{-2} (Figure 4.4b).[55,160] Asymmetric supra-structures were obtained by treating the Janus particles with MV^{2+} functionalised polymeric colloids **C1**. **C1** with an average diameter of 70 nm was pre-mixed with CB[8], the MV^{2+} moieties on which formed inclusion complex with CB[8] on its surface (synthesis procedure discussed in previous chapter). However, the self-assembly process could not be completely controlled. The **C1**@CB[8] can act as a 'supramolecular glue' joining multiple Janus particles. Aggregation will occur as shown Figure 4.4c. Moreover, the Janus particles have a random surface coverage of **C1** on account of the assembly process taking place in bulk solution.

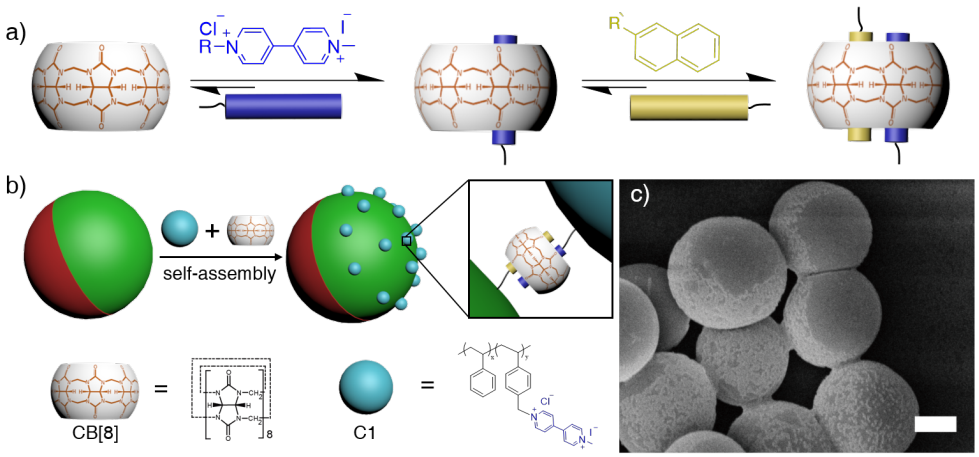

Figure 4.4: a) Schematic of the two-step, three-component binding of cucurbit[8]uril in water. b) Asymmetric self-assembly of MV^{2+} functionalised **C1** colloids onto Janus particles through CB[8] host-guest complexation. c) SEM image of aggregated Janus particles from a bulk solution *via* C1@CB[8] nanoparticles (scale bar: 2 μm).

To solve this problem, compartmentalised self-assembly was introduced, using microdroplets to isolate populations of Janus particles from their parent streams and facilitate molecular recognition between complementary colloidal particles (**C1**). This microscale environment isolates the self-assembly process from non-specific interference and uncontrolled clustering present in bulk. The compartmentalised self-assembly was carried out in three steps: encapsulation, pico-injection, and sorting, as shown in Figure 4.5.

More specifically, an aqueous dispersion of Janus particles was first encapsulated into water-in-oil droplets *via* a cross-shaped flow-focusing device. To minimize the occurrence of multiple Janus particles in a single microdroplet, the water/oil flow rate ratio was maintained at 1/5, and the concentration of Janus particles was kept at 0.16 mg/mL. The resulting microdroplets were shown to be either empty, or containing single Janus particles, with an average diameter of 31.2 $\pm$ 1.2 μm as shown in Figure 4.6. Over 40% of the microdroplets were occupied by Janus particles and the percentage of microdroplets containing a single particle was approximately 90% (Figure 4.7).

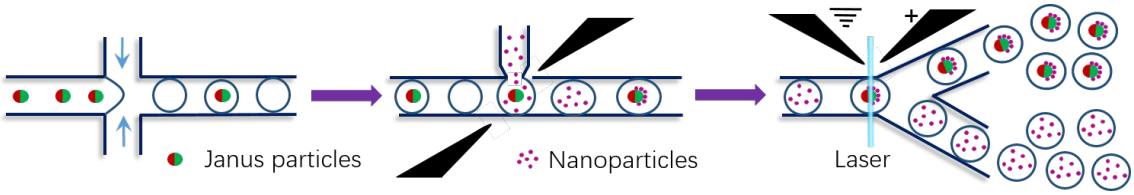

Figure 4.5: Schematic illustrations of compartmentalised self-assembly of Janus particles and the corresponding micrographs of the microfluidic chips. Janus particles were firstly encapsulated into water-in-oil microdroplets, followed by injection of **C1**@CB[8] into the microdroplets. Lastly, microdroplets containing Janus particles were sorted and collected in a separate channel.

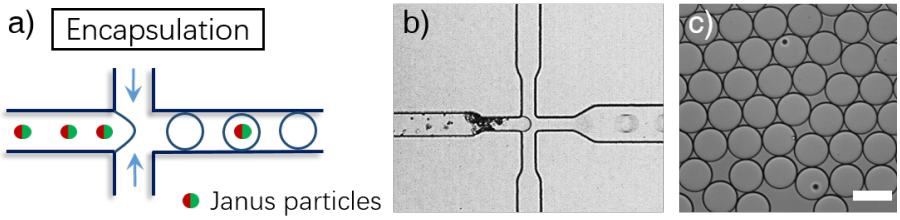

Figure 4.6: a-b) Encapsulation step and the corresponding micrograph of the microfluidic chip. c) Micrographs of microdroplets after encapsulation of Janus particles (scale bar: 40 μm).

All microdroplets collected from the first step were then re-injected into the second microfluidic device (Figure 4.8a). Microdroplets were spaced by two oil inlet channels, and flowed towards a T-shaped junction, where a channel containing an aqueous dispersion of **C1**@CB[8] was injected continuously (see Video S1-3 for details). A high voltage square waveform was applied between two electrodes positioned either side of the junction, causing fusion between a microdroplet and a fixed volume of **C1**@CB[8] dispersion.

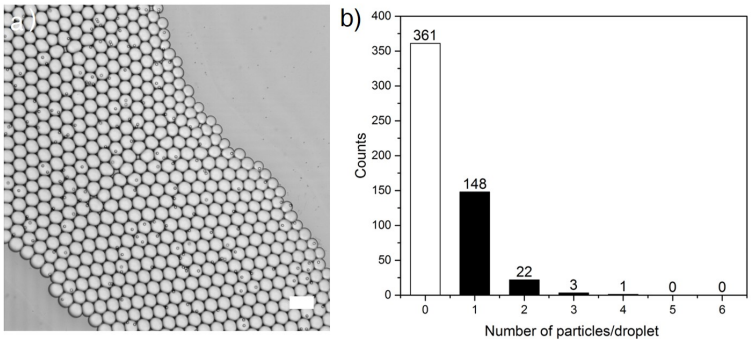

Figure 4.7: a) Micrographs of Janus particles encapsulated in the microdroplets (scale bar: 50 μm). b) Statistical analysis of the occupancy of encapsulation indicating that over 40% of the microdroplets contained Janus particles and the percentage of the single particles droplet among these microdroplets is approximate 90% (sample size: approximate 600).

The content of each microdroplet is then evenly mixed as it passed through a meandering channel before exiting the device. The mean diameter of the microdroplets following the pico-injection increased to 36.7 $\pm$ 1.4 μm on account of the additional volume from the **C1**@CB[8] dispersion (Figure 4.8b). The subsequent self-assembly process between the Janus particles and **C1** took place in each microdroplet independently.

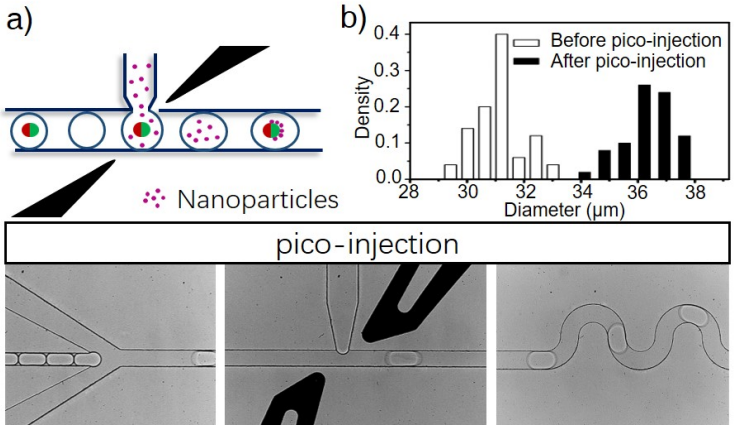

Figure 4.8: a) Pico-injection step and the corresponding micrographs of the microfluidic chip. b) Histogram comparing the microdroplets diameter before and after pico-injection.

Finally, the microdroplets containing Janus particles, were sorted from the microdroplets 'pool' according to their fluorescence signal. The sorting process is explained in Figure 4.9. A laser beam was focused to a narrow line across the sorting channel in the mi-

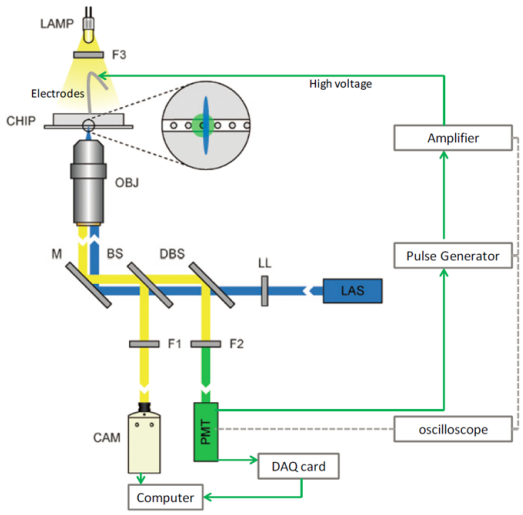

Figure 4.9: Schematic representation of the sorting setup. Laser light (LAS) shaped into a laser line (LL) and transmitted through a multi-edge dichroic beam splitter (DBS) to the microscope. Inside the microscope the laser light passed through a beam splitter (BS) and was reflected up into the objective by a conventional mirror (M). The shaped laser beam was focused to a narrow line across the sorting channel in the microfluidic chip (CHIP) where it excited droplets one at a time. The fluorescent emission from each droplet passed back along the path of the laser beam, but was reflected by the dichroic beam splitter (DBS) to the sensor of the photomultiplier tube (PMT) *via* a bandpass filter (F2). Filtered light from the microscope's halogen lamp (LAMP) illuminated the channels and droplets, allowing the trajectories of droplets to be monitored by the high speed camera (CAM). The filter F3 removed wavelengths of light that were detected by the PMT to avoid a high background signal. Adapted from reference[161]

crofluidic chip where it excited sample droplets one at a time. The fluorescent emission from the sample droplet passed back along the path of the laser beam, but was reflected by the dichroic beam splitter (DBS) to the sensor of the photomultiplier tube (PMT) *via* a bandpass filter (F2). A signal will be sent out from the computer to activate the electrode in the microfluidic chip and accomplish the sorting process. The Nile Red inside each particle not only distinguishes the Janus morphology, but also acts as a fluorescent label. In the third, Y-shaped sorting device (Figure 4.10a), the microdroplets containing Janus particles which carry the fluorescence signal of Nile red ($\lambda_{emission} = 630$ nm) were excited *in situ* by a laser, and detected by a photomultiplier tube. The fluorescence signal triggers the application of a waveform to the electrodes adjacent to the sorting region. This inhomogeneous electric field steers each fluorescent microdroplet into the

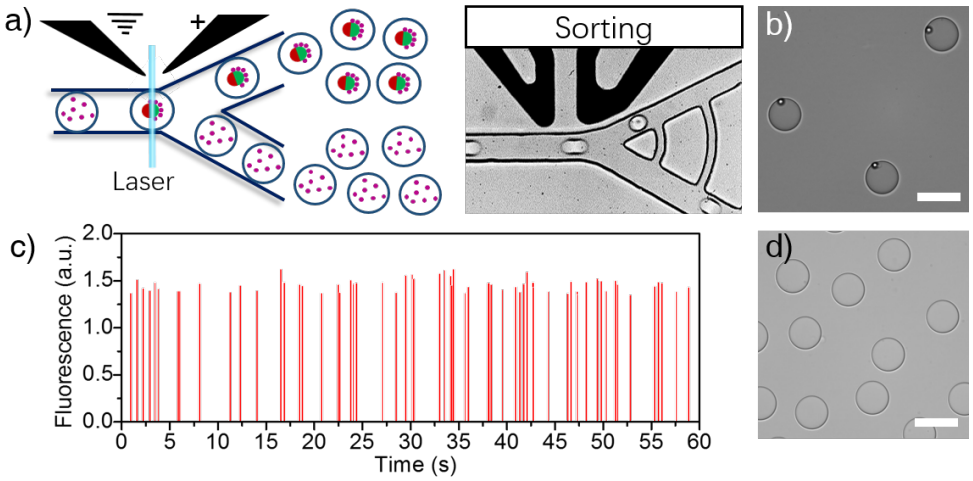

Figure 4.10: a) Sorting step and the corresponding micrograph of the microfluidic chip. b) Micrograph of the microdroplets containing single Janus particle collected from the sorting device (scale bar: 40 μm). c) Time-resolved fluorescence detection profiles from sorting microdroplets with Janus particles for 60 s. d) Micrograph of the empty microdroplets from the sorting device (scale bar: 40 μm).

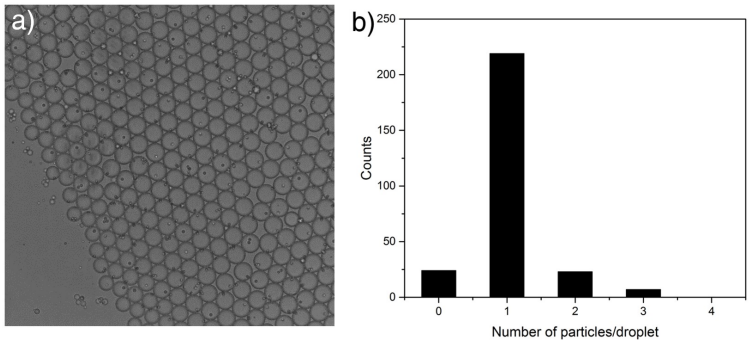

Figure 4.11: a) Micrographs of Janus particles encapsulated in the microdroplets after sorting process (scale bar: 50 μm). b) Statistical analysis of the occupancy of encapsulation indicating that over 80% of the microdroplets contained single Janus particles (sample size: approximate 300)

upper channel by dielectrophoresis, separating it from the non-fluorescent microdroplets which are drawn into the lower channel by hydrodynamic forces (see Video S4 for details). A time series recording of the fluorescence recording is shown in Figure 4.10c, with each peak representing an individual Janus particle-containing microdroplet. The sorted microdroplets were collected separately from the 'pool' of empty microdroplets, as shown in Figure 4.10b and d. The sorting process enabled microdroplets containing single Janus particle to be selected with an accuracy greater than 80% (Figure 4.11).

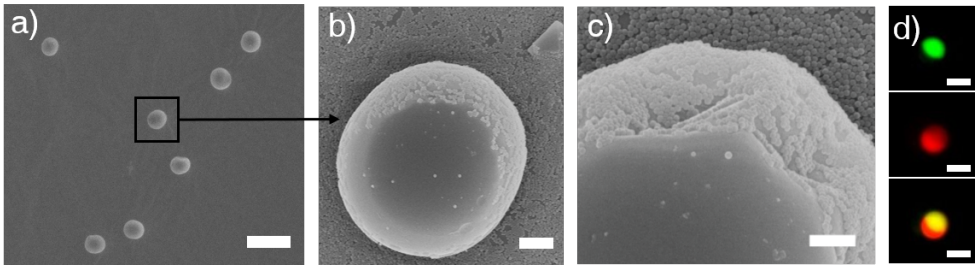

Figure 4.12: a-c) SEM images of assembled Janus particles obtained from collected microdroplets after sorting (scale bars: 40 μm, 1 mm and 500 nm respectively). d) Fluorescence micrograph of a Janus particle assembled with Nile Red labelled C1@CB[8] observed in the green, red and combined yellow channel respectively (scale bar is 5 μ).

In compartmentalised self-assembly, **C1**@CB[8] would complex with the only Janus particle within the microdroplet. Thus no aggregation can occur. Eventually, after de-emulsifying the droplet, the remaining Janus particles arrayed separately. They displayed supra-structures with **C1** selectively assembled towards only one side of the particle as shown in Figure 4.12a and b. A magnified region (Figure 4.12c) indicates the collapse in the **P2** side caused by the electron sputtering effect, which confirms that **C1** binds to the Janus particles selectively through CB[8] complexation. To further study the supra-structures under the fluorescence microscope, the Janus particles were assembled with Nile Red labelled **C1**@CB[8]. The resulting assemblies clearly showed that **C1**@CB[8] attached selectively onto the **P2** side of the Janus particles. The yellow fluorescence region on the Janus particle is produced by a mixture of the green fluorescence of **P2** and the red fluorescence of **C1** (Figure 4.12d). When the dispersion in the pico-injection step was replaced with **C1**@CB[7], no supra-structure was observed where the **C1** remains discrete from the Janus particles (Figure 4.13). This is because CB[7] cannot form the ternary complex with MV^{2+} and Np. More importantly, the density of **C1** grafted onto the surface of the Janus particles could be controlled easily by varying the concentration of **C1** in the pico-injection step. SEM images (Figure 4.14) illustrate a library of structured assemblies, where one side of Janus particle is covered by different densities of **C1**.

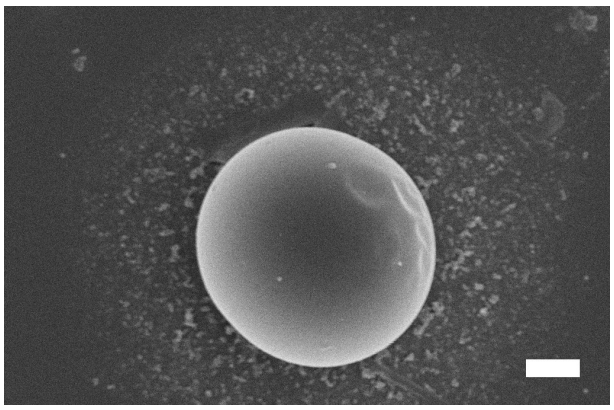

Figure 4.13: SEM image of assembling Janus particles and C1 nanoparticles with CB[7] (scale bar: 1 μm).

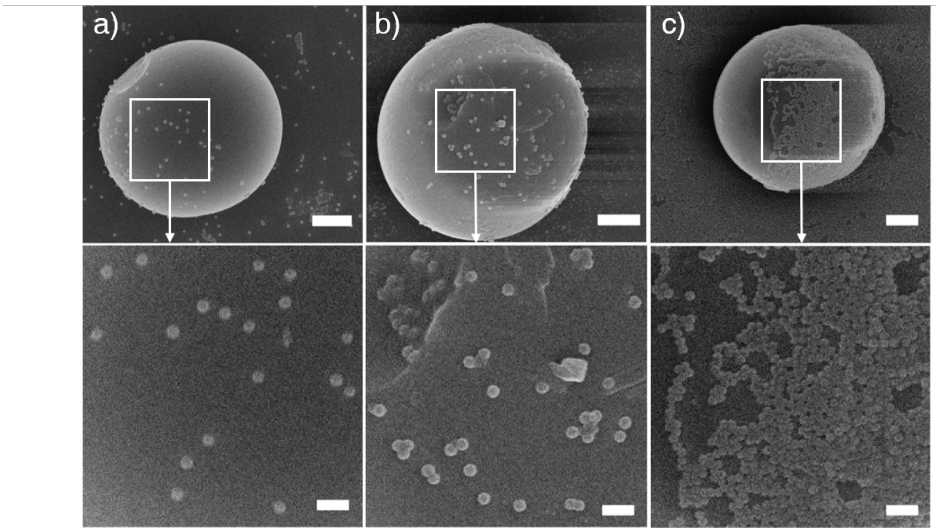

Figure 4.14: SEM images of a-c) Janus particles with different density of **C1** assembled, illustrating a versatile control of supra-colloids (the scale bar is 1 μm, the scale bar of magnified regions is 200 nm).

4.3 Conclusion and Future Work

In conclusion, the design of colloidal building blocks with selectivity has realized the fabrication of novel structured colloids. This goes beyond colloidal assemblies, whose structures are defined primarily by non-specific interactions and complementary colloidal shapes. We demonstrated a novel approach to direct the asymmetric assembly of functional Janus particles through the molecular recognition of CB[8] host-guest chemistry. The compartmentalisation of the microdroplet environment allows the formation

of targeted asymmetric supra-structures without any non-specific interference due to uncontrolled clustering. The sorting process enables a high percentage (above 80%) of targeted structures being screened out efficiently with a relatively high yield. Moreover, the ability to control the asymmetric assemblies was exhibited by tuning the coverage density of complementarily-functionalised colloids (**C1**) on the surface of the Janus particles. This systematic approach offers a new opportunity to build topological supra-colloids with great potential in colloidal engineering and material chemistry.

4.4 Experimental Appendix

4.4.1 Materials and General Methods

All starting materials were purchased from Alfa Aesar and Sigma Aldrich and used as received unless stated otherwise. CB[7] and CB[8] were prepared as documented previously.[34,120]

^{1}H NMR (400 MHz) spectra were recorded using a Bruker Avance QNP 400. ATR FT-IR spectroscopy was performed using a Perkin-Elmer Spectrum 100 series FT-IR spectrometer equipped with a universal ATR sampling accessory. UV-*vis* studies were performed on a Varian Cary 4000 UV-*vis* spectrophotometer. Transmission electron microscopy (TEM) characterisation was carried out on a FEI Philips Tecnai 20 TEM under an accelerating voltage of 80 kV. Samples were prepared by applying one drop of the as-synthesised microspheres onto a Holey R carbon coated copper TEM grid (400 mesh) drying overnight. Dynamic light scattering (DLS) and zeta potential (ZP) measurements were performed on Malvern Zeta-sizer NS90 instrument. Microscopic images and fluorescence images were obtained using an Olympus IX81 inverted optical microscope coupled with a camera of Andor Technology EMCCD iXonEMþ DU 897. M_w, number average molecular weight (M_n) and polydispersity (M_w/M_n) were obtained by aqueous or THF-GPC. The THF GPC setup consisted of two 30-cm PLgel Mixed-C columns in series, eluted using THF and calibrated against a series of 12 near monodisperse PMMA standards (M_p from 690 to 1,944,000 g mol^{-1}). The polymers were analyzed in THF at a con-

centration of 5.0 mg ml^{-1}. All calibrations and analysis were performed at 35 °C at a flow rate of 1ml min^{-1}. Scanning electron microscopy (SEM) images were obtained using a FEI Verios 460 variable pressure SEM using and InLens detector. The samples were sputter coated with a thin layer of platinum and palladium metals prior to imaging.

4.4.2 Synthesis of PSt (P1)

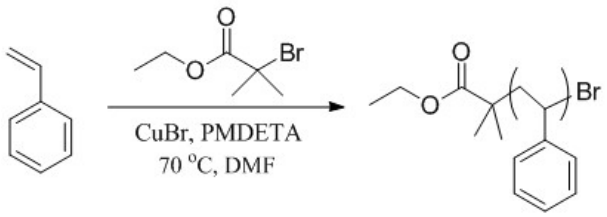

Figure 4.15: Reaction scheme of PS (**P1**)

Polymeric microspheres of PSt-*co*-StMV were synthesized by atom transfer radical polymerisation technique. To a 250 mL flask, styrene (St) (5.21 g, 50.0 mmol), PMDETA (35 μL, 0.25 mmol) were added to a solution of toluene (20 mL). The mixture was purged with Nitrogen for 15 min, CuBr (35.7 mg, 0.25 mmol) was added subsequently under nitrogen protection. The reaction was initiated by injecting ethyl 2-bromoisobutyrate dissolved in 3 mL Toluene (129 μL, 0.5 mmol). The reaction was heated to 80 °C. An aliquot of the reaction mixture (0.2 mL) was withdrawn after 24 h, which was exposed to air and divided into two parts. One part was roughly dried under gentle N_2 flow and dispersed in DMSO for the determination of monomer conversions by ^{1}H NMR analysis. The reaction mixture was then precipitated in cold methanol for purification.

4.4.3 Synthesis and Characterization of PolyMMA-*co*-MANp (P2)

Poly(MMA-*co*-MANp) was synthesized *via* free radical polymerization. To a two-neck round bottom flask were added MMA, (1 g, 10 mmol, 100 equiv.), MANp (1.3 g, 10 mmol, 10 equiv.), and FOA (38.6 mg, 0.1 mmol, 1 equiv.) in DMF (10 ml). Oxygen was removed by bubbling Nitrogen through the solution for 20 min, followed by the subsequent addition of AIBN (14 mg, 0.05 mmol, 0.5 equiv.). The flask was then immersed in a preheated

oil bath (65 °C) and the solution was stirred at 400 r.p.m. for 24 h. The resultant polymer was precipitated in cold methanol. The formed polymer was characterized to give M_w 21 kDa, PDI 1.2 from GPC (Figure 4.16).

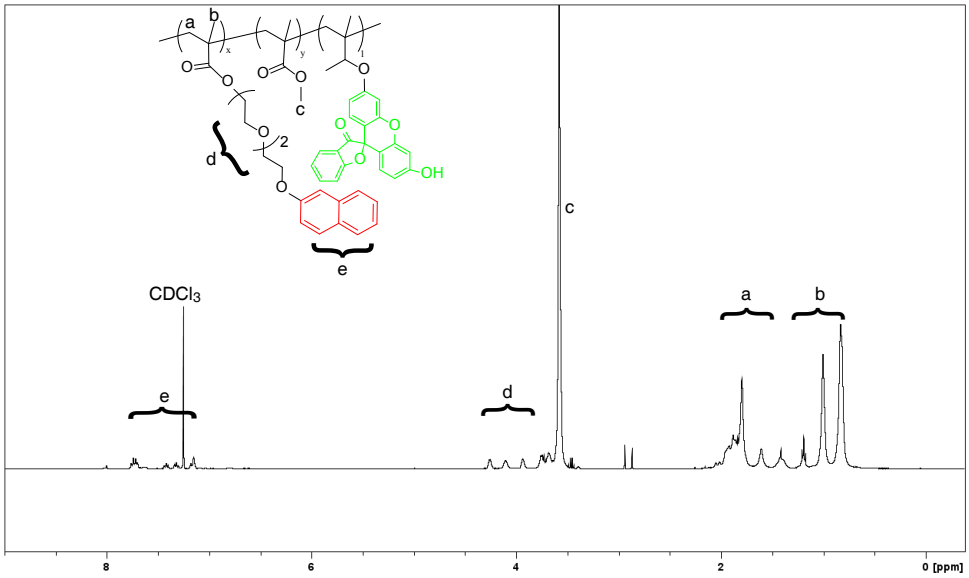

Figure 4.16: ^{1} NMR of **P2**: polyMMA-*co*-MA-PEGNP.

4.4.4 Fabrication of Janus Nanoparticles

All microfluidic chips used in this work were manufactured from silica and purchased fully assembled from Dolomite. To produce monodisperse oil-in-water microdroplets, a hydrophilic flow-focussing microfluidic chip was employed (14 μm channel depth, 3000158 Droplet Junction Chip). The hydrophobic phase (DCM) and the hydrophilic aqueous phase were injected into the microfluidic device *via* two syringe pumps (PHD, Harvard Apparatus) with controlled flow rates. The continuous aqueous phase was prepared by dissolving sodium dodecyl sulfate (1 *wt*%) in deionised (DI) water, while the discontinuous phase comprised of dichloromethane, into which **PS**, **P1** and Nile red were dissolved. Microdroplet formation was initiated by first pumping the aqueous continuous phase into the device at the rate of 50 μl h^{-1}, to fill the appropriate channels, followed by the discontinuous oil phase into the middle channel of the flow-focussing device at 100

μl h^{-1} At these flow rates, the oil flow was periodically sheared at the flow focus to form microdroplets within an aqueous carrier flow. The formed microdroplets were collected and mildly dried in aqueous solution with sodium dodecyl sulfate for two days. Phase separation occurred during the drying process and generated the Janus nanoparticles. The collected Janus particles were washed by centrifugation with water to remove any excess of surfactant.

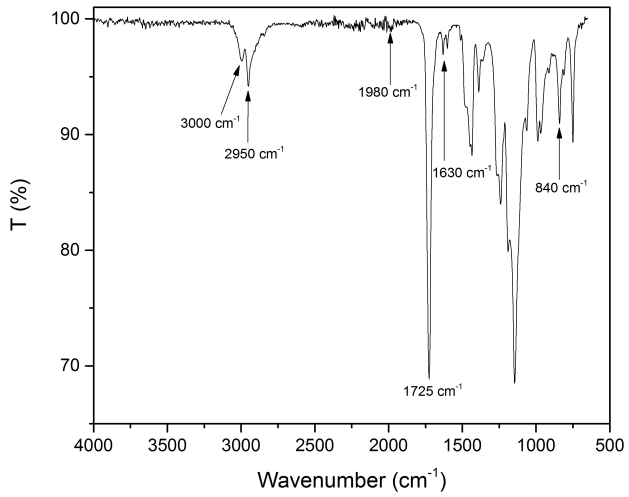

Figure 4.17: FTIR of Naphthol (Np) functionalized Janus particle

4.4.5 Encapsulation of Janus Nanoparticles

To encapsulate Janus nanoparticles in water-in-oil microdroplets, a hydrophilic flow-focussing microfluidic chip was employed (40 μm channel depth, 3000158 Droplet Junction Chip). The hydrophobic phase (HFE7500) and the hydrophilic aqueous phase were injected into the microfluidic device *via* two syringe pumps (PHD, Harvard Apparatus) with controlled flow rates. The continuous aqueous phase was prepared by dispersing Janus nanoparticles in DI water, while the discontinuous phase comprised of HFE7500 with surfactant (XL171 Spherefluidics, 1.5 *wt*%). Microdroplet formation was initiated by first pumping the oil continuous phase into the device at the rate of 500 μl h^{-1}, to fill the appropriate channels, followed by the discontinuous aqueous phase into the middle

channel of the flow-focussing device at 100 μl h^{-1} At these flow rates, the aqueous flow was periodically sheared at the flow focus to form microdroplets within an oil carrier flow. The formed microdroplets were collected in a sealed syringe.

4.4.6 Fusion of Janus Nanoparticles

For Pico-injection microdroplets with C1@CB[8] dispersion, the previously prepared water-in-oil microdroplets droplets were passed through a narrow channel with a height of 25 μm similar to the droplet diameter at a flow rate of 20 μL h^{-1}. HFE7500 oil was added from a side channel at 180μL h^{-1} to maintain the spacing between each microdroplets. In the T-shaped junction, a channel containing an aqueous dispersion of C1@CB[8] was injected continuously at a flow rate of 20 μL h^{-1}. The fusion process was observed through a high-speed camera (Phantom MIROEX4, Vision Research). A high voltage square waveform was applied between two electrodes positioned either side of the junction, causing fusion between a microdroplet and a fixed volume of the C1@CB[8] dispersion.

Video S1-3 | Videos of injecting **C1**@CB[8] continuously to the encapsulated microdroplets through a T-shaped junction.

4.4.7 Sorting of Janus Nanoparticles

The sorting of microdroplets containing Janus particles from empty ones was based on the Janus particles that carry the fluorescence signal of nile red ($\lambda_{emission}$ = 630 nm). The fluorescence detection system was used the one we reported before.[?] Briefly, emitted fluorescence was filtered through a 633 nm long-pass filter (RazorEdge, Semrock) to eliminate the 491 nm excitation wavelength from collected fluorescence. A 633 nm dichroic filter (Semrock) was used to split light between the fast-camera (Phantom MIROEX4, Vision Research) and the PMT (H8249, Hamamatsu Photonics). Emitted Nile red fluorescence from microdroplets containing Janus particles was filter by a 633 nm long-pass filter (Semrock) and the detected light was sent to a PMT (H8249, Hammamatsu Photonics) which was connected to a Data Acquisition (DAQ) card (National Instruments), con-

nected to the computer for real-time fluorescence monitoring and analysis. An oscilloscope (TDS2004B, Tektronix) monitored the collected fluorescence as well as the triggered square signal from the pulse generator (TTi TGP 110, 10 MHz, Thurlby Thandar) and amplified pulse sent to the chip from the high-voltage amplifier (PD06087, TREK).

To pass the microdroplets into the microfluidic sorting device, the microdroplets were injected into the device with a flow rate of of 12 μL h^{-1}. HFE7500 oil was added from a side channel at 120 μL h^{-1} to maintain the spacing between each microdroplets. As the microdroplets passed the laser region, the Nile Red fluorescence was excited and detected by the PMT. The PMT converted this collected fluorescence into an electrical signal, which triggered the application of a waveform to the electrodes adjacent to the sorting region. This inhomogeneous electric field steered each fluorescent microdroplet into the upper channel by dielectrophoresis, separating it from the non-fluorescent microdroplets, which were drawn into the lower channel by hydrodynamic forces (see ESI Video S4 for details).

Video S4 | Video of sorting the target microdroplet from the droplets 'pool' through a Y-shaped channel. The microdroplet contained the fluorescence-labelled Janus particles, which were dectected and activated the electrode in the microfluidic chip. The microdroplet was sorted into the upper collector channel.

Chapter 5

Bioinspired Supramolecular Fibers and its Mechanical Properties

Inspired by biological systems, we report a supramolecular polymer-colloidal hydrogel (SPCH) comprising 98 wt% water that can be readily drawn into uniform (ca. 6 μm thick) 'supramolecular fibers' at room temperature. Functionalized polymer-grafted silica nanoparticles, a semi-crystalline hydroxyethyl cellulose derivative and cucurbit[8]uril undergo aqueous self-assembly at multiple length scales to form the SPCH, facilitated by host-guest interactions at the molecular level and nano-fibril formation at colloidal length scale. The fibers exhibit a unique combination of stiffness and high damping capacity (60-70%), the latter exceeding that of even biological silks and cellulose-based viscose rayon. The remarkable damping performance of the hierarchically-structured fibers is proposed to arise from the complex combination and interactions of 'hard' and 'soft' phases within the SPCH and its constituents. SPCH represent a new class of hybrid supramolecular composites, opening a window into fiber technology through low-energy manufacturing.

This work has been published in the following peer-reviewed journal article:

- **Wu, Y.**[‡]; Shah, D. U.[‡]; Liu, C.; Yu, Z.; Liu, J.; Ren, X.; Rowland, M. J.; Abell, C.; Ramage, M. H.; Scherman, O. A.* "Bioinspired supramolecular fibers drawn from a multi-phase self-assembled hydrogel", *Proc. Natl. Acad. Sci. U.S.A.*, doi: 10.1073/pnas.1705380114

5.1 Introduction

In nature, spiders spin silk fibers with superb properties at ambient temperatures and pressures[162,163]. We are yet to mimic such an elegant process. Conventionally, synthetic fibers are manufactured through a variety of spinning techniques, including wet, dry, gel and electro-spinning[164]. Such approaches to generate fibers are limited by high energy input, laborious procedures and intensive use of organic solvents. Supramolecular pathways enable the formation of filamentous soft materials that are showing promise in biomedical applications[165–167], such as cell culture[168–170] and tissue engineering.[171] However, such materials are constrained by the length scale (sub-micron level),[172–174] energy intake duing production[170] and complex design of assembly units.[175]

Supramolecular polymeric hydrogels are a class of three-dimensional (3D) crosslinked soft materials that display a high level of responsiveness.[176] In contrast to conventional covalent crosslinking methods, strong and selective supramolecular crosslinks allow for dynamic behaviour: structural error correction,[177] shear-thinning,[178,179] self-healing, elasticity and mouldability,[180] which are desirable characteristics for a variety of important biomedical and industrial applications.[176] There are a wide variety of supramolecular motifs that can be used to fabricate supramolecular polymeric hydrogels including hydrogen bonding,[177,181] metal-ligand coordination,[182,183] host-guest complexation,[178,184,185] ionic[186,187] and 'biomimetic' interactions.[188,189] While host-guest complexation has been exploited with some interesting molecular recognition moieties, Scherman and co-workers reported high-water-content ($>$ 95 wt%) self-assembled polymeric hydrogels in 2012 based on strong and highly specific heteroternary complex formation with the macrocyclic host cucurbit[8]uril (CB[8]).[179] CB[8] is a macrocyclic host molecule that is capable of simultaneously encapsulating two guests within its cavity, forming a stable yet dynamic ternary complex. CB[8] as a supramolecular 'handcuff' has been utilised to fabricate hydrogels with different mechanical properties or responsiveness.[179,190] This has been achieved by tuning the host-guest complexation motif[191] and tailoring other functionalities on the polymer chains,[192] switching to different polymer backbones[193] as well as forming hybrid double-network materials.[194] All of these examples to date, however,

have been altered at the molecular level. Introducing shape-persistent nano-particles into the supramolecular hydrogel system allows for modification of the local gel structures at the nanoscale, resulting in assemblies with emergent properties.[195] Leibler *et al.* demonstrated a simple method for 'gluing' hydrogels together, which exploited the adhesive properties of nanoparticles with polymer chains at the gel surface leading to stress dissipation at the interface. The discovery of a simple, efficient, cost-effective method for gluing complex materials has proven to be extremely powerful, and the introduction of nanoparticles into composites has led to novel functional materials.

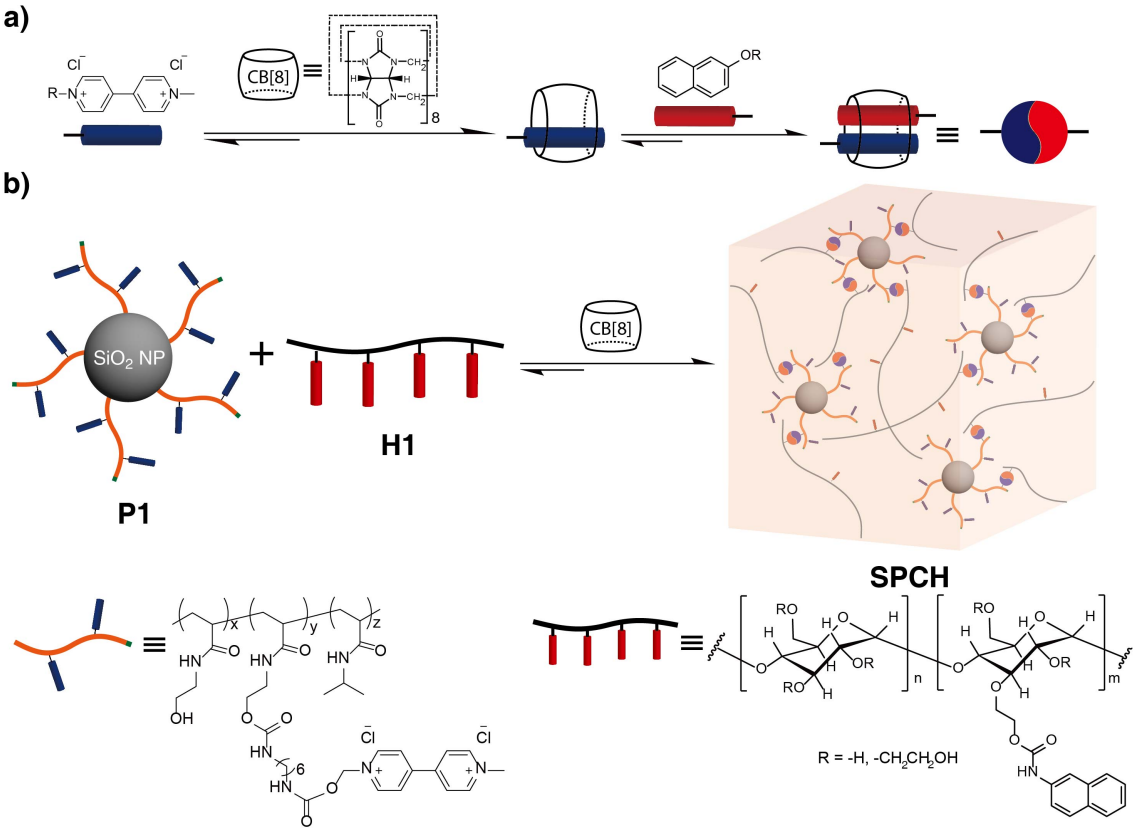

Figure 5.1: **Self-assembly of SPCH.** a) Schematic of the two-step, three-component binding of cucurbit[8]uril in water. b) Schematic representation of a supramolecular hierarchical polymer-colloidal hydrogel prepared through addition of CB[8] to a mixture of polymer-grafted silica **P1** (functionalised with MV) and a linear HEC-NP **H1** in water.

Here, we report drawing supramolecular fibers of arbitrary length from a dynamic, supramolecular polymer-colloid hydrogel (**SPCH**) at room temperature (video S1). The components consist of methyl viologen (MV) functionalised polymer-grafted silica nan-

oparticles (NP)s (**P1**), a semi-crystalline polymer in the form of a hydroxyethyl cellulose derivative (**H1**) and cucurbit[8]uril (CB[8]) as illustrated in Figure 5.1. The macrocycle CB[8] is capable of simultaneously encapsulating two guests within its cavity, forming a stable yet dynamic ternary complex, has been exploited as a supramolecular 'hand-cuff' to physical crosslink fuctional polymers.[179,190] Introducing shape-persistent nanoparticles into the supramolecular hydrogel system allows for modification of the local gel structures at the colloidal length scale, resulting in assemblies with unique emergent properties.[195] The hierarchical nature of the **SPCH** is presented, where the hydrogel is composed of nanoscale fibrillar structures. The self-assembled **SPCH** composite exhibits great elasticity at a remarkably high water content (98%), demonstrating a novel low-energy manufacturing process for fibers from natural, sustainable precursor materials. We hypothesized that the reorganisation of internal structures and the presence of crystallinity in the **SPCH** enable the formation of the 'supramolecular fiber'. Moreover, a detailed investigation of the mechanical behavior of these supramolecular fibers indicates they exhibit a unique combination of ductility and stiffness. These fibers are also remarkably efficient at absorbing energy with a high damping capacity, comparable to viscose, and in some ways, resembling the biological protein-based spider silks.

5.2 Results and Discussion

5.2.1 Self-assembly of SPCH

The fabrication of SPCH was accomplished by mixing an aqueous solution of **H1** (1 wt%) with an aqueous solution of **P1** (1 wt%), which was previously complexed with CB[8] in a 1:1 MV:CB[8] ratio (**P1**@CB[8]). **P1** is a functional polymer (M_n = 74 kDa, polydispersity indext (PDI) = 1.48) grafted onto silica NPs with a core size of 50 nm (Figure 5.1, see experimental appendix Figure 5.14 to 5.20 for synthesis). The linear polymers (**H1** in Fig. 5.1b) were prepared by functionalizing napthalene (Np) isocyanate onto hydroxyethylcellulose (HEC; M_n = 1.3 MDa).[190] The composite material exhibited elastic behavior with an increase in rigidity and a persistent shape. The hydrogel formation is clearly dependent

on the presence of all three components of the ternary complex. In the absence of CB[8], or when CB[8] was replaced by CB[7], whose cavity is only large enough to encapsulate MV alone, mixtures of **H1** and **P1** behave like a runny liquid (Figure 5.2a).

Mechanical properties of the hydrogels were investigated through rheological measurements. Strain dependent oscillatory rheology of a mixture of **H1** (1 wt%) with pre-complexed **P1**@CB[8] (1 wt%) displays a broad linear viscoelastic region with a gel-to-sol crossover point remarkably appearing only at 500% strain (Figure 5.2b). The frequency-dependent rheology performed in the linear viscoelastic region is shown in Figure 5.2c (blue circles), whereby storage moduli (G′) are dominant over loss moduli (G″) across the whole range of frequencies studied, which identifies gel-like behavior. In the absence of CB[8], no difference in the rheology was observed between an aqueous solution of **H1** (1 wt%) alone and a mixture of **H1** (1 wt%) with **P1** (1 wt%), indicating that entanglement arising from additional polymer chains **P1** does not lead to polymeric network formation (Figure 5.3). When **P1** was replaced with a larger silica NP size of 200 nm ($\mathbf{P}_{200}$) the assembled hydrogel became weaker as shown by the red squares in Figure 5.2c, as the G″ becomes larger than G′ at low frequencies. This is possibly due to the reduction in the number of effective crosslinks in the hydrogel network.[196] In addition, a rapid recovery rate of the material is observed in step-strain measurements depicted in Figure 5.2d, where alternating strains of 1% and 1000% were applied to the material at 30 (s) intervals. Overall, the process was repeated over 5 cycles and the SPCH exhibited fast and complete recovery to its initial modulus, corresponding to the fast association kinetics of CB[8] ternary complexation.[192,193]

We observed that the hydrogels were substantially 'stretchy', revealing a highly ductile nature. Moreover, a 'filament' can be drawn from a reservoir of hydrogel (5 mg) at room temperature that remained stable to lengths $>$ 250 mm (Figure 5.4a) After the water in the hydrogel filament evaporates within 30 (s), a fine and flexible fiber remains with a cylindrical shape and consistent diameter as shown in the scanning electron microscopy (SEM) images in Figure 5.4b and c. The fiber diameter was found to be independent of the draw length (R^2 = 0.001, n = 177; Figure5.5), suggesting an increase in length dur-

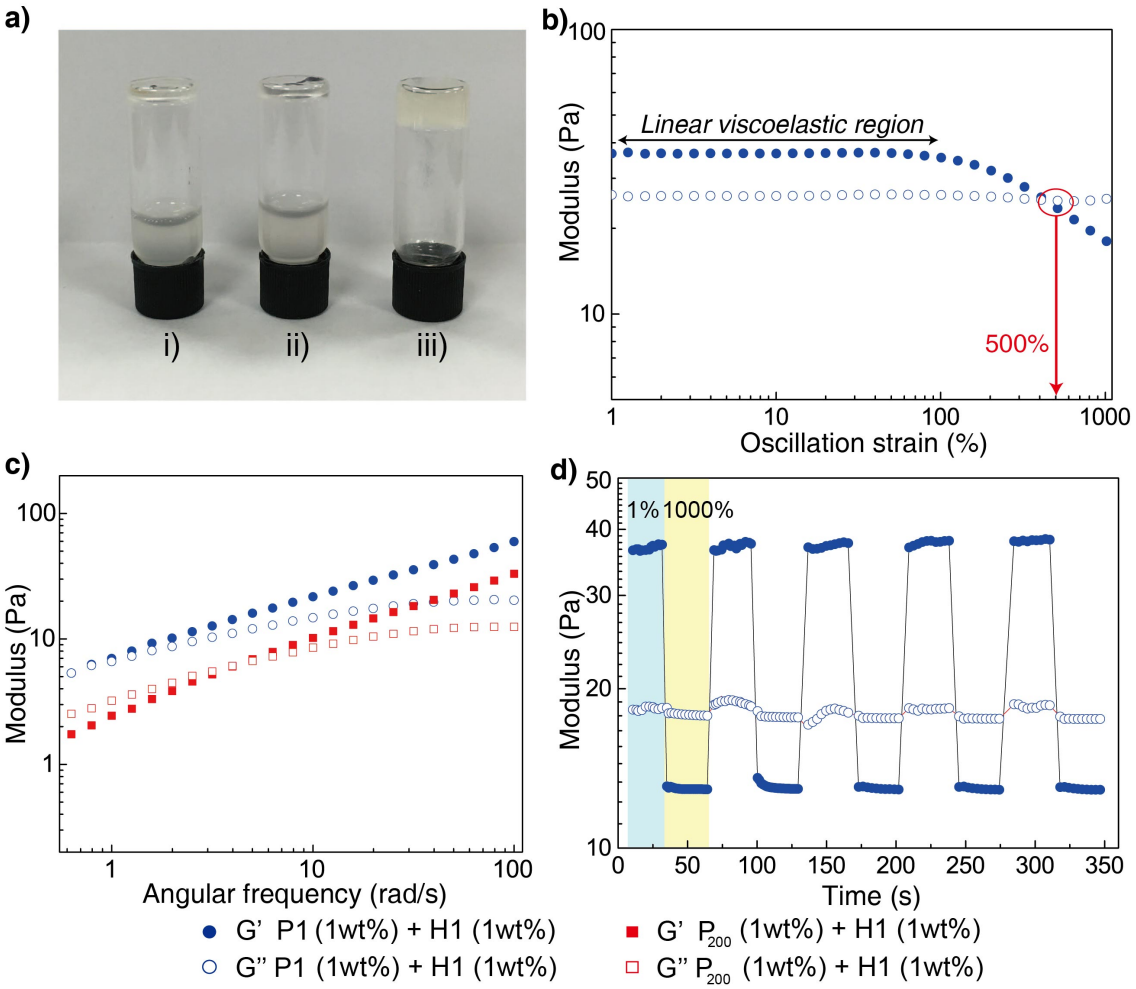

Figure 5.2: **Fabrication and rheological characterisation of the SPCH.** a) Photograph of Inverted vial tests demonstrating the formation of the hydrogel from the mixture of **P1** (1 wt%), **H1** (1 wt%), and CB[8] (0.05 wt%) exclusively. Vial **i)**: **P1** and **H1**; Vial **ii)**: **P1**, **H1** and CB[7]; Vial **iii)**: **P1**, **H1** and CB[8]. b) Rheological strain oscillatory rheology of **P1** (1 wt%)@CB[8]/**H1** (1 wt%) from 0.1% to 1000% at 20 °C (ω = 10 rad/s). The materials expressed broad viscoelastic regimes and resisted yielding up to 100% strain, G'/G'' crossover point at 500%. c) Frequency dependent oscillatory rheology, demonstrating that hydrogels with polymer grafted on 50 nm silica NPs (**P1**) have stronger and more ordered networks than hydrogels with polymer grafted on 200 nm silica NPs ($\mathbf{P}_{200}$). d) Step-strain measurement with applied oscillatory strain alternated between 1 and 1000% for 30 s periods (ω = 10 rad/s, 20 °C). At high strain, G'' dominates. Upon alternating back to 1% strain, G' recovers rapidly to its original viscoelastic property. This process was repeated across five high strain periods demonstrating good recyclability.

ing drawing was not at the expense of fiber diameter. Rather, fiber length increased through continuous drawing of material from the hydrogel reservoir and a simultan-

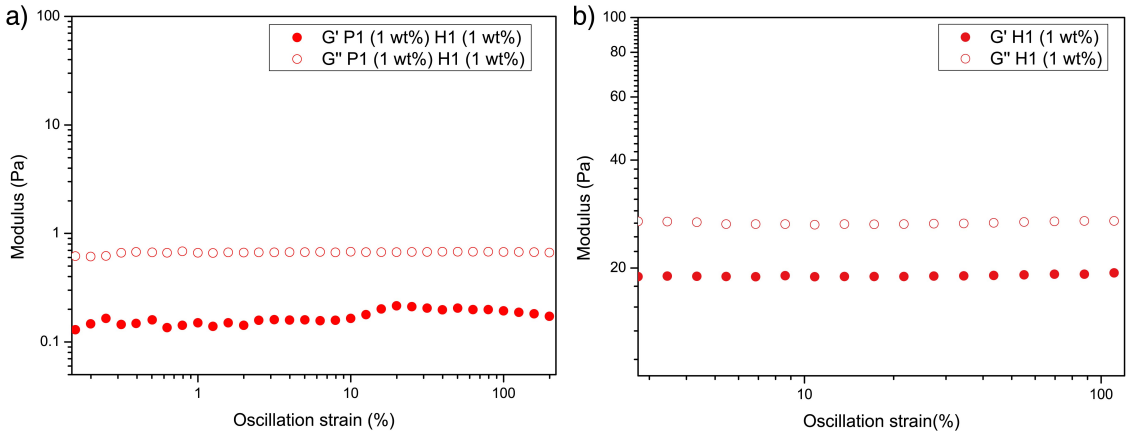

Figure 5.3: a) Amplitude dependent oscillatory rheology of the mixture between P1 (1 wt%) and H1 (1 wt%). Loss modulus (G“) is larger than the storage modulus (G‘) indicating the sol behaviour of the mixture. b) Amplitude dependent oscillatory rheology of the mixture H1 (1 wt%). Loss modulus (G“) is larger than the storage modulus (G‘) indicating the sol behaviour.

eous, rapid liquid-solid phase transition. In addition, by slicing the cross-section of the ‘supramolecular fiber’ using focussed ion beam, we observed that the silica core NPs from **P1** were dispersively embedded in the fiber (Figure 5.4d).

SEM was further used to investigate the internal structure of the **SPCH** in an effort to explain its unique ductility. Figure 5.6e-g reveals the microstructure in the cross section of the cryo-dried and lyophilized hydrogel filament. As the magnification factor increases, we observed nanoscale fibrillar features that interweave and support the internal network of the hydrogel filament. When the diameter of the silica core increased, hydrogels assembled between $\mathbf{P}_{200}$@CB[8] and **H1** exhibited nanosheet-like internal structures (Figure 5.6) compared to the nanofibril features mentioned above, which resulted in unstable filaments (that break upon dehydration). This also correlates with the frequency sweep in the early rheology study (Figure 5.2c, red squares). When **P1** was replaced with a linear polymer, poly(NIPAm-*co*-HEAm-MV) (**LP**), the hydrogel did not show such ductility, nor did it yield fibers (video S2). No nano-fibrillar microstructures were observed in the hydrogels (Figure 5.7) or for any previously reported CB[8]-based hydrogels.

More importantly, the semi-crystalline **H1** (Figure 5.8) allows further enhancement of the elasticity, where the crystalline domain of the polymer chains could reconfigure them-

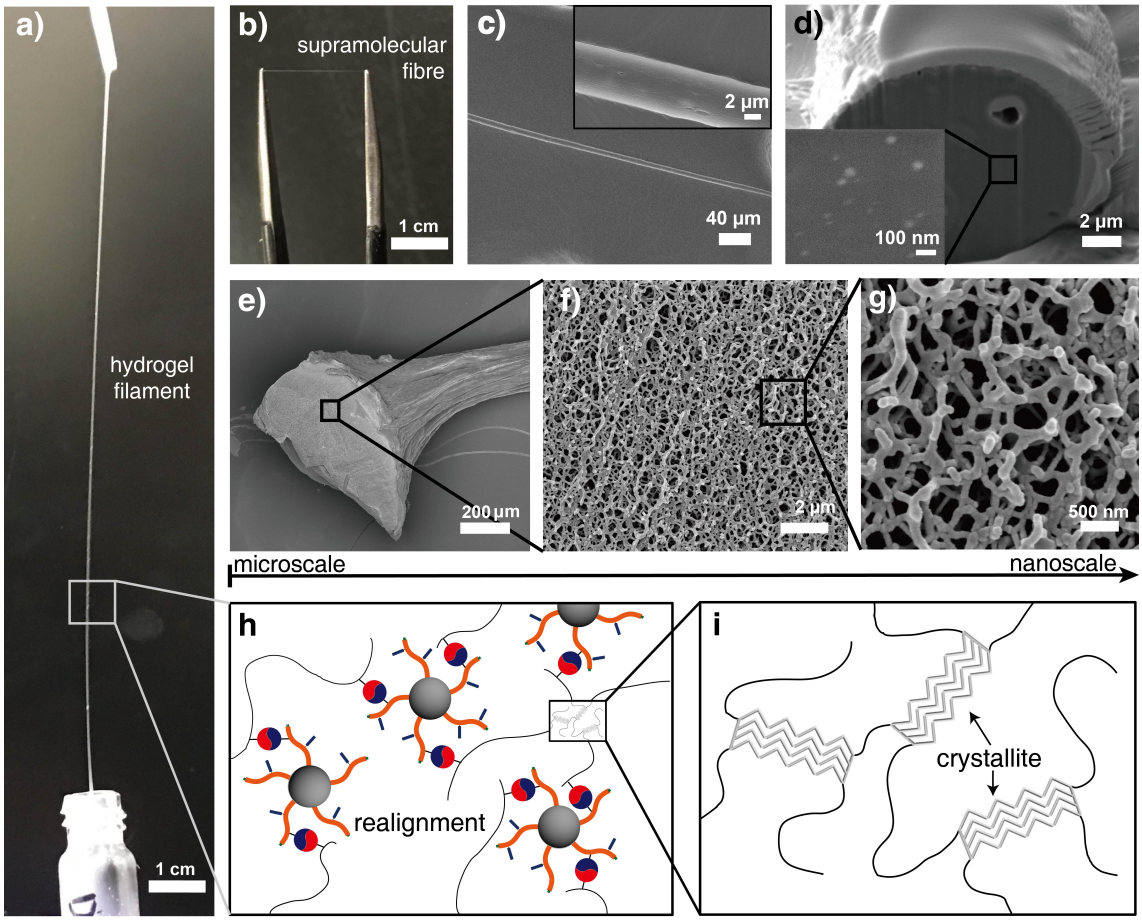

Figure 5.4: **Investigating the structure of SPCH.** a) Photograph of the hydrogel filament drawn from the **SPCH** reservoir. b) Photograph of the supramolecular fiber after the hydrogel filament undergoes fast dehydration. c) Scanning electron microscopy image of the supramolecular fiber. d) Focussed ion beam scanning electron microscopy image of the cross-section area in the supramolecular fiber, the light-colored particles in the inset depict the silica NPs with size around 50 nm dispersed inside the polymer matrix. e) Cryogenic scanning electron microscopy images of the internal structure of **SPCH** demonstrate its hierarchical nature with nanoscale fibrils feature. h-i) Proposed molecular organization within the hydrogel filament, with **H1** and **P1** physically cross-linked by CB[8], and the **H1** polymer having crystalline domains.

selves. To verify this as a generic theory, we prepared a hydrogel by replacing **H1** with Np functionalized polyvinyl alcohol (PVA) that is a typical semi-crystalline polymer. The resulting materials show similar transformations into fibers (Figure 5.9). In contrast, when amorphous functional polymers (poly(AM-*co*-HEAm-Np)) were assembled with **P1**@CB[8], no fiber formation was observed (Figure 5.10). Overall, **H1**, with crystalline domains at the molecular level, was assembled with **P1** through dynamic host-guest in-

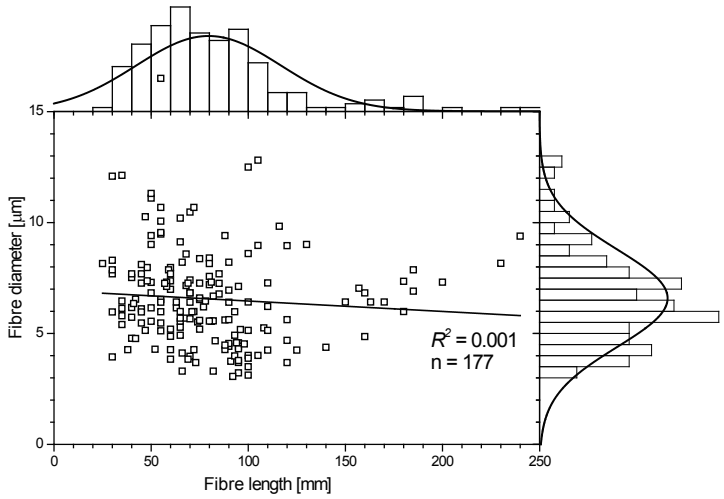

Figure 5.5: The distribution of and correlation between fiber diameter and fiber draw length (n = 177). Fibers were drawn to various lengths and their diameters were measured. There was no correlation ($R^2 = 0.001$) between fiber diameter and draw length. Frequency histograms are shown on the secondary axes, with the line representing a normal distribution curve. The fiber diameter ranged between 3.1–12.8 μm, with a mean and standard deviation of 6.6 μm and 2.2 μm, respectively. This is comparable to the typical diameter of natural spider ($<$ 1–8 μm) and silkworm (5–20 μm) silks[197,198] as well as synthetic carbon fiber (5–11 μm),[199] however, it is much finer than plant fibers (15–100 μm),[197,198] artificial silks (10–100 μm),[200] and many technical polymer and inorganic (e.g., E-glass) fibers.[198]

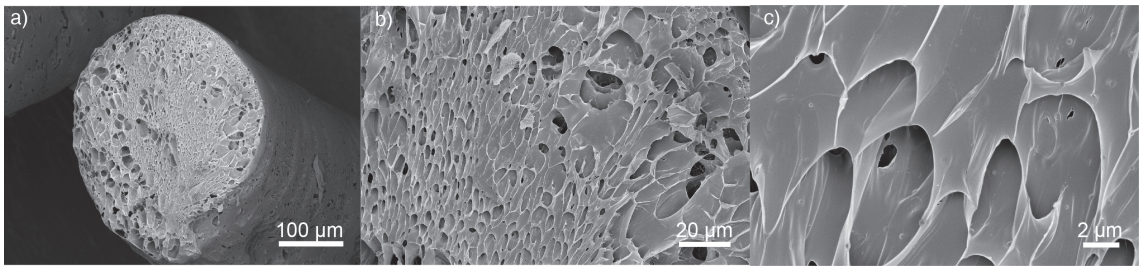

Figure 5.6: SEM images show internal structure of the hydrogel containing $\mathbf{P}_{200}$@CB[8] (1 wt%) and **H1** (1 wt%).

teractions *via* CB[8], forming the nanoscale fibrils, which extend, realign and repack at the colloidal length scale (Figure 5.4h and i). The resulting 'hydrogel filament' (drawn from the **SPCH**) exhibits hierarchical structures across multiple length scales that distribute the applied stress effectively. Finally, the large aspect ratio of the filament induces fast evaporation of water, yielding a ductile supramolecular fiber.

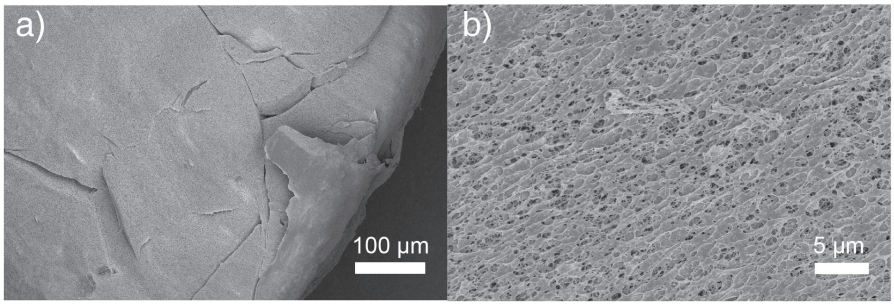

Figure 5.7: SEM images show the internal structure of the mixture between **LP**@CB[8] (1 wt%) and **H1** (1 wt%).

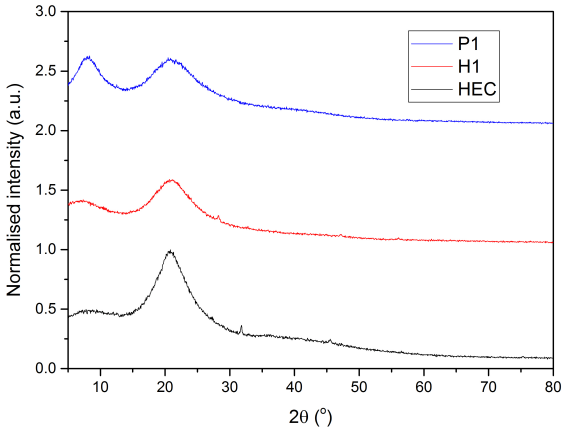

Figure 5.8: X-ray diffraction data illustrating amorphous feature of **P1** and semi-crystalline feature of both HEC and **H1** (functionalized HEC)[201,202]

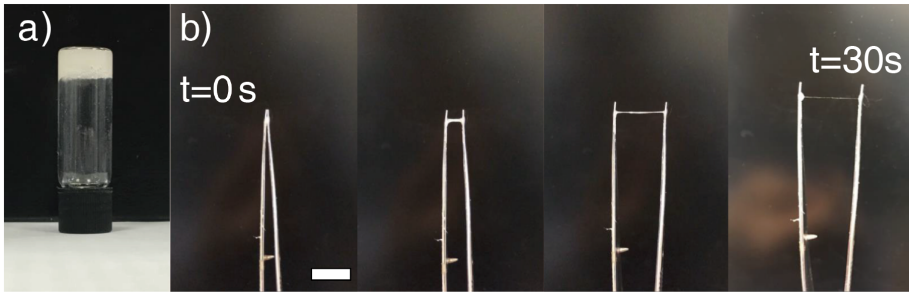

Figure 5.9: a) photograph of the mixture between P1@CB[8] (1 wt%) and PVA-Np (1 wt%, M_n = 200k). b) time resolved photographs of the drawing the mixture using a tweezers, illustrating a fiber is formed after 30s. (scale bar is 1 cm).

5.2.2 Characterisation of the Supramolecular Fiber

Stress-strain profiles (Figure 5.11a) display an initial linear region up to a yield point in the range of 1–3% applied strain. The elastic modulus determined in this region

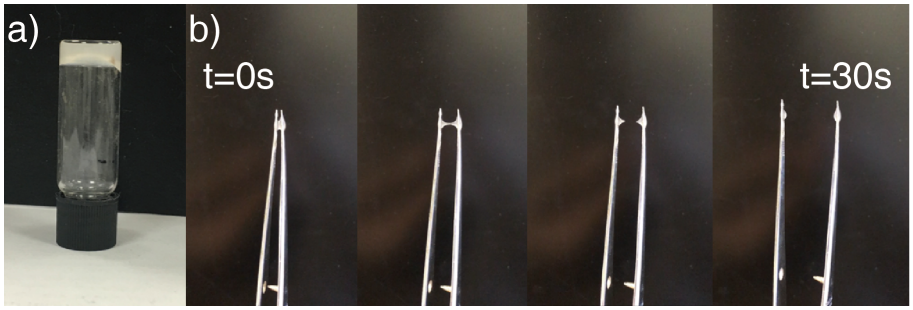

Figure 5.10: a) photograph of the mixture between P1@CB[8] (1 wt%) and P(AM-*co*-HEAm-Np) (1 wt%, M_n = 650k). b) time resolved photographs of the drawing the mixture using a tweezers, illustrating no fiber is formed. (scale bar is 1 cm).

was 6.0 ± 2.9 GPa. For polymeric materials, whose stiffness ranges between 1 MPa to *ca.* 10 GPa, the modulus is related to bond stiffness of intermolecular interactions (*e.g.* hydrogen bonding, hydrophobic interactions and van der Waals forces). Therefore, the lack of covalent interactions in our supramolecular fiber is not detrimental to its stiffness, and indeed the modulus reflects the flexible and dynamic nature of the physical crosslinks present. Failure strength and strain of the fiber were determined to be 193 ± 54 MPa and 18.1 ± 5.7%, respectively. This unique combination of tensile properties exceeds that of conventional regenerated textile fibers such as cellulose-based viscose, and protein-based artificial silks as well as animal and human hair[198](Figure 5.13). Finally, the toughness, or total energy required to break the fiber, was calculated to be 22.8 ± 10.3 MJ·m^{-3}, higher than several natural fibers, such as flax and jute.[197] The coefficient of variation in properties ranged between 30 to 50%, which is a spread commonly observed in natural fibers including biological silk[203] and flax.[204] Factors influencing variability include processing conditions (drawing speed), environmental conditions (during processing and testing) as well as the composition of the material.[203,205]

In an effort to assess reversibility and damping behavior of the supramolecular fiber, material response to cyclic loads was investigated. Fibers with low damping capacity (high resilience), like E-glass, elastin, polypropylene and vulcanised rubber are efficient at recovering most of the deformation energy they absorb, typically exhibiting little to no hysteresis; while fibers with high damping capacity (low resilience), such as viscose,

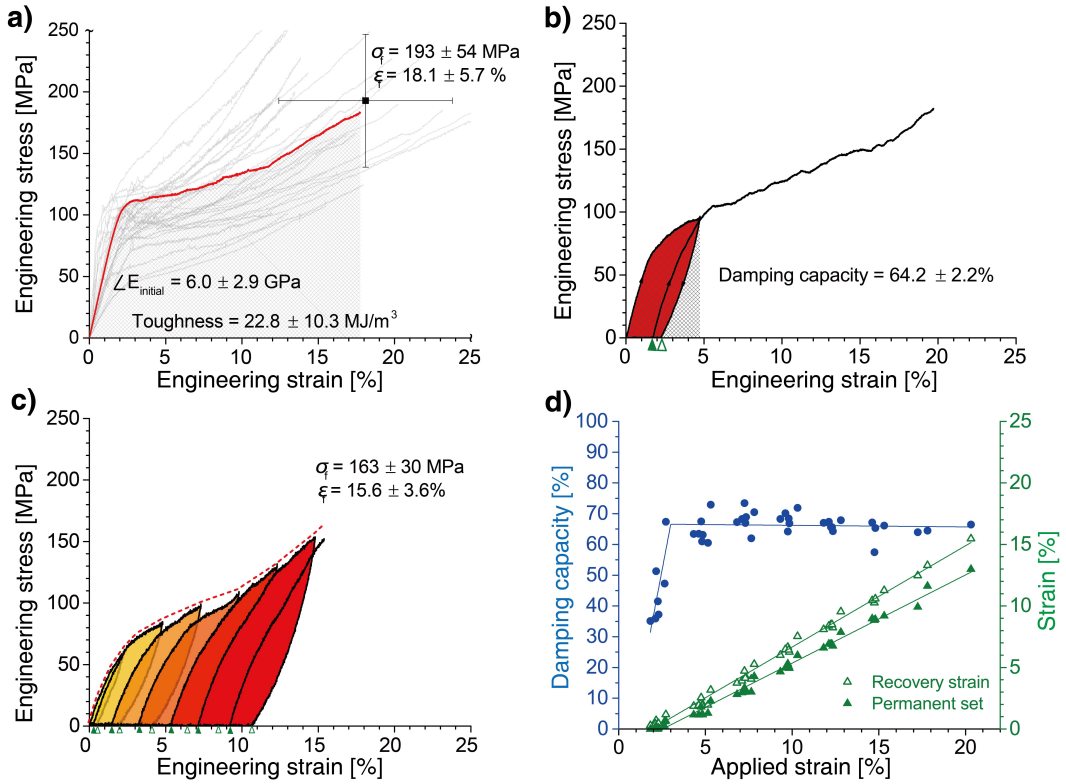

Figure 5.11: **Mechanical properties of supramolecular fibers subjected to static and cyclic tensile loads.** a) Illustration of the fiber stress-strain response at a quasi-static loading rate: grey curves indicate variability in the dataset (n = 50), with a representative data curve shown in red; the data point (solid square) indicates the mean failure strength and strain, with error bars denoting 1 std. dev. b) Representative stress-strain curve (n = 7) of a fiber subjected to a single loading-unloading-reloading cycle (indicated by arrowheads) at 5% strain. The recovery strain (upon unloading) and the permanent set (before reloading) are indicated by hollow and solid triangles, respectively, on the x-axis. The damping capacity was determined from the ratio of the damping energy (shaded area; area between the loading and unloading curve) to the stored energy (hatched area; area below the loading curve). c) Representative stress-strain curve (n = 7) of a fiber subjected to progressive loading cycles at 2.5% strain intervals up to failure. The damping energy, indicated by the shaded areas between the paired loading-unloading curves, increases with every loading cycle. d) The evolution of damping capacity, recovery strain and permanent set with applied strain. Linear fits to the data points are shown.

cotton and silks are efficient at absorbing or dissipating most of the energy (Figure 5.12). We subjected the fiber to a single load-unload-reload cycle (see Figure 5.11b). It is evident that the supramolecular fiber has a high damping capacity of 64.2 ± 2.2% (n = 7), which is even higher than biological silks and comparable to viscose (Figure 5.12). Furthermore,

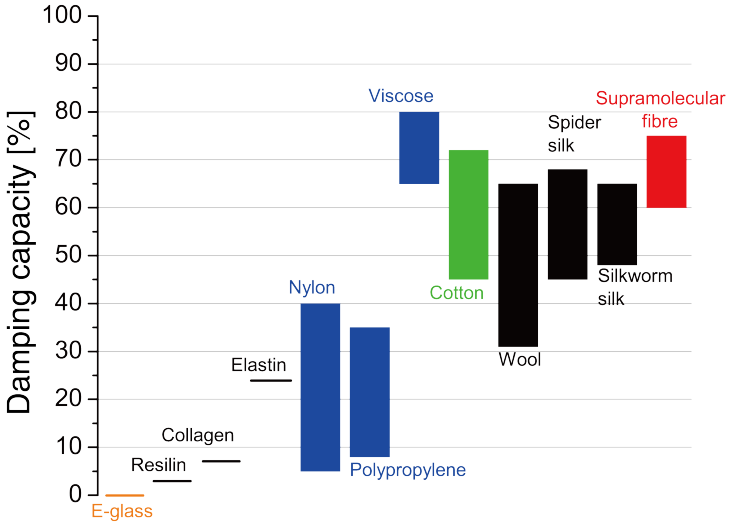

Figure 5.12: **Comparison of the mechanical properties of our supramolecular fiber (red) with other typical technical fibers.** The damping capacity of the supramolecular fiber exceeds that of biological silks and is comparable to viscose, making it a good candidate for energy-absorption applications.

we find that the coefficient of variation in the damping capacity of our supramolecular fiber was significantly lower at only 3%, in comparison to that of all other mechanical properties (ranging between 30 to 50%). Thus, damping capacity in our case is more directly related to the molecular structure of the fiber.

From further tests, we observed that damping energy as well as damping capacity reduced with respected cycles of loading-unloading: from 67.2 $\pm$ 5.3% in the first cycle to 31.2 $\pm$ 2.8% by the fifth cycle, with the major drop (of 60%) occurring between the first and second cycle (Figure 5.14). Essentially, by subjecting the supramolecular fiber to multiple cycles at the same applied strain it was transformed from being effective at energy dissipation to a material efficient at energy recovery and storage. Interestingly, this behavior has also been observed for spider silks whose damping capacity drops from around 68% in the first cycle to as low as 37% in subsequent cycles.[206] When the supramolecular fiber was subjected to progressive loading-unloading cycles until failure, the damping energy was observed to increase with every cycle (Figure 5.11c). Notably, while the damping capacity increased from 30 to 65% in the range of 2-3% applied strain (*i.e.* after the first cycle), it was remarkably stable at 66% for all other cycles of applied strain ranging between 3-20% (n = 7, Figure 5.11d). Again, such a profile has also been observed for

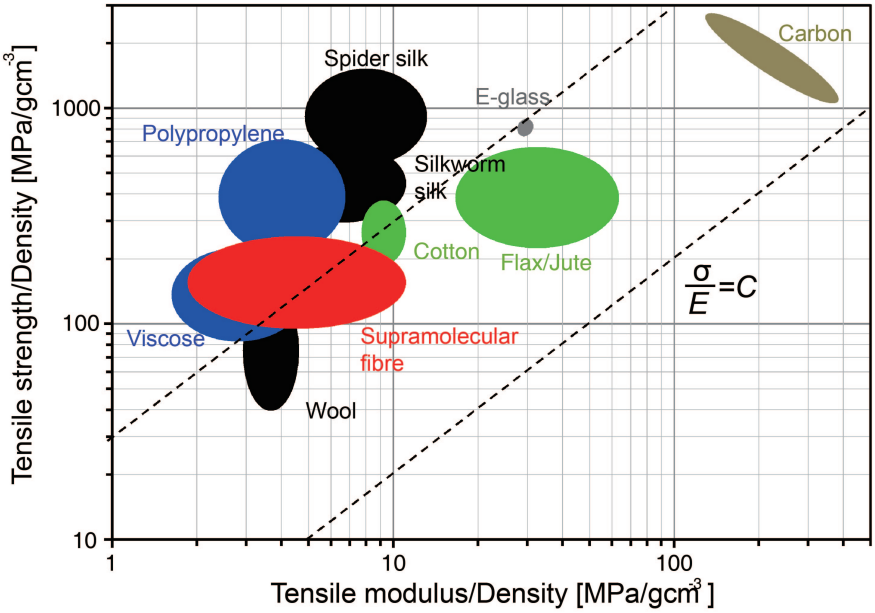

Figure 5.13: Ashby plots comparing specific (i.e. per unit density) tensile strength and modulus. The supramolecular fiber has a specific modulus ranging between 2 and 10 GPa·g·cm^{-3} and specific strength of 80–240 MPa·g·cm^{-3}. Synthetic and protein polymer fibers, whose properties are also dominated by intermolecular bonding, naturally have properties more comparable to our fiber. In particular, the supramolecular fiber exhibits a better specific modulus than conventional regenerated textile fibers such as cellulose-based viscose, and protein-based artificial silks as well as animal and human hair.

spider silks, whose damping capacity is low (at 5 to 30%) in the first cycle at 5% applied strain, but increases to 30 to 70% in subsequent cycles of increasingly applied strain.[207] The recovery strain and permanent set (permanent deformation) were also found to increase linearly with the applied strain (applied deformation) in every cycle up to failure (Figure 5.11d).

We envision that the remarkable damping performance of the supramolecular fiber arises from energy dissipative mechanisms provided by a complex structure of 'hard' (crystalline) and 'soft' (amorphous) phases at the molecular scale (*vis.* semi-crystalline **H1** polymer, Figure 5.4h), like in spider silks[206,208]. While the soft phase is always active, the hard phase is strain-activated, and undergoes a partly-reversible transformation to the soft phase *via* a process of strain-induced hydrogen bond breakage when stretched to its limit, which is accompanied by the unravelling, aligning and slipping of molecular chains. The energy stored during loading in the previous process is (partly) released

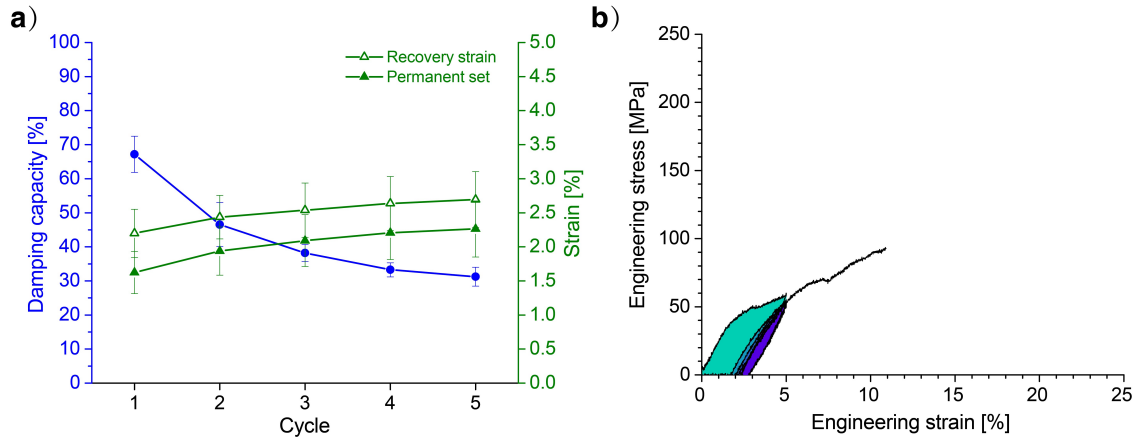

Figure 5.14: a) Representative stress-strain curve (n = 7) of a fiber subjected to multiple (five) loading-unloading cycles at 5% strain. b) The evolution of damping capacity (solid blue circles), recovery strain and permanent set with each cycle.

during unloading, by the reformation of hydrogen bonds and reverse-transition of soft phases to hard phases, as well as de-alignment or coiling of molecular chains. Consequently, the fiber finds itself in a new molecular conformation at a non-zero recovery strain (Figure 5.11b)[206,208]. In the case of our supramolecular fiber, 'hard' and 'soft' phases exist beyond the molecular scale of the semi-crystalline **H1** polymer, at the intermolecular scale (where CB[8] provides dynamic cross-links between **P1** and **H1**), as well as at the colloidal scale (silica NPs in the **SPCH**, Figure 5.4h).

5.3 Conclusion and Future Work

We have shown a novel means of assembling hierarchical supramolecular polymer-colloidal hydrogels (**SPCH**) based on CB[8] host-guest chemistry. By introducing functional polymer grafted silica NPs, we successfully modified the internal structure of the gel at the nanoscale and benefit from the semi-crystalline nature of **H1**, which allow for significant enhancement of the elasticity of the material. We have reported for the first time a 'supramolecular fiber' drawn from an extremely high water-content **SPCH** at room temperature. The synthetic biocompatible fiber exhibits a unique combination of strength and high damping capacity that can be readily manipulated through a detailed understanding of the hierarchical assembled structure and the underlying CB[8] host-guest chemistry. We

envision that by altering the chemistry and processing methods of **SPCH**, a family of supramolecular fibers with a whole range of tuneable properties can be produced at low temperature taking us a considerable step closer to sustainable fiber technology.

5.4 Experimental Appendix

5.4.1 Materials and General Methods

All starting materials were purchased from Alfa Aesar and Sigma Aldrich and used as received unless stated otherwise. MV-Hex isocyanate and CB[8] were synthesised as previously reported.[34,120] N-Hydroxyethyl acrylamide was purchased from Sigma-Aldrich and was passed through a column of silica gel and purged with high purity nitrogen for 1 h prior to use. 2-naphthyl isocyanate, triethylamine were purchased from Alfa Aesar. N-Isopropylacrylamide, 2-bromoisobutyryl bromide, tetraethyl orthosilicate, tris(2-dimethyl aminoethyl)amine, copper (II) chloride, hydroxyethylcellulose were purchased from Sigma-Aldrich. Silica Nps, the surface ATRP initiator, MV-Hex isocyanate and CB[8] were synthesised as previously reported. Solvents and reagents were used without further purification.

^{1}H NMR (500 MHz) spectra were recorded using a Bruker Avance BB 500. Chemical shifts are recorded in ppm (δ) in D_2O with the internal reference set to δ 4.79 ppm. ATR FT-IR spectroscopy was performed using a Perkin-Elmer Spectrum 100 series FT-IR spectrometer equipped with a universal ATR sampling accessory. UV-*vis* studies were performed on a Varian Cary 4000 UV-*vis* spectrophotometer. Transmission electron microscopy (TEM) characterisation was carried out on a FEI Philips Tecnai 20 TEM under an accelerating voltage of 80 kV. Samples were prepared by applying one drop of the as-synthesized microspheres onto a Holey R carbon coated copper TEM grid (400 mesh) drying overnight. Dynamic light scattering (DLS) and zeta potential (ZP) measurements were performed on Malvern Zeta-sizer NS90 instrument. Gel permeation chromatography (GPC) was carried out in DMF (dimethylformamide) with 0.1 M of LiBr on a JordiX-stream H_2O 10^3 Å glucose column with a Shimadzu SPD-M20A prominence diode array detector. Samples were filtered over 0.45 μm PTFE filters before injection using a 0.7 mL·min^{-1} flow rate. The system was calibrated with Poly(methyl methacrylate) (PMMA) standards.

5.4.2 Preparation of Poly(Nipam-co-HEAm-MV) Grafted Silica NPs (P1)

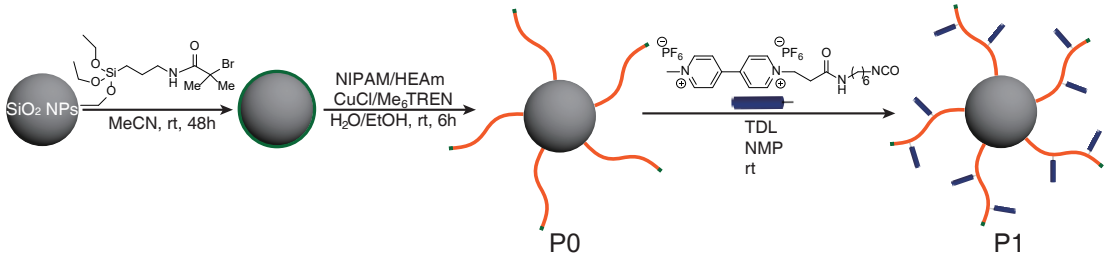

Figure 5.15: Synthetic scheme for the preparation of poly(NIPAm-*co*-HEAm-MV) grafted silica NPs, **P1**.

The synthesis of **P1** was accomplished *via* surface initiated atom transfer radical polymerization[60,209,210] (Figure 5.15). Firstly, ammonium hydroxide (25 wt% in water, 25 mL) and ethanol (500 mL) were added into a two-necked round-bottom flask at ambient temperature; the mixture was stirred at a speed of 300 rpm. A mixture of tetrathoxysaline (TEOS, 12.5 mL) and ethanol (14 mL) was added into the flask at a rate of 1 mL/min through a dropping funnel. After stirring 20 h at room temperature, the nanoparticles were isolated by centrifugation at 8000 rpm. After discarding the supernatant, the sediments were redispersed in ethanol and centrifuged again. This purification cycle was repeated for four times. The obtained silica NPs were then dispersed and stored in 50 mL of ethanol. TEM image of the silica NPs is shown in Figure 5.16.

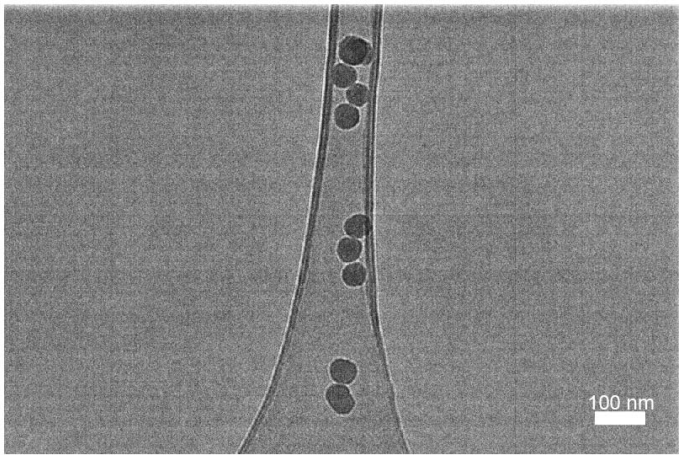

Figure 5.16: TEM image of bare silica NPs.

To synthesize the ATRP initiator, 2-bromoisobutyryl bromide (2.79 g, 12.1 mmol) were

dded dropwise to a solution of 3-aminopropyltriethoxysilane (1.89 g, 8.55 mmol) and triethylamine (1.64 g, 16.13 mmol) in 100 mL of dry DCM. The solution was stirred for 16 h and the precipitate was filtered off. The solution was washed with diluted HCl and with deionized water, dried with magnesium sulfate, and evaporated to give a yellow oil (89% Yield). ^{1}H NMR (500 MHz, D_2O), 9.09 (d, 2H), 9.0 (d, 2H), 8.46 (q, 4H), 7.56 (d, 2H), 7.45 (d, 2H), 6.77 (dd, 4H), 5.85 (t, 4H), 5.37 (d, 2H), 4.46 (s, 1H).

Functionlisation of silica NPs dispersed in acetonitrile was achieved by adding 1.5-fold excess of Atrp initiator for 18 h under N_2 atmosphere at room temperature. The particles were isolated *via* centrifugation and washed by three cycles of centrifugation and resuspension in acetonitrile to remove unreacted initiator.

To synthesize **P0**, NIPAM (4.06 g, 36 mmol), HEAm (0.46 g, 4 mmol) Me_6TREN (6.02 μL, 0.017 mmol) were added to a solution of H_2O/EtOH (4 mL, *v:v* = 1:1),. The mixture was purged with Nitrogen for 15 min, CuCl (1.8 mg, 0.017 mmol) was added subsequently under nitrogen protection. The reaction was initiated by injecting Initiator-functionalised silica NPs dispersed in 3 mL EtOH (24 mg, 0.01 mmol of initiating sites). An aliquot of the reaction mixture (0.2 mL) was withdrawn after 6 h, which was exposed to air and divided into two parts. One part was roughly dried under gentle N_2 flow and dispersed in D_2O for the determination of monomer conversions by ^{1}H NMR analysis. The remaining part was subjected to centrifugation and then treated with hydrofluoric acid to cleave the grafted polymer chains for further GPC analysis. The polymer (**P0**, Figure5.17) was purified by dialysis for 5 d and freeze dried.

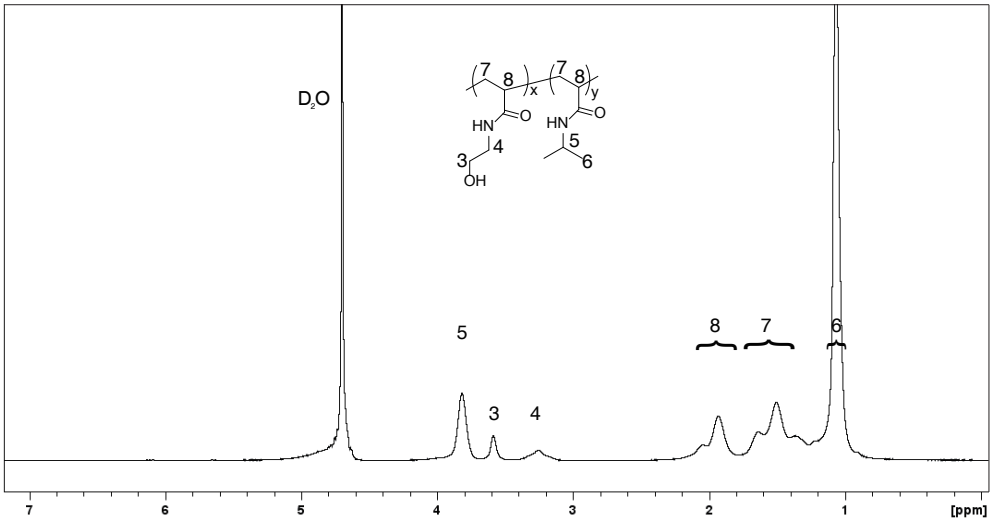

Figure 5.17: ^{1}H NMR spectrum of polymer **P0**: polyNIPAM-*co*-HEAm grafted silica NPs.

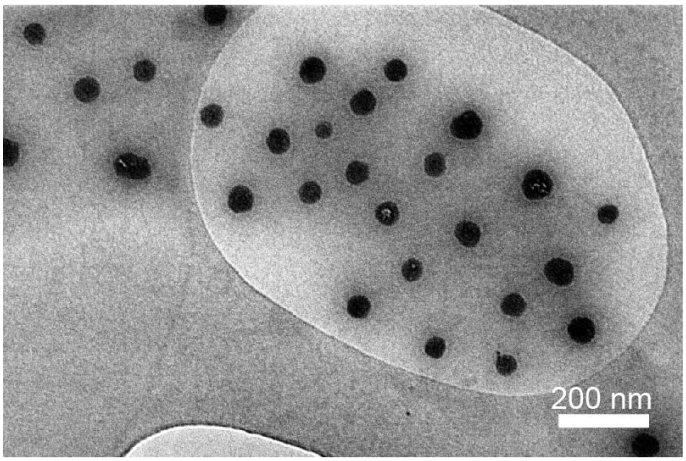

Figure 5.18: TEM image of the **P0**.

Finally, **P1** was synthesized by functionalizing **P0**. To a solution of MV-Hex-NCO di(hexafluorophosphate) (91 mg, 0.0645 mmol) in 10 mL anhydrous NMP was added **P0** (100 mg, 0.043 mmol of OH groups) dissolved in 10 mL anhydrous NMP. The reaction was stirred for 24 h at room temperature. The crude mixture was purified by dialysis in water containing 1 wt% of NaCl for 5 d. The product was freeze-dried yielding the title compound as a fluffy, yellow solid (92 mg, 76%).

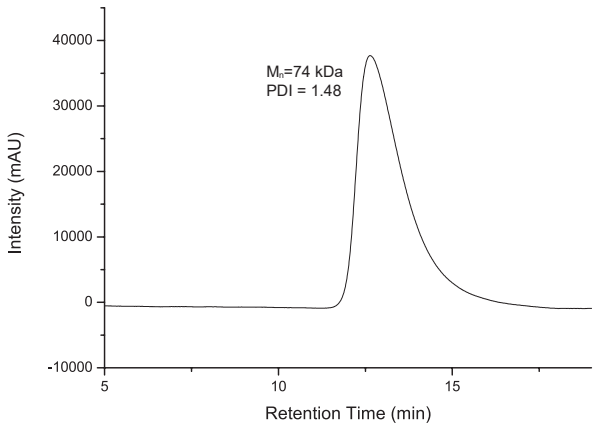

Figure 5.19: GPC trace for polymer **P1** polyNIPAM-*co*-HEAm.

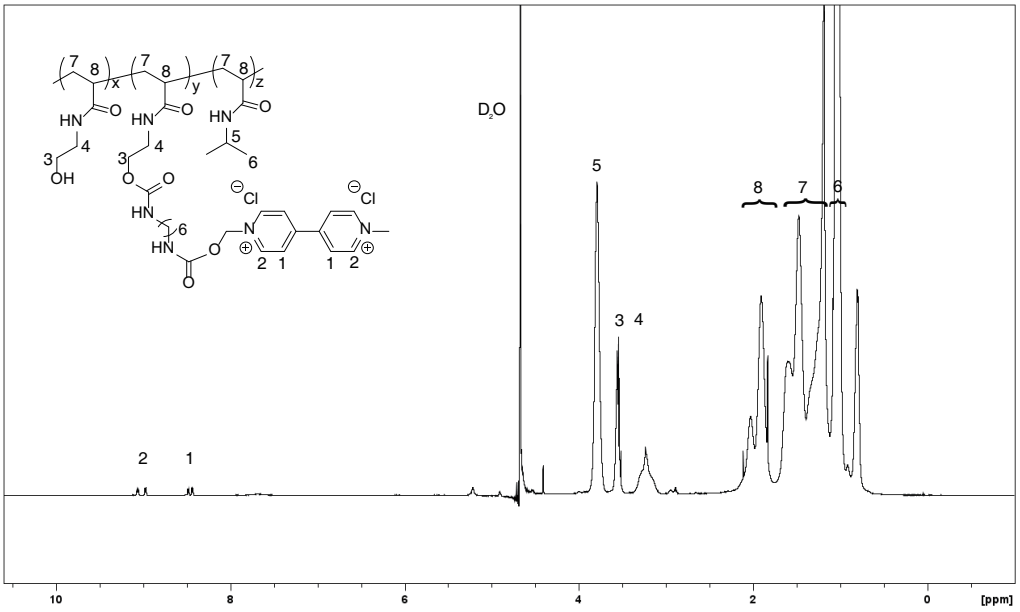

Figure 5.20: ^{1}H NMR spectrum of polymer **P1**: polyNIPAM-*co*-HEAm-MV grafted silica NPs.

5.4.3 SPCH Preparation

SPCH were prepared by first dissolving **P1** polymers in water (20 mg mL^{-1}) with stirring followed by addition of CB[8] (5 mg mL^{-1}). **H1** polymer was then dissolved in water (20 mg mL^{-1}) with stirring. **P1** polymer solution (0.2 mL) and **H1** polymer solution (0.2 mL) were then added together and mixed well by vortex.

5.4.4 Further Rheological Studies

Rheological characterisation was performed using an ARES-LC controlled strain rheometer fitted with a water bath set to 25 °C. Strain sweep measurements were performed at a frequency of 10 rad/s. Frequency sweep measurements were performed at a 5% strain amplitude. All measurements were performed using a 25 mm parallel plate geometry set to a gap height of 0.75 mm and analyzed using TA Instruments and TA Orchestrator software.

5.4.5 SEM Studies of SPCH

Cryogenic scanning electron microscopy (SEM) images were obtained using a FEI Verios 460 variable pressure SEM using and InLens detector. To prepare samples for imaging 0.1 mL of gel was transferred to a sample stub and then plunged into a slushy (liquid and solid) nitrogen bath. The frozen samples were fractured with a sharp blade and then transferred to an EM VCT100 vacuum cryo-transfer system (Leica Microsystems, Inc.) to remove surface water by controlled specimen sublimation. The samples were sputter coated with a thin layer of platinum and palladium metals prior to imaging.

5.4.6 Mechanical Test of Supramolecular Fiber

Sample preparation for testing of fibers involved, firstly drawing fibers to lengths between 25 and 250 mm. Segments of around 50 mm were then carefully obtained from the middle section, ensuring the fiber was not stretched. These segments were placed on and attached to laser-cut card frames (Figure 5.21) using a cyanoacrylate adhesive. The frames set the test gauge length (at 5, 10 or 20 mm). Before testing, the average diameter of each sample was obtained from three measurements along the gauge length using an optical microscope.

For testing, the frames were first loaded onto an Instron tensile testing machine equipped with a calibrated 5 N load cell (Figure 5.21a). Upon clamping the card frame between the grips (Figure 5.21a), the sides of the frame were cut (Figure 5.21b), and the fiber was subjected to specific loading regimes:

i) Quasi-static tests to failure at an extension rate of 1 mm/min. A total of n = 50 samples were tested: 11 at a gauge length of 5 mm, 31 at a gauge length of 10 mm (in three separate batches), and 8 at a gauge length of 20 mm.

ii) Single load-unload cycle to 5% applied strain and subsequent reloading to failure at a constant extension rate of 1 mm/min. A total of n = 7 samples were tested at a gauge length of 20 mm.

iii) Multiple (five) load-unload cycles to 5% applied strain and subsequent reloading to failure at a constant extension rate of 1 mm/min. A total of n = 7 samples were tested at a gauge length of 20 mm.

iv) Progressive load-unload cycles, increasing the applied strain by 2.5% with every cycle (e.g. cycle 1 to 2.5%, cycle 2 to 5%, cycle 3 to 7.5% and so on) until failure at a constant extension rate of 1 mm/min. A total of n = 7 samples were tested at a gauge length of 20 mm.

All tests were carried out under ambient conditions (18-20 °C and 50-60% relative humidity). Load-displacement curves were obtained, where displacement was determined from the crosshead displacement. Thereafter, engineering stress-strain plots were produced and used to determine initial elastic modulus (in the strain range of 0-1%), failure strength and strain. For quasi-static tests, the toughness was calculated from the total area under the stress-strain curve. For cyclic tests, for each cycle, i) damping capacity was determined from the ratio of the damping energy (area between the loading and unloading curve) to the stored energy (area below the loading curve), ii) recovery strain was denoted as the highest strain in the unloading curve that produced zero engineering stress, and iii) permanent set was denoted as the lowest strain in the reloading curve that produced a positive engineering stress.

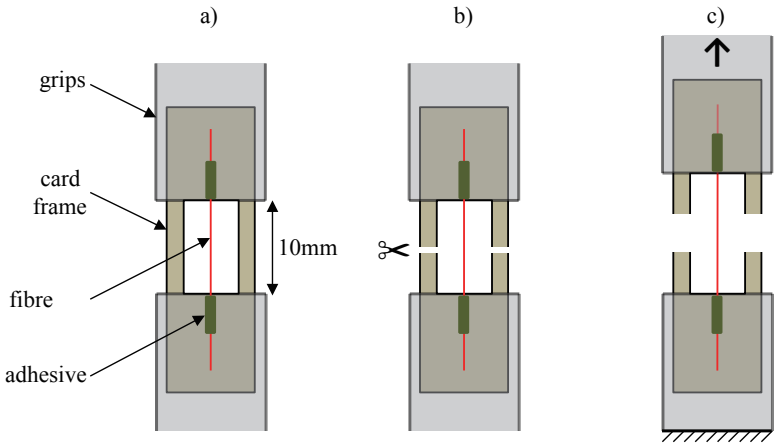

Figure 5.21: Schematic of fiber testing method: a) card frame with mounted fiber is clamped between grips on a testing machine, and then b) sides of the frame are cut, and c) the fiber is thereafter tested in tension.

Table 5.1: Summary of static tensile properties of the hydrogel fiber. See methods for detail on measurement (n = 50).

	Diameter [μ·m]	Initial modulus [G·Pa]	Tensile strength [M·Pa]	Failure strain [%]	Toughness [MJ/m^3]
Mean	7.3	5970	193	18.1	22.8
Standard deviation	2.0	2870	54	5.7	10.3
Coefficient of variation	0.27	0.48	0.28	0.31	0.45

Video S1 | Video of drawing supramolecular polymer-collodial hydrogel (**SPCH**) into a hydrogel filament.

Video S2 | Video of control hydrogel assembled between **LP@**CB[8] (1 wt%) and **H1** (1 wt%), which does not show elasticity.

Chapter 6

Biomimmetic Contractile Fiber

Spider silk is a fascinating material, combining high strength and elasticity that outperform most artificial fibers. Another intriguing feature of spider silk is its ability to 'supercontract' when exposed to water, shrinking up to 50%. This is likely on account of the entropy-driven recoiling of secondary structured proteins when water penetrates the spider silk. In contrast, humidity driven contraction in synthetic fibers is complicated to achieved. Here, inspired by the spider silk model, we report a supercontractile fiber (SCF) with contraction up to 50% of its original length at high humidity, comparable to spider silk. The fiber exhibits up to 300% uptake water by volume, confirmed under the environmental scanning electronic microscopy (ESEM). More interestingly, the SCF exhibits tunable mechanical properties at a varying humidity environment, which is reflected on the prolonged failure strain and the reversible damping capacity. Essentially, this resembles spider silks and is likely on account of the double-network in the fiber matrix. This novel fiber material provides a new opportunity of fabricating biomimetic muscle for diverse applications.

This work has been published in the following peer-reviewed journal articles:

- **Wu, Y.**; Shah, D. U.; Wang, B.; Ramage, M. H.; Scherman, O. A.* "Biomimetic suprecontracted fiber". (submitted)

6.1 Introduction

Natural systems frequently exploit intricate multiscale and multi-phase structures to achieve functionalities beyond those of man-made systems.[211–213] For example, spider dragline silk tends to outperform other natural fibers and most man-made filaments.[214,215] More interestingly, spider silk is able to 'supercontract' in high humidity, with contraction up to 50% of its original length.[216–218] Supercontraction is thought to be induced by the entropy-driven revoiling of molecular chains.[219–223] In analogy, most man-made fibers undergo thermal induced shrinkage and a variation in mechanical properties.[224,225] Humidity driven contraction in synthetic fibers is rarely seen on account of a 'frozen' molecular network in the fiber. In chapter 5, we have demonstrated drawing a surpamelecular fiber from a self-assembled multi-phase hydrogel at high water content (98%).[226] The fiber exhibits a good combination of tensile properties as well as damping capacity. More importantly, the underlying structure of the hydrogel can be readily manipulated to produce novel fiber materials with emerging properties.

Herein, inspired by the spider silk model, we report a supercontractile fiber (**SCF**) as a continuation of Chapter 6, which is capable of contracting up to 50% of its original length at high humidity, comparable to spider silk (Figure 6.1). In comparison to the supramolecular fiber (previously shown) where its polymer matrix is held by physical interactions, the **SCF** is imparted with a second network of covalent cross-links *via* UV treatment. The resulting **SCF** is not only resilient to water, but also shows stimuli-responsiveness in high humidity. The fiber exhibits up to 300% uptake water by its volume at high humidity, confirmed under the environmental scanning electronic microscopy (ESEM). Moreover, the **SCF** undergoes a cyclic relaxation-contraction response to wetting and drying, similar to spider silk. This type of fiber material provides a new opportunity of fabricating biomimetic muscle for diverse applications, ranging from humanoid robots, prosthetic limbs, and exoskeletons.

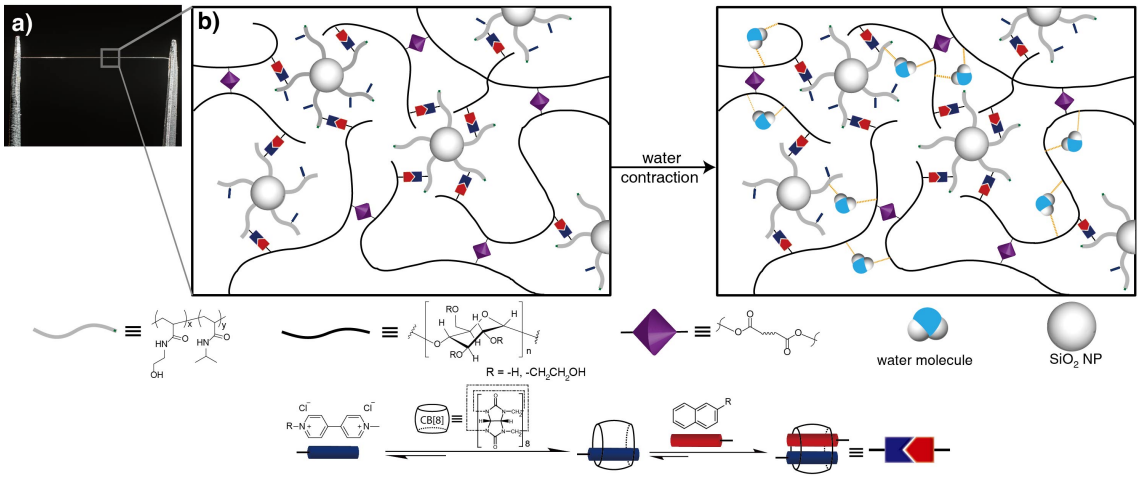

Figure 6.1: a) Photograph of the super-contractile fiber (**SCF**). b) schematic illustration of **SCF** undergoes super-contraction at high humidity. Water molecules penetrate into the fiber matrix and interact with the hydrophilic moieties. The covalent cross-linkers ensure the stability of wet fiber, while the dynamic cross-linkers enable the movement of polymer chains. Thus, water induces the polymer chains to reconfigure toward higher entropy and cause the entire fiber to contract.

6.2 Results and Discussion

Fabrication of SCF

The fabrication of **SCF** was accomplished in two consecutive steps. Fibers were initially drawn from a hydrogel composite (**H1**), followed by a UV treatment at room temperature. **H1** is primarily held by host-guest interactions of cucurbit[8]uril (Figure 6.2), consisting of methyl viologen (MV) functionalised polymer-grafted silica nanoparticles (**P1**, 1 wt%), a napthol (Np) functionalised hydroxyethyl cellulose (**P2**, 1 wt%), CB[8] (0.5 wt%) and photoinitiator (I2959, 0.1 wt%). The constituents serves different purposes: the CB[8] is a supramolecular macrocycle, cross-linking **P1** and **P2** in an aqueous media by forming a dynamic ternary complex with the pendant guest molecules on both polymers. This induces the desired viscoleatstic behaviour required for direct drawing fiber with a high aspect ratio from **H1**.[226] In addition, **P2** is functionalised with methacrylic anhydride (MA) for further UV cross-linking in the fiber matrix.[193] The resulting fiber is constructed by a double network, including the physical interactions between **P1** and **P2** and the covalent cross-links within **P2**.

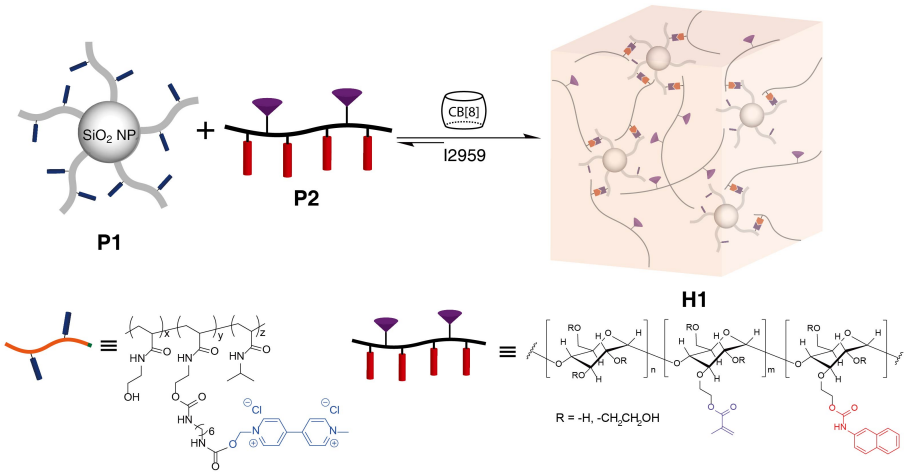

Figure 6.2: Schematic representation of a supramolecular polymer-colloidal hydrogel **H1** prepared through addition of CB[8] to a mixture of polymer-grafted silica **P1** (functionalised with MV) and a linear Np-HEC-MA **P2** in water in the presence of photoninitiator I2959.

The efficacy of UV crosslinking was studied in both hydrogel composite state and fiber state. The mechanical properties of the hydrogels were characterized with rheometric measurements. Strain dependent oscillatory rheology of the hydrogel before UV treatment displays a broad linear viscoelastic region (storage moduli G' >G", Tan $\delta \approx 0.75$, Figure S5a). After UV treatment, the value of G' increases dramatically to more than twice of its original state (Tan $\delta \approx 0.66$), indicating additional crosslinks inside the hydrogel composite (Figure S5c). Similar in frequency dependent oscillatory rheology, a large increase in G' across the whole range of frequencies was observed in the hydrogel before and after the UV treatment (Figure S5b and d). In terms of the fiber state, the success of UV crosslink was clearly demonstrated by a stability test of fiber in water. Fibres that were produced from the hydrogel without cross-linking could be easily destroyed upon rehydration on account of the fiber network held by dynamic interactions (Figure S6a). While in comparison to the fibre after UV treatment, it remained stable without any collapse in the fiber matrix as shown in Figure S6b. This further proves that the **SCF** was reinforced by additional covalent cross-links.

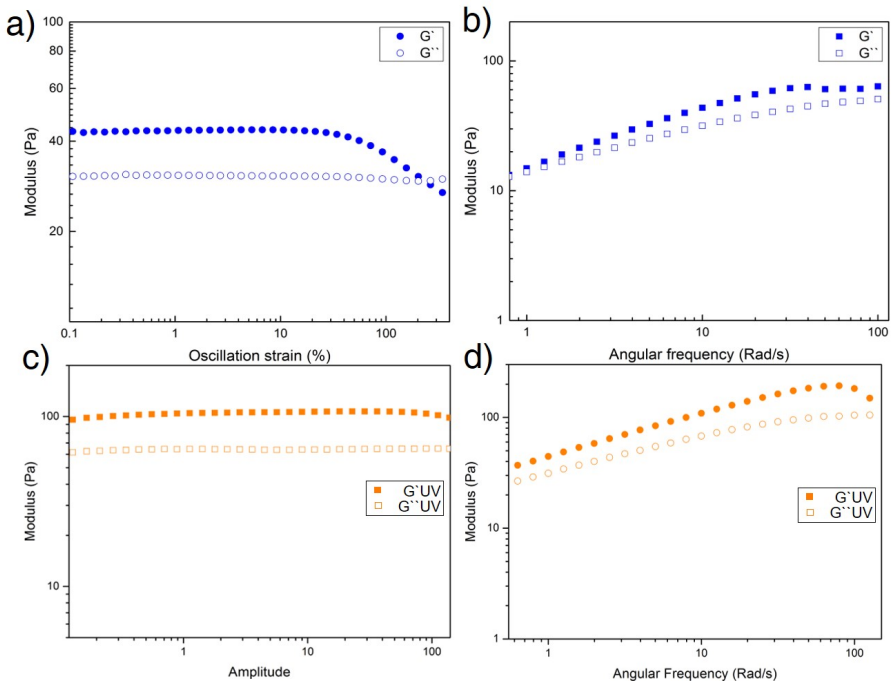

Figure 6.3: a,c) Rheological strain oscillatory rheology of **H1** before and after the UV treatment respectively (2 wt%) from 0.1% to 400% at 20 °C (w = 10 rad/s). The materials expressed broad viscoelastic regimes and resisted yielding up to 100% strain, the storage modulus of **H1** after UV treatment increased more than doubled, indicating successful UV crosslinking of **H1**. b,d) Frequency dependent oscillatory rheology of **H1** before and after the UV treatment respectively indicating gel-like behaviour, the increase in storage modulus of **H1** after UV treatment corresponds to the similar trend.

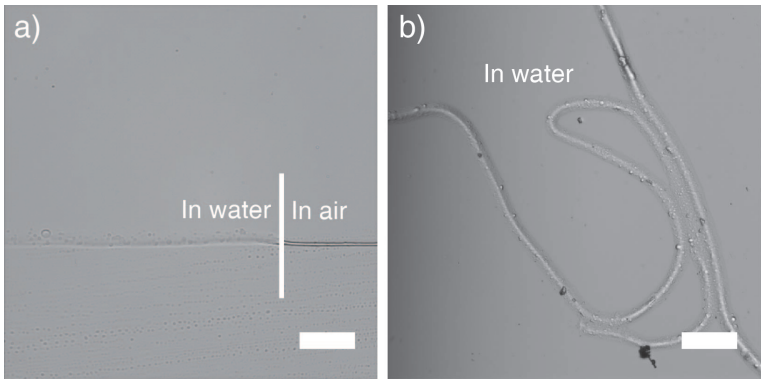

Figure 6.4: Stability test of fibers in water, micrograph of a) pre-treated fiber with collapsed fiber matrix in water (scale bar is 30 μm); b) UV treated fiber in water illustrating the effective cross-linking within the fiber matrix (scale bar is 100 μm).

Interestingly, the **SCF** was observed to contract in length at high humidity, similar to spider silks. As shown in Figure 6.5, upon introducing high humidity, the **SCF** contracts itself from an original length of 2 cm to 1.1 cm. The contraction could achieved up to 50% (average 42%), and it is independent with the diameter of the fiber (Figure6.6). ESEM was used to investigate the structure of the **SCF** with respect to humidity variation in an effort to explain its contraction behaviour. Figure 6.5c depicts a section of the fiber (Diameter: 6.53 μm) at a relative humidity of 53%. As the humidity increased (97%), the

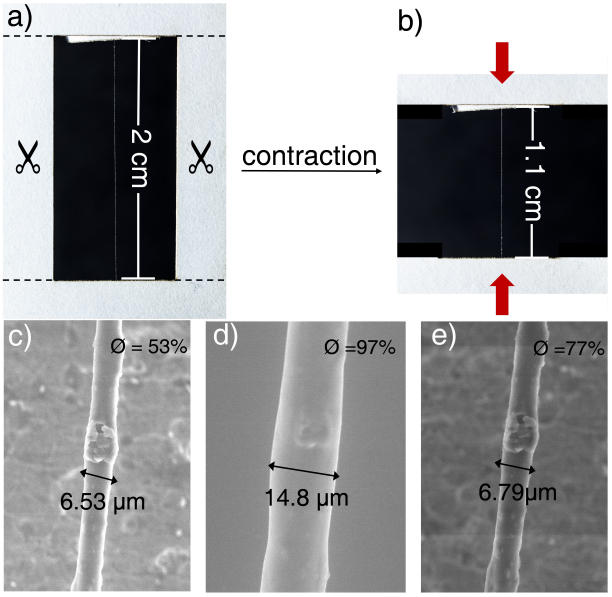

Figure 6.5: a-b) Photographs of **SCF** undergoing super-contraction at high humidity, over 40% (scale bar: 2 cm). **c-e** Environmental SEM images of the **SCF** at different humidity, difference in diameter indicating different amount of water uptake inside the **SCF**.

diameter of fiber expanded significantly to 14.82 μm (Figure 6.5d). By calculating the net volume of the fiber, we could estimate the volume of water uptake (1.4 nL/cm). This represents a large amount of water penetrated into the fiber matrix within seconds without breaking the fiber network. Furthermore as the relative humidity dropped (Figure 6.5e), the diameter of the swelled fiber decreased accordingly, indicating reversible process of water uptake and release (see video S1 for more details). This is possibly on account of the co-existence of a dynamic network inside the fiber, including the polymer chain entanglement, slipping and the host-guest interactions of CB[8]. In addition, the **SCF** could

not contract when it is immersed in a non-polar solvent, such as toluene, though organic solvent would also cause the **SCF** to swell (Figure 6.7). Therefore, the contraction of

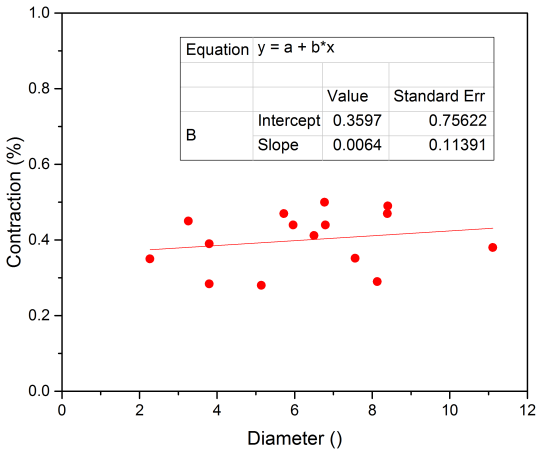

Figure 6.6: The distribution and correlation between the fiber diameter and their contraction percentage in water (n = 15). There was no correlation (R^2 = 0.002) between fiber diameter and draw length.

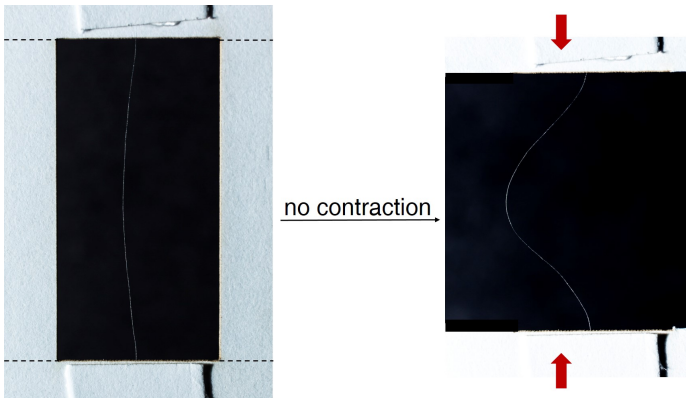

Figure 6.7: Photographs indicating **SCF** could not contract after it is immersed in toluene.

SCF could be attributed to its uptake of water at high humidity. When water molecules penetrate into the fiber matrix, they disrupt the hydrogen bonding within the polymer chains. This disruption does not cause any collapse or breakage of the **SCF** on account of the cross-linked fiber network. Yet it is sufficient to allow the polymer chains to reconfigure toward higher entropy and causing the entire **SCF** to suddenly contract in length while expanding in overall volume. The **SCF** now behaves like a filled rubber with a

relatively low modulus, which is confirmed by the mechanical tests. Interestingly, this hypothesized model has also been proposed similarly in spider silks.[216]

6.2.1 Characterisation of SCF

The cross-linking of the supramolecular fibers prevents them from re-solubilising in water, and also imparts changes in mechanical properties. Tensile tests reveal that the **SCF** have a significantly lower modulus and strength in comparison to the uncross-linked fibers, with the failure strain remaining unchanged (experimental appendix Figure 6.15). Furthermore, changes in cross-link density, resulting from altering UV cross-linking duration lead to similar observations (experimental appendix Figure 6.15). The reduction in modulus and strength with cross-linking is presumably a result of competitive action from a number of factors. Firstly, cross-links may have a defect trapping effect,[227] the presence of internal voids, which may be locked during cross-linking and act as microcrack during tensile loading, has been observed.[226] Secondly, cross-linking may cause initial diminution of the crystallinity of the system and introduce flexible moieties, both of which have been shown to decrease the modulus of polyvinyl alcohol.[228] In relevance to this study, PVA is a semi-crystalline polymer that can be used as an alternative to HEC to produce such supramolecular fibers.[226] Thirdly, the formation of a chemical network through cross-links may alter the molecular stretching behaviour, for example by restricting some of the dynamic mechanisms associated with the non-covalent interactions of an uncross-linked fiber. Having said this, crosslinking also imparts better control and tunability in properties, for example a range of stress-strain profiles can be generated (experimental appendix Figure 6.15) by altering the degree of cross-linking.

The cross-linked 'dry' fibers have stiffness, strength and failure strain of 3.2 GPa, 110 MPa and 22%, respectively. Like spider silks, the **SCF** exhibits substantial super contraction at ambient conditions in the presence of water. In addition, the water substantially alters fiber mechanical properties, with 'wet' fibers exhibiting low strength of 25 MPa, and high failure strains of 35% (Figure 6.8, experimental appendix Figure 6.16). An envelope of stress-strain profiles is observed, with varying moisture content and therefore physical structure, having a unique stress-strain response. Intriguingly, this mimics the property response of spider silks with water (and degree of super-contraction, also referred to as 'coefficient of shrinkage – Csh').[219] Furthermore, we observe that 'redrying'

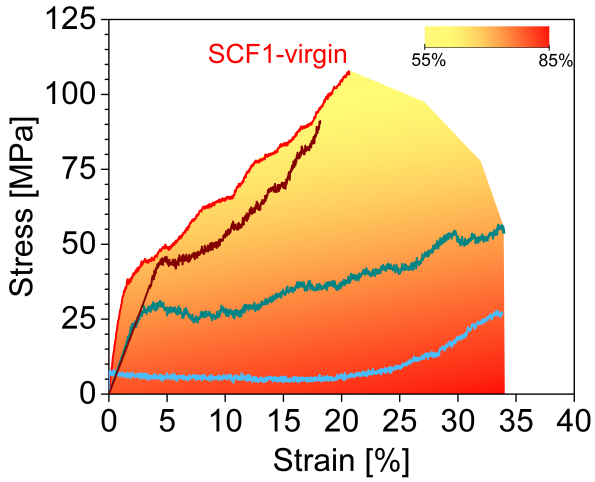

Figure 6.8: Tensile stress-strain response of SCF1 tested at various humidity levels. See Figure 6.16 for comparison between initial modulus, strength and failure strain.

of wetted fibers resets the fiber properties to the initial virgin 'dry' state (Figure 6.8, experimental appendix Figure 6.16). In essence, water induced super contraction is reversible in our fiber. We envisage that as in spider silks, water plasticises the system and increases the internal free volume, leading to improved mobility and therefore lower strengths and higher failure strains.[206,219,229,230]

In Chapter 5, we have shown the dynamic properties of supramolecular fibers (uncross-linked), with a damping capacity of 65% (in the first cycle), exceeding that of spider silk and viscose fibers. However likewise in spider silks, due to molecular rearrangement and the manifestation of a plastic permanent set, subsequent cycles led to a reduction in damping capacity, below 30% by the fifth cycle. A similar trend is also observed with the **SCF**, albeit with slightly (5-10%) higher damping capacities in comparison to the uncross-linked fibers (**UF**). Interestingly, super contraction induced by water enables the elimination of permanent set (from the previous load-unload cycle). In essence, water enables 're-setting' of the fiber properties, presumably by resetting the molecular organisation. Indeed, a damping capacity of 75% can be repeatedly obtained for every load-unload cycle by wetting (and subsequent drying) of the fiber in the dwell period. The change in damping behaviour due to water-induced super contraction is well-depicted through the

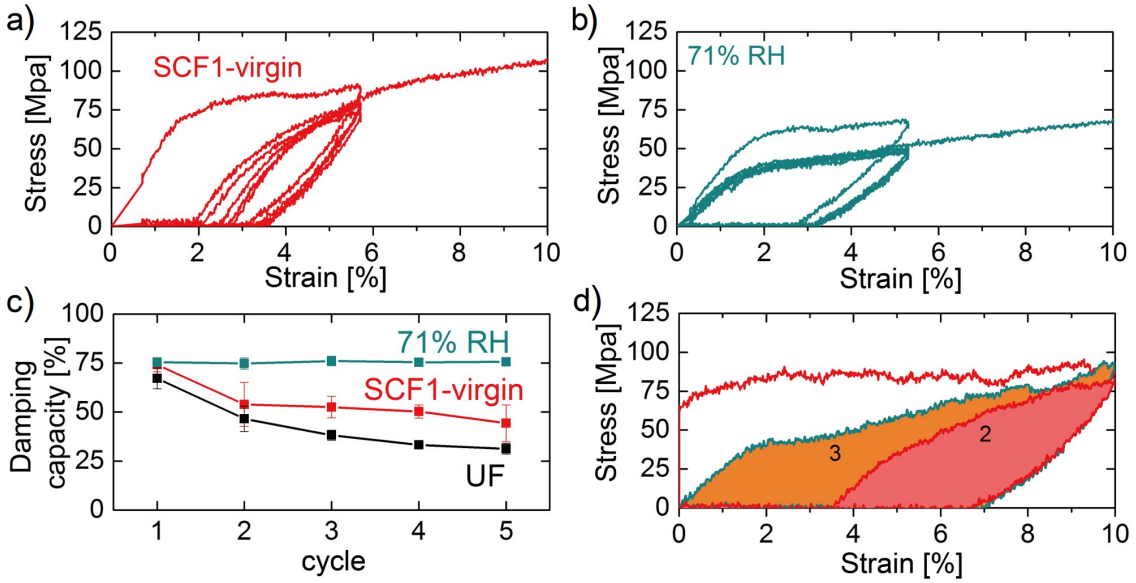

Figure 6.9: a) Cyclic response of an SCF1 virgin fibre (at RH = 55%) exhibits hysteresis loops decreasing in area with every cycle, alongside an increasing recovery strain and permanent set ('permanent' deformation). b) However, if after each unloading cycle, RH is increased to 65-70%, and the fibre is re-loaded thereafter, the fibre exhibits a 'reset' and stable response, with a constant high damping capacity at 75%, and no permanent set. c) The evolution of damping capacity (ratio of damping energy to stored energy) with loading cycles is depicted for three different fibres: uncrosslinked fibres (UF; from[226]), SCF1-virgin (at RH = 55%), and SCF1 rehydrated to 65-70% RH before every reload cycle. d) The 'reset' can be implemented at any cycle. In this case, we were able to reset the properties at every alternate cycle (3,5, and so on).

stress-strain curves in Figure 6.9a-c), where the damping energy is reducing with every cycle for the SCF1-Virgin fiber (Figure 6.9a), but that stress-strain curves are neatly overplayed on top of each other and the damping energy is constant for the resettled fibers (Figure 6.9b). Figure 6.9d shows the ability to exercise control over the damping behaviour by, for example, resetting the properties every alternate cycle through resetting. It is well-known that proteinacious spider silk dragline fibers also exhibit such tunability and control in static and dynamic properties through interactions with water.[206,219,229,230] While the evolutionary function and advantage of this is not known for spider silks,[206,231] the applications of such smart functional materials, for instance as sensors, biomedical applications, are exciting. Water is a key resource and tool in nature. Spider silks, for instance, are produced from a dope where water is a solvent, and the same water is used

by the spiders to control properties for a range of functions. Learning how to effectively use water to produce such low-energy, high-performance fibers is the key to the future of sustainable fiber processing. The work on the development of supramolecular fibers formed from hydrogels (with 98wt% water), and with properties including supercontraction, is important and pioneering scientific developments in material science. The **SCF** exhibits an average pre-stress of 20.0 $\pm$ 8.4 MPa (experimental appendix Figure 6.17), which is impressive as the stress is only generated by water. Here, by mimicking the muscle fiber, multiple **SCF**s were aligned and joined as a fiber bundle to conduct weight lifting experiments (Figure 6.10a-b). As shown in Figure 6.10c, the hanging weight is 5 mg, after spraying water to the fiber bundle, it contracted and lifted the weight up about 0.5 cm (12.5%). This is approximate 10 MPa in stress. Moreover, the weight lifting can be repeated in multiple cycles (Figure 6.10d), after reset the length of the fiber bundle.

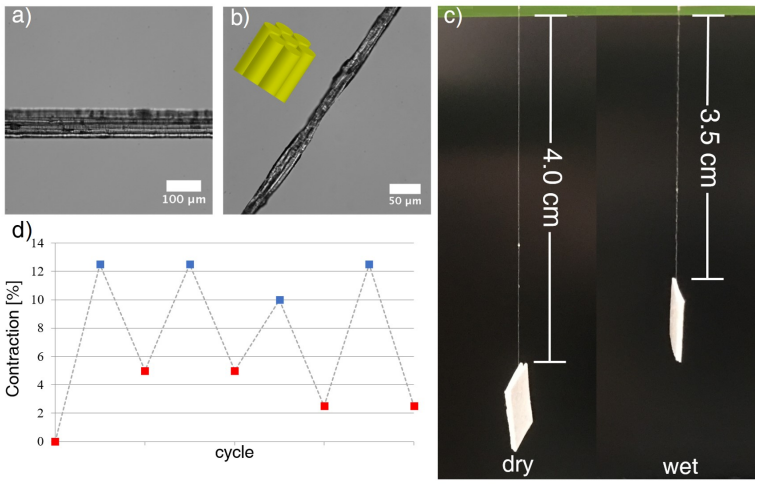

Figure 6.10: a-c) Micrograph of the **SCF** bundle, imitating a muscle fiber to lift weight (5 mg). d) Recyclability diagram of the fiber bundle showing weight lifting can be repeated in multiple cycles.

6.3 Conclusion and Future Work

Based on the work of supramolecular fibers in previous chapter, we further explored the fiber network and prepared the supercontractile fiber. By introducing the covalent cross-links to the fiber, its stability in water is significantly enhanced. The underlying

dynamic interactions allow the reconfiguration of polymer chains within the fiber matrix. The penetrated water molecules induce the contraction of the **SCF** up to 50%, which is comparable to spider silk. Moreover, similar to spider silk, the mechanical properties of **SCF** is tunable according to the humidity level. The **SCF** is a good example of developing emerging fiber materials. We envision the alteration of chemistry and processing technology offer limitless opportunities towards biomimmetic materials.

6.4 Experimental Appendix

6.4.1 Materials and General Methods

All starting materials were purchased from Alfa Aesar and Sigma Aldrich and used as received unless stated otherwise. CB[7] and CB[8] were prepared as documented previously.[34,120]

^{1}H NMR (400 MHz) spectra were recorded using a Bruker Avance QNP 400. ATR FT-IR spectroscopy was performed using a Perkin-Elmer Spectrum 100 series FT-IR spectrometer equipped with a universal ATR sampling accessory. UV-*vis* studies were performed on a Varian Cary 4000 UV-*vis* spectrophotometer. Transmission electron microscopy (TEM) characterisation was carried out on a FEI Philips Tecnai 20 TEM under an accelerating voltage of 80 kV. Samples were prepared by applying one drop of the as-synthesised microspheres onto a Holey R carbon coated copper TEM grid (400 mesh) drying overnight. Dynamic light scattering (DLS) and zeta potential (ZP) measurements were performed on Malvern Zeta-sizer NS90 instrument. Microscopic images and fluorescence images were obtained using an Olympus IX81 inverted optical microscope coupled with a camera of Andor Technology EMCCD iXonEMþ DU 897. M_w, number average molecular weight (M_n) and polydispersity (M_w/M_n) were obtained by aqueous or THF-GPC. The aqueous GPC setup consisted of a Shodex OHpak SB column, connected in series with a Shimadzu SPD-M20A prominence diode array detector, a Wyatt DAWN HELEOS multi-angle light scattering detector and a Wyatt Optilab rEX refractive index detector. The THF GPC setup consisted of two 30-cm PLgel Mixed-C columns in series,

eluted using THF and calibrated against a series of 12 near monodisperse PMMA standards (M_p from 690 to 1,944,000 $gmol^{-1}$). The polymers were analyzed in THF at a concentration of 5.0 mg $ml^{-1}1$. All calibrations and analysis were performed at 35 °C at a flow rate of $1mlmin^{-1}$. Scanning electron microscopy (SEM) images were obtained using a FEI Verios 460 variable pressure SEM using and InLens detector. The samples were sputter coated with a thin layer of platinum and palladium metals prior to imaging.

6.4.2 Preparation of supramolecular polymer-colloidal hydrogel (H1)

To prepared **P2**, synthetically acquired HEC-Np (1 g) was dissolved in 50 mL of water. Dimethylformamide (DMF, 30 mL) was added and the solution stirred until it was homogeneous. The polymer solution was then cooled to 5°C in an ice/water bath and methacrylic anhydride (740 μL, 5.00 mmol) added dropwise over a period of 15 min. The reaction mixture was removed from the ice bath and the pH maintained between 8 and 10 for 4 h by the addition of 0.5 M NaOH(aq) before being left to stir overnight. The reaction mixture was then transferred directly to dialysis tubing (MWCO 15 kDa) and dialyzed against water for 5 days. The **P2** was then obtained by lyophilization in yields upward of 70% and functionalization with methacrylate observed by ^{1}H NMR (Figure 6.12).

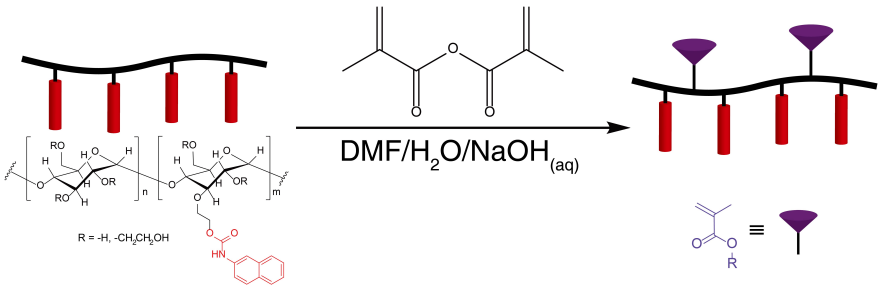

Figure 6.11: Synthetic scheme of Np-HEC-MA (**P2**).

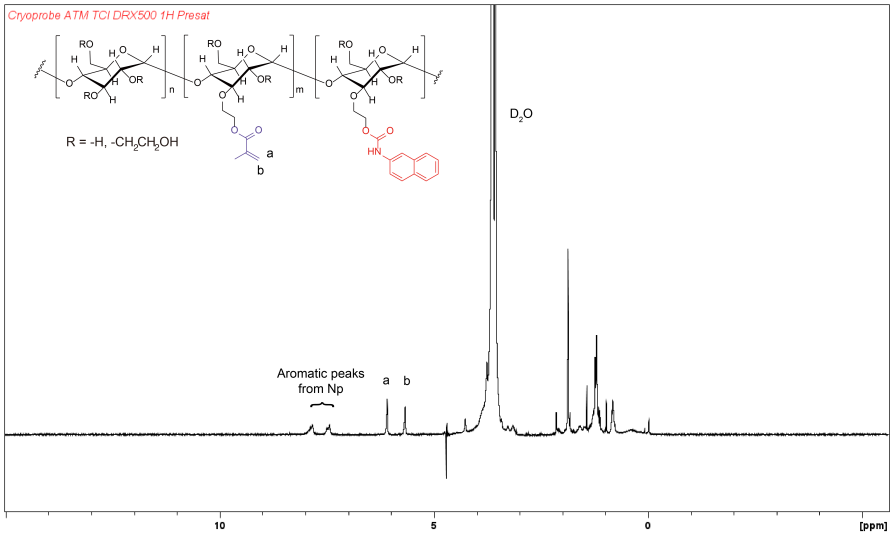

Figure 6.12: ^{1}H NMR of **P2**.

H1 was prepared by first dissolving **P1** polymers in water (20 mg mL^{-1}) with stirring followed by addition of CB[8] (5 mg mL^{-1}). **P2** polymer was then dissolved in water (20 mg mL^{-1}) with addition of a aqueous solution of Irgacure 2959 (100 μL, 1 mg/mL). **P1** polymer solution (0.2 mL) and **P2** polymer solution (0.2 mL) were then added together and mixed well by vortex in dark.

6.4.3 Preparation of supercontracted fiber

Fibers were prepared by drawing hydrogel filaments from **H1** at a steady speed (*ca.* 1 cm/min). After the fast dehyadration process, the fiber was mounted on a pre-cut paper board, the pre-treated fiber was then exposed to the UV light (350 nm) for 15 min to initiate the corsslinking between **P2** as illustrated in Figure 6.13 and 6.14.

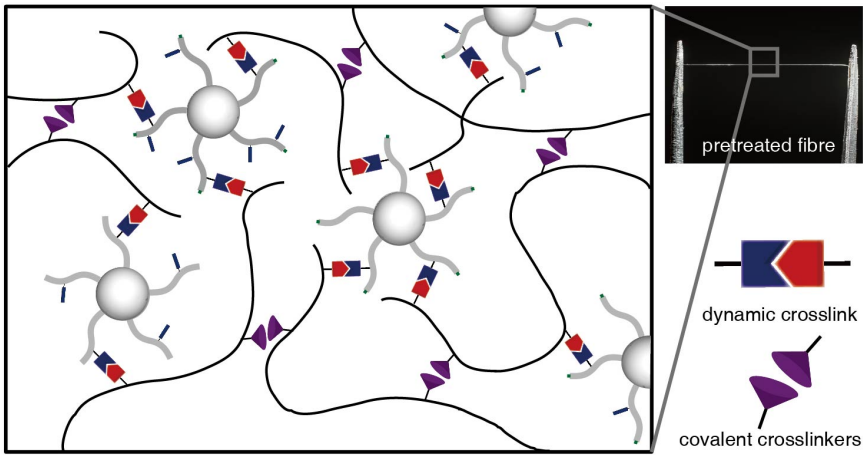

Figure 6.13: Schematic representation of the network of pre-treated fiber before UV light (350 nm) treatment.

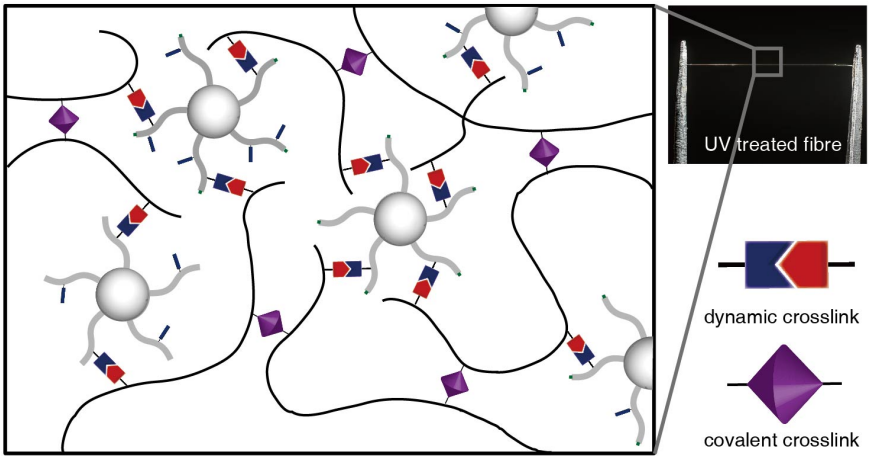

Figure 6.14: Schematic representation of the network of UV-treated fiber (wavelength = 350 nm).

6.4.4 Mechanical test of the supercontracted fiber

Fiber mechanical testing was conducted as described in Chapter 6. Sample preparation for testing of filaments involved, firstly drawing filaments to lengths between 25 and 250 mm. Segments of around 50 mm were then carefully obtained using tweezers from the middle section, ensuring the filament was not stretched. These segments were placed on and attached to laser-cut card frames using a cyanoacrylate adhesive. The frames set the test gauge length at 10 mm. Before testing, the average diameter of each sample was obtained from three measurements along the gauge length using an optical microscope.

Based on a circular cross-section, as supported by SEM images, an average cross-section area was obtained for each sample. For testing, the frames were first loaded onto an Instron tensile testing machine equipped with a calibrated 5 N load cell. Upon clamping the card frame between the grips, the sides of the frame were cut, and the filament was subjected to specific loading regimes:

i) Quasi-static tests to failure at an extension rate of 1 mm/min. UF (n = 50), SCF1 (n = 12) and SCF2 (n = 13) fiber types were tested in their virgin state in ambient conditions (T = 20 °C, RH = 55%). In addition, the SCF1 fiber type was tested at various humidity levels: at 75-80% RH (n = 8), 65-70% RH (n = 7), and 60% RH (n = 8). An Easy-Log temperature and humidity data logger (Lascar Electronics Limited, UK) was used to monitor conditions. Humidity was regulated by placing the fiber in the test chamber and spraying water into the chamber, followed by air drying for a specified time. Ambient air conditions were controlled to T = 20 °C and RH = 55%. Figure S10 and Figure S11 present the data exploring the effects of cross-linking and water on tensile mechanical properties, respectively.

ii) Multiple (five) load-unload cycles to ca 5% applied strain at a constant extension rate of 1 mm/min, with a 5 min dwell period between every reload cycle. UF (n = 8) and SCF1 (n=5) fibers were tested in their virgin state. In addition, the SCF1 fiber type was tested at 65-70% RH (n=5), where the fiber was wetted by spraying water onto it at the end of its unloading cycle and was air dried in ambient conditions during the 5 min dwell period before reloading. Furthermore, tests were done (n=3) where the SCF1 fiber was wetted-and-dried in alternate reloading cycles.

Load-displacement curves were obtained, where displacement was determined from the crosshead displacement. Thereafter, engineering stress-strain plots were produced and used to determine initial elastic modulus (in the strain range of 0-1%), failure strength and strain. For cyclic tests, for each cycle, damping capacity was determined from the ratio of the damping energy (area between the loading and unloading curve) to the stored energy (area below the loading curve). See chapter 5 for more detail.

Supercontraction stress was measured as the equilibrium compressive stress (reached

typically after 4 min) on a fiber (n=8), loaded on a card frame and held at a constant 10 mm gauge length, when wetted by spraying water. Figure S12 presents the evolution of supercontraction induced pre-stress with time.

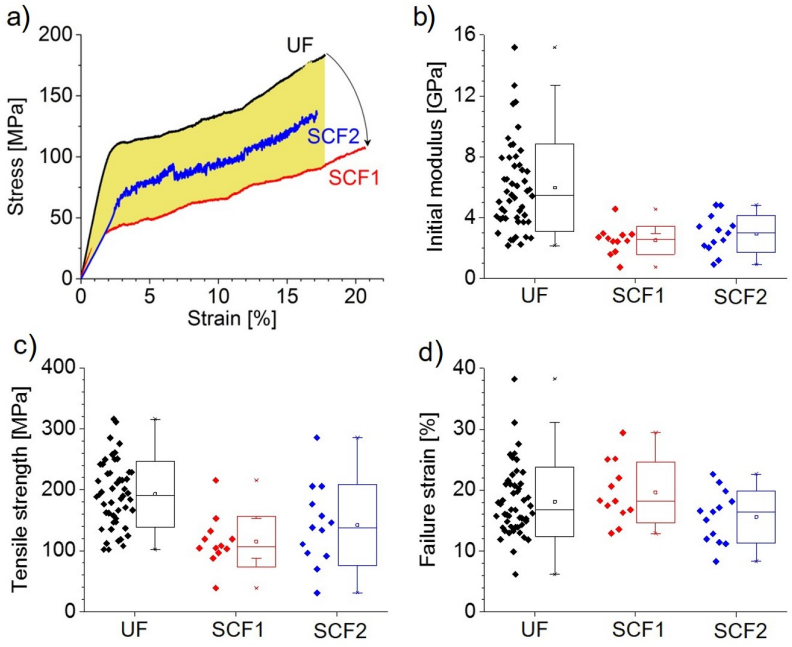

Figure 6.15: Tensile behaviour a) and properties b-d) of three supramolecular fibre varieties. UF are uncrosslinked fibres, which solubilise in contact with water. The crosslinked fibres (SCF1 and SCF2) maintain their fibre structure, but exhibit supercontraction. SCF2 fibres were crosslinked over a shorter duration. Box plots show maximum and minimum (whiskers), upper and lower quartiles (box range), median, and mean (unfilled square).

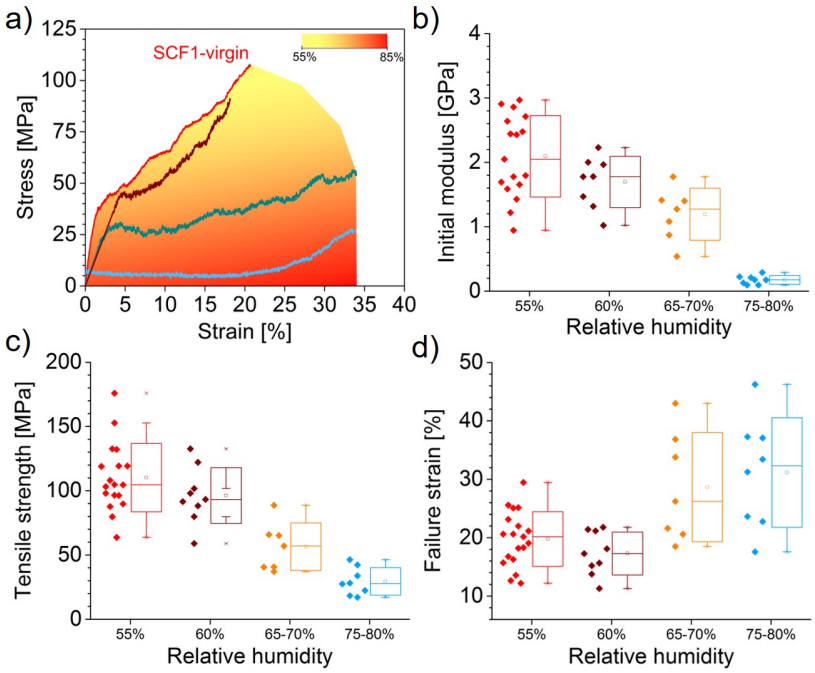

Figure 6.16: a) An envelope of stress-strain profiles is obtained by varying the level of humidity, and therefore the degree of hydration of the fibre. Significant differences in b) initial modulus, c) tensile strength and d) failure strain are observed for fibres with different degrees of hydration. Box plots show maximum and minimum (whiskers), upper and lower quartiles (box range), median, and mean (unfilled square).

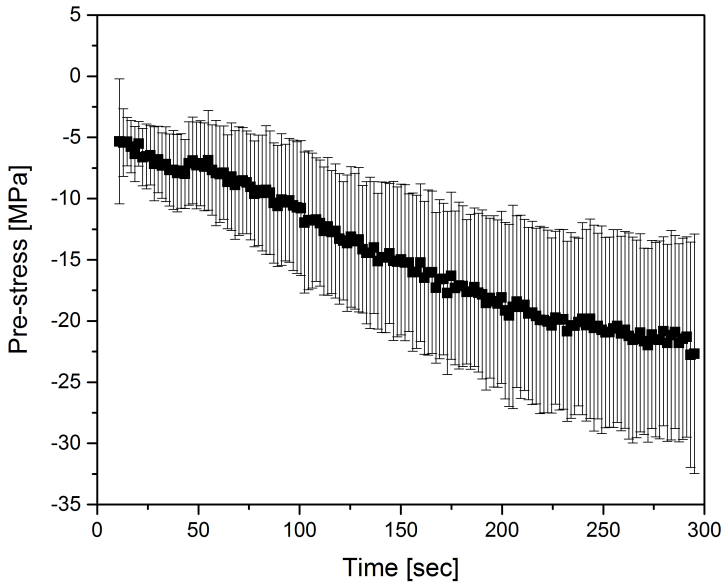

Figure 6.17: The evolution of supercontraction induced pre-stress as a function of time (n=8). The equilibrium compressive stress (reached typically after 4 min) was measured to be 20.0 $\pm$ 8.4 MPa.

Video S1 | Video of a section of **SCF** observed under ESEM with relative humidity decreasing from 99% to 40%, the diameter of the **SCF** decrease correspondingly, showing humidity sensitivity of the fiber.

Chapter 7

Conclusion and Outlook

Colloidal assemblies have become an important field in material science, with additional demand on the control in terms of its size, shape, composition and functions. Supramolecular approach has provided a unique platform to realize the assembly of colloidal building blocks, on account of its spontaneous, specific, directional and dynamic characteristics. With a precise tailoring of colloidal surfaces, emerging colloidal assemblies can be fabricated, exhibiting higher complexity and higher level of hybridization. Designing and fabricating different types of hybrid colloidal assembles based on the supramolecular host-guest interactions of cucurbit[n]uril (CB[n], primarily CB[7] and CB[8]) has been the primary aim in this thesis.

Cucurbit[n]urils are macrocyclic host molecules that shows high affinities towards various small molecules in water. More interestingly, CB[8] has the ability to bind two guest molecules simultaneously with high ternary binding constant (K_{eq} up to $10^{14}M^{-2}$).

It behaves like a supramolecular 'hand-cuff', joining complementary entities together spontaneously. Thus, the thesis (chapter 2) introduced the self-assembly of hybrid 'raspberry-like' colloids (HRCs). CB[8] effectively complexed the methyl viologen (MV) functionalised corona polymeric nanoparticles onto the azo-benzene (Azo) functionalised core silica colloids. The 'raspberry-like' structures were successfully characterized *via* TEM and SEM. Moreover, the dynamic interaction of CB[8] enables the colloidal assemblies being easily dissembled via external stimuli. This supramolecular approach allows for the synthesis of structured colloids that can be used to introduce the roughness of sur-

faces.

With a detailed study of CB[*n*] interacting towards metallic NPs, next, the fabrication of catalytic nanocomposties was presented (Chapter 3). Metastable palladium NPs were easily grafted onto the MV functionalised polymer colloids *via* CB[7] host-guest interactions. This can effectively prevent any aggregation of metallic NPs, and prolong its stability up to months. The nanocomposties has demonstrated a high catalytic efficiency with high recyclability. Moreover, this approach has shown that the nanocomposities could be prepared with various element of metallic NPs, which makes it promising in functional nanomaterials.

To prepare the structured colloids with high topological complexity, the design of the colloidal building blocks and the assembly strategies are of great importance (Chapter 4). This thesis shows the supramolecular assembly of Janus NPs in the compartmentalised environment. CB[8] directed the assembly of MV functionalised polymeric colloids onto micro-sized Np functionalised Janus NPs specifically on one side only. The compartmentalised droplets allow a confined assembling environment so that no aggregation would occur, in comparison to the assembly in bulk solution. Moreover, the control of the assembled structures could be achieved, with different level of grafting on the surface of the Janus NPs. This approach has demonstrated an effective combination of chemistry modification and on-demand strategy on the synthesis of structured colloids, representing a new platform for fabricating emerging colloidal assembly.

CB[8] based supramolecular hydrogels has been developed by complexing complementary functional polymers, with a selection of guest motifs, such as MV/Np, MV/Azo, Phe/Phe (phenylalanine) etc. These materials show remarkable properties of dynamic hydrogels, including self-healing, shear thinning, stimuli-responsive, elastic and high mouldability. In addition, the in-depth kinetics understanding of CB[8]-based hydrogels has been achieved. However, such studies has been focused on the alteration of materials from molecular level. Introducing shape-persistent nano-objects (colloids) into the hydrogel and precisely control its location in the polymeric matrix has not been investigated in details. Thus, we have fabricated the emerging hybrid polymeric colloidal

hydrogel based on the host-guest interactions of CB[8] (Chapter 5). Functional polymer grafted silica NPs were well dispersed into a semi-crystalline polymer matrix. The grafted polymers on silica NPs effectively interacted with the counterpart polymer, with little phase separation occurring. The resulting material exhibited enhanced elasticity where the hydrogel can be drawn into fibers with a high aspect ratio of 10^5. The formation of the fiber has been studied. It is the result of the reorganisation of hydrogel internal structures and the presence of crystallinity inside the hydrogel. Nanofibrils inside the hydrogel were characterized under the SEM, which contribute to the high elasticity of the hydrogel. Moreover, the investigation of the mechanical behaivour of these supramolecular fiber has been carried out. They exhibit a unique combination of ductility, stiffness and remarkably high damping capacity. Colloidal self-assemblies are essential for the advancing the future soft materials. Meanwhile, the hydrogel provides a new platform of fabricating novel fiber materials.

To further develop the fiber materials, we have explored the fiber network and prepared the 'like-silk' supercontractile fiber (SCF). On the basis of the supramolecular fiber scaffold, a second covalent network was effectively introduced. The resulting SCF has become not only resilient to water, but also shows stimuli-responsiveness in high humidity. The fiber exhibits up to 300% of uptake of water by its volume at high humidity. Moreover, the SCF undergoes a cyclic relaxation-contraction response to wetting and drying, similar to spider silk. This type of fiber materials has demonstrated the repeatable weight lifting experiments, bio-mimicking the muscle fibers.

In conclusion, the cucurbit[n]uril-based supramolecular chemistry can be effectively applied into the assembly of colloidal building blocks, demonstrate a wide platform for fabricating hybrid materials with emerging applications.

Bibliography

[1] Cölfen, H.; Mann, S. *Angew. Chem. Int. Ed.* **2003**, 2350–2365.

[2] Koshland, D. E. **1994**, 2375–2378.

[3] Lehn, J.-m. *Angew. Chem. Int. Ed.* **1988**, *27*, 89–112.

[4] Ikkala, O. *Chem. Commun.* **2004**, 2131–2137.

[5] Amabilino, D. B.; Smith, D. K.; Steed, J. W. *Chem. Soc. Rev.* **2017**, *46*, 2404–2420.

[6] Stupp, S. I.; Lebonheur, V.; Walker, K.; Li, L. S.; Huggins, K. E.; Keser, M.; Amstutz, A. *Science* **1997**, *276*.

[7] Webber, M. J.; Appel, E. A.; Meijer, E. W.; Langer, R. *Nat. Mater.* **2016**, *15*, 13–26.

[8] Heinzmann, C.; Weder, C.; Espinosa, L. M. D. *Chem. Soc. Rev.* **2016**, *45*, 342–358.

[9] Barton, J. K.; Lippard, S. J. *J. Am. Chem. Soc.* **1978**, *8059*, 3227–3229.

[10] Hastings, C. J.; Pluth, M. D.; Bergman, R. G.; Raymond, K. N. *J. Am. Chem. Soc.* **2010**, *2*, 6938–6940.

[11] Vriezema, D. M.; Aragone, M. C.; Elemans, J. A. A. W.; Cornelissen, J. J. L. M.; Rowan, A. E.; Nolte, R. J. M. *Chem. Rev.* **2005**,

[12] Smith, D. K. *J. Chem. Educ.* **2005**, *82*, 393–400.

[13] et. al., D. R. B. *Nature* **1997**,

[14] Buckley, R. H.; Ward, F. E. *The New England Journal of Medicine* **1999**,

[15] Dumoulin, M.; Last, A. M.; Desmyter, A.; Spencer, A.; Decanniere, K.; Canet, D.; Archer, D. B.; Sasse, J.; Muyldermans, S.; Wyns, L.; Robinson, C. V.; Redfield, C.; Dobson, C. M. *Nature* **2003**, *424*, 783–788.

[16] Dobson, C. M. *Nature* **2005**, *435*, 747–749.

[17] Soc, J. A. C.; Whitesides, G. M.; Grzybowski, B. *Science* **2002**, *295*, 2418–2421.

[18] Jenekhe, S. A.; L, C. X. *Science* **1999**, *283*, 372–376.

[19] Sukhishvili, S. A.; Granick, S. *Macromolecules* **2002**, 301–310.

[20] Schalley, C. A. *Noncovalent Bonding in Supramolecular Chemistry*; Wiley-VCH: Weinheim, 2007; pp 1–4.

[21] Lodish, H.; Berk, A.; Zipursky, S. L. *Molecular Cell Biology. 4th edition*; New York: W. H. Freeman, 2000.

[22] Szejtli, J. *Cyclodextrin Technology*; New York: Springer, 1988.

[23] Gutsche, C. D. *Calixarenes*; Cambridge: Royal Society of Chemistry, 1989.

[24] Lagona, J.; Mukhopadhyay, P.; Chakrabarti, S.; Isaacs, L. *Angewandte Chemie (International ed. in English)* **2005**, *44*, 4844–70.

[25] Calcd, F. **2010**, *57*, 11–12.

[26] Takeda, Y. *Bulletin of the Chemical Society of Japan* **1998**, *61*, 627.

[27] Nau, W. M.; Scherman, O. A. *Isr. J. Chem.* **2011**, 492–494.

[28] Freeman, W. A.; Mock, W. L.; Shih, N. Y. *J Am Chem Soc* **1981**, *103*, 7367.

[29] Burton, D. J.; Naae, D. G.; Flynn, R. M. *J. Org. Chem.* **1983**, 3618–3619.

[30] Mock, W. L.; Shih, N.-y. *J. Org. Chem* **1986**, *60680*, 4440–4446.

[31] Behrend, R.; Meyer, E.; Rusche, F. *Justus Liebigs Annalen der Chemie* **1905**, *1*, 339.

[32] S, J. L.; Chemie, A. D. E. R. *ANNALEN DER CHEMIE*. **1904**,

[33] Day, a.; Arnold, a. P.; Blanch, R. J.; Snushall, B. *The Journal of organic chemistry* **2001**, *66*, 8094–100.

[34] Kim, J.; Jung, I.-s.; Kim, S.-y.; Lee, E.; Kang, J.-k.; Sakamoto, S.; Yamaguchi, K.; Kim, K.; Hyojadong, S.; Korea, R. **2000**, *19*, 540–541.

[35] Sasmal, S.; Sinha, M. K.; Keinan, E. *Org. Lett.* **2004**, 4–7.

[36] Hough, G. C.; Williams, D. J. **1992**, 1991–1993.

[37] Park, K. M.; Yang, J.-a.; Jung, H.; Yeom, J.; Park, J. S.; Park, K.-h.; Hoffman, A. S.; Hahn, S. K.; Kim, K.; Al, P. E. T. *ACS Nano* **2012**, *6*, 2960–2968.

[38] Zhao, J.; Kim, H.-j.; Oh, J.; Kim, S.-y.; Lee, J. W.; Sakamoto, S.; Yamaguchi, K.; Kim, K. **2001**, 4363–4365.

[39] Jon, S. Y.; Selvapalam, N.; Oh, D. H.; Kang, J.-k.; Kim, S.-y.; Jeon, Y. J.; Lee, J. W.; Kim, K. *J. Am. Chem. Soc.* **2003**, 10186–10187.

[40] Lee, J. W.; Samal, S.; Selvapalam, N.; Kim, H.-J.; Kim, K. *Acc. Chem. Res.* **2003**, *36*, 621–30.

[41] Marquez, C.; Hudgins, R. R.; Nau, W. M. *J. Am. Chem. Soc.* **2004**, *126*, 5806–5816.

[42] Nau, W. M.; Florea, M.; Assaf, K. I. *Isr. J. Chem.* **2011**, *51*, 559–577.

[43] Masson, E.; Ling, X.; Joseph, R.; Kyeremeh-Mensah, L.; Lu, X. *RSC Advances* **2012**, *2*, 1213.

[44] Assaf, K. I.; Nau, W. M. *Chem. Soc. Rev.* **2014**, *44*, 394–418.

[45] Biedermann, F.; Scherman, O. A. **2012**,

[46] Kellersberger, K. A.; Anderson, J. D.; Ward, S. M.; Krakowiak, K. E.; Dearden, D. V. **2001**, 11316–11317.

[47] Buschmann, H.-J.; Jansen, K.; Schollmeyer, E. *Inorg. Chem. Commun.* **2003**, *6*, 531–534.

[48] Zhang, H.; Paulsen, E. S.; Walker, K. A.; Krakowiak, K. E.; Dearden, D. V. *J. Am. Chem. Soc.* **2003**, 9284–9285.

[49] Phenomena, I.; Recognition, M.; Publishers, K. A.; Nord-west, D. T. *J. Inclusion Phenom. Mol. Recognit. Chem.* **1992**, *14*, 91–99.

[50] Florea, M.; Nau, W. M. *Angew. Chem. Int. Ed.* **2011**, *50*, 9338–9342.

[51] Jeon, W. S.; Moon, K.; Park, S. H.; Chun, H.; Ko, Y. H.; Lee, J. Y.; Lee, E. S.; Samal, S.; Selvapalam, N.; Rekharsky, M. V.; Sindelar, V.; Sobransingh, D.; Inoue, Y.; Kaifer, A. E.; Kim, K. *J. Am. Chem. Soc.* **2005**, *2*, 12984–12989.

[52] Ko, Y. H.; Kim, Y.; Kim, H.; Kim, K. *Chemistry, an Asian journal* **2011**, *6*, 652–7.

[53] Moghaddam, S.; Yang, C.; Rekharsky, M.; Ko, Y. H.; Kim, K.; Inoue, Y.; Gilson, M. K. *J. Am. Chem. Soc.* **2011**, 3570–3581.

[54] Rekharsky, M. V.; Mori, T.; Yang, C.; Ko, Y. H.; Selvapalam, N.; Kim, H.; Sobransingh, D.; Kaifer, A. E.; Liu, S.; Isaacs, L.; Chen, W.; Moghaddam, S.; Gilson, M. K.; Kim, K.; Inoue, Y. *Proc. Natl. Acad. Sci. U.S.A.* **2007**, *104*, 20737–20742.

[55] Ko, Y. H.; Kim, E.; Hwang, I.; Kim, K. *Chem. Commun.* **2007**, 1305–1315.

[56] Rauwald, U.; del Barrio, J.; Loh, X. J.; Scherman, O. a. *Chemical communications (Cambridge, England)* **2011**, *47*, 6000–2.

[57] Rauwald, U.; Robinson, C. V.; Scherman, O. A. *Chem. Commun.* **2009**, 644–646.

[58] Biedermann, F.; Uzunova, V. D.; Scherman, O. A.; Nau, W. M.; Simone, A. D. *J. Am. Chem. Soc.* **2012**,

[59] Rauwald, U.; Biedermann, F.; Robinson, C. V.; Scherman, O. A. *J. Phys. Chem. B* **2010**, 8606–8615.

[60] Biedermann, F.; Rauwald, U.; Zayed, J. M.; Scherman, O. A. *Chem. Sci.* **2011**, *2*, 279–286.

[61] Appel, E. A.; Jun, X.; Jones, S. T.; Dreiss, C. A.; Scherman, O. A. *Biomaterials* **2012**, *33*, 4646–4652.

[62] Sci, C.; Appel, E. A.; Dyson, J.; Scherman, O. A. *Chem. Sci.* **2012**, 2278–2281.

[63] Zhang, J.; Coulston, R. J.; Jones, S. T.; Geng, J.; Scherman, O. A.; Abell, C. *Science* **2012**, *335*, 690–694.

[64] Coulston, R. J.; Jones, S. T.; Lee, T.-c.; Appel, E. A.; Scherman, O. A. *Chem. Commun.* **2011**, 164–166.

[65] Tian, F.; Cheng, N.; Nouvel, N.; Geng, J.; Scherman, O. A. *Langmuir* **2010**, *26*, 5323–5328.

[66] Appel, E. A.; Loh, X. J.; Jones, S. T.; Biedermann, F.; Dreiss, C. A.; Scherman, O. A. *J. Am. Chem. Soc.* **2012**, *134*, 11767–11773.

[67] Wagner, F. E.; Haslbeck, S.; Stievano, L.; Calogero, S.; Pankhurst, Q. A.; Martinek, K.-P. *Nature* **2000**, *407*, 691–692.

[68] Hauser, E. A. *J. Chem. Educ.* **1932**,

[69] Wang, D.; Mo, H.; Wang, D. *J. Mater. Chem.* **2004**, 459–468.

[70] Park, J.-g.; Forster, J. D.; Dufresne, E. R. *J. Am. Chem. Soc.* **2010**, 5960–5961.

[71] Vogel, N.; Retsch, M.; Fustin, C.-a.; Campo, A.; Jonas, U. *Chem. Rev.* **2015**,

[72] Yi, G.-r.; Pine, D. J.; Sacanna, S. *J. Phys. Condens. Matter* **2013**,

[73] Mcgorty, R.; Fung, J.; Kaz, D.; Manoharan, V. N. *Mater. Today* **2010**, *13*, 34–42.

[74] Hepp, K. *Colloids and the Depletion Interaction*; Springer, 2011.

[75] Zhang, B. J.; Li, Y.; Zhang, X.; Yang, B. *Adv. Mater.* **2010**, *130012*, 4249–4269.

[76] Yin, Y.; Lu, Y.; Gates, B.; Xia, Y.; April, R. V. *J. Am. Chem. Soc.* **2001**, *25*, 8718–8729.

[77] Furst, E. M. *Proc. Natl. Acad. Sci. U.S.A.* **2011**, *108*, 20853–20854.

[78] Parak, W. J. *Science* **2011**, *334*, 1359–1361.

[79] Hoon, K.; Jeong, J.-m.; Jae, S.; Gill, B.; Lee, K. G. *J. Colloid Interface Sci.* **2016**, *484*, 44–50.

[80] Hong, L.; Cacciuto, A.; Luijten, E.; Granick, S. *Nano Lett.* **2006**,

[81] Piccinini, E.; Pallarola, D.; Azzaroni, O. *Molecular Systems Design & Engineering* **2016**, *1*, 155–162.

[82] Busseron, E.; Ru, Y.; Moulin, E.; Giuseppone, N. *Nanoscale* **2013**, 7098–7140.

[83] Lu, Y.; Yin, Y.; Li, Z.-y.; Xia, Y. *Nano Lett.* **2002**, 2–5.

[84] Du, J.; Reilly, R. K. *Chem. Soc. Rev.* **2011**, 2402–2416.

[85] Dendukuri, D.; Doyle, P. S. *Adv. Mater.* **2009**, *21*, 4071–4086.

[86] Yin, Y.; Xia, Y. *J. Am. Chem. Soc.* **2003**, 2048–2049.

[87] Sacanna, S.; Irvine, W. T. M.; Chaikin, P. M.; Pine, D. J. *Nature* **2010**, *464*, 575–578.

[88] Sacanna, S.; Korpics, M.; Rodriguez, K.; Colo, L.; Kim, S.-h.; Pine, D. J.; Yi, G.-r. *Nat. Commun.* **2013**, 2–7.

[89] Kim, S.-h.; Hollingsworth, A. D.; Sacanna, S.; Chang, S.-j.; Lee, G.; Pine, D. J.; Yi, G.-r. *J. Am. Chem. Soc.* **2012**,

[90] Manoharan, V. N.; Elsesser, M. T.; Pine, D. J. *Science* **2003**, *301*, 483–487.

[91] Sacanna, S.; Pine, D. J. *Curr. Opin. Colloid Interface Sci.* **2011**, *16*, 96–105.

[92] Weisbecker, C. S.; Merritt, M. V.; Whitesides, G. M. *Langmuir* **1996**, *7463*, 3763–3772.

[93] Mirkin, C. A.; Letsinger, R. L.; Micic, R.; Storhoff, J. *Nature* **1996**,

[94] Sun, S.; Anders, S.; Hamann, H. F.; Thiele, J.-u.; Baglin, J. E. E.; Thomson, T.; Fullerton, E. E.; Murray, C. B.; Terris, B. D.; Road, H.; Jose, S. *J. Am. Chem. Soc.* **2002**, *124*, 2884–2885.

[95] Choueiri, R. M.; Galati, E.; Thérien-aubin, H.; Klinkova, A.; Larin, E. M.; Querejeta-fernández, A.; Han, L.; Xin, H. L.; Gang, O.; Zhulina, E. B.; Rubinstein, M.; Kumacheva, E. *Nature* **2016**, *538*, 79–83.

[96] Boal, A. K.; Ilhan, F.; Derouchey, J. E.; Thurn-albrecht, T.; Russell, T. P.; Rotello, V. M. *Nature* **2000**, *404*, 746–748.

[97] Korth, B. D.; Keng, P.; Shim, I.; Bowles, S. E.; Tang, C.; Kowalewski, T.; Nebesny, K. W.; Pyun, J. *J. Am. Chem. Soc.* **2006**, 6562–6563.

[98] Vestal, C. R.; Zhang, Z. J. *J. Am. Chem. Soc.* **2002**, 14312–14313.

[99] Lan, Y.; Loh, X. J.; Geng, J.; Walsh, Z.; Scherman, O. a. *Chemical communications (Cambridge, England)* **2012**, *48*, 8757–9.

[100] Kraft, D. J.; Ni, R.; Smallenburg, F.; Hermes, M.; Yoon, K.; Weitz, D. A.; Blaaderen, A. V. *Proc. Natl. Acad. Sci. U.S.A.* **2012**, *109*, 10787–10792.

[101] Werne, T. V.; Patten, T. E. *J. Am. Chem. Soc.* **1999**, 7409–7410.

[102] Park, M.-k.; Onishi, K.; Locklin, J.; Caruso, F.; Advincula, R. C. *Langmuir* **2003**, 8550–8554.

[103] Kawaguchi, H. *Prog. Polym. Sci.* **2000**, *25*, 1171–1210.

[104] Champion, J. a.; Katare, Y. K.; Mitragotri, S. *Journal of controlled release : official journal of the Controlled Release Society* **2007**, *121*, 3–9.

[105] Zhang, Q.; Chuang, K. T. *Advances in Environmental Research* **2001**, *5*, 251–258.

[106] Fudouzi, H.; Xia, Y. *Advanced Materials* **2003**, *15*, 892–896.

[107] Thickett, S. C.; Gilbert, R. G. *Polymer* **2007**, *48*, 6965.

[108] Kim, S. W.; Cho, C. R., H. G.and Park *Langmuir* **2009**, *25*, 9030.

[109] Choe, S.; Kim, G.; Lim, S.; Lee, B. H.; Shim, E. *Polymer* **2010**, *51*, 1197.

[110] Bai, F.; Huang, B.; Yang, X.; Huang, W. *Polymer* **2007**, *48*, 3641–3649.

[111] Fu, G.-D.; Li, G. L.; Neoh, K.; Kang, E. *Prog. Polym. Sci.* **2011**, *36*, 127–167.

[112] Li, W.-h.; Sto, H. D. H. **2000**, 4354–4360.

[113] Madani, A.; Nessark, B.; Brayner, R.; Elaissari, H.; Jouini, M.; Mangeney, C.; Chehimi, M. M. *Polymer* **2010**, *51*, 2825–2835.

[114] Wang, J.; Yang, X. *Langmuir : the ACS journal of surfaces and colloids* **2008**, *24*, 3358–3364.

[115] Ming, W.; Wu, D.; van Benthem, R.; de With, G. *Nano Lett.* **2005**, *5*, 2298–2301.

[116] Polymerization, M. **2005**, 2124–2128.

[117] Chen, M.; Zhou, S.; You, B.; Wu, L. **2005**, 6411–6417.

[118] Biedermann, F.; Elmalem, E.; Ghosh, I.; Nau, W. M.; Scherman, O. A. *angew. chem. int. ed* **2012**, *51*, 7739–43.

[119] Graf, C.; Vossen, D. L. J.; Imhof, A.; van Blaaderen, A. *Langmuir* **2003**, *19*, 6693–6700.

[120] Jiao, D. Z.; Zhao, N.; Scherman, O. A. *Chem. Commun.* **2010**, *46*, 2007–2009, 566PG Times Cited:10 Cited References Count:17.

[121] Huang, J.; Jiang, T.; Gao, H.; Han, B.; Liu, Z.; Wu, W.; Chang, Y.; Zhao, G. *Angew. Chem. Int. Ed.* **2004**, *116*, 1421–1423.

[122] Argo, A. M.; Odzak, J. F.; Lai, F. S.; Gates, B. C. *Nature* **2002**, *415*, 623–626.

[123] Bell, A. T. *Science* **2003**, *299*, 1688–1691.

[124] Gallon, B. J.; Kojima, R. W.; Kaner, R. B.; Diaconescu, P. L. *Angew. Chem. Int. Ed.* **2007**, *46*, 7251–7254.

[125] Gates, B. C. *Chem. Commun.* **2013**, *49*, 7876–7877.

[126] Narayanan, R.; El-Sayed, M. A. *J. Am. Chem. Soc.* **2003**, *125*, 8340–8347.

[127] Landon, P.; Collier, P. J.; Papworth, A. J.; Kiely, C. J.; Hutchings, G. J. *Chem. Commun.* **2002**, *18*, 2058–2059.

[128] Han, J.; Liu, Y.; Guo, R. *Adv. Funct. Mater.* **2009**, *19*, 1112–1117.

[129] Heitz, W.; Greiner, A.; Oestreich, S.; Fo, S. *J. Am. Chem. Soc.* **1997**, *38*, 10116–10120.

[130] Scheuermann, G. M.; Rumi, L.; Steurer, P.; Bannwarth, W.; Mülhaupt, R. *J. Am. Chem. Soc.* **2009**, *131*, 8262–8270.

[131] Lidia, S.; Jian, L.; Kaifer, A. E. *Langmuir* **2003**, *19*, 483–485.

[132] Premkumar, T.; Geckeler, K. E. *Mater. Chem. Phys.* **2014**, *148*, 772–777.

[133] Lee, T.-C.; Scherman, O. A. *Chem. Eur. J.* **2012**, *18*, 1628–1633.

[134] Wang, Y.; Wang, Y.; Breed, D. R.; Manoharan, V. N.; Feng, L.; Hollingsworth, A. D.; Weck, M.; Pine, D. J. *Nature* **2012**, 51–55.

[135] Valignat, M. P.; Theodoly, O.; Crocker, J. C.; Russel, W. B.; Chaikin, P. M. *Proc. Natl. Acad. Sci. U.S.A.* **2005**, *102*, 4225–4229.

[136] Chen, Q.; Bae, S. C.; Granick, S. *Nature* **2011**, *469*, 381–384.

[137] Cho, Y. S.; Yi, G. R.; Lim, J. M.; Kim, S. H.; Manoharan, V. N.; Pine, D. J.; Yang, S. M. *J. Am. Chem. Soc.* **2005**, *127*, 15968–15975.

[138] van Blaaderen, A.; Ruel, R.; Wiltzius, P. Template-directed colloidal crystallization. 1997.

[139] Nych, A.; Ognysta, U.; Škarabot, M.; Ravnik, M.; Žumer, S.; Muševič, I. *Nat. Commun.* **2013**, *4*, 1489.

[140] Yang, S.-M.; Kim, S.-H.; Lim, J.-M.; Yi, G.-R. *J. Mater. Chem.* **2008**, *18*, 2177.

[141] Nykypanchuk, D.; Maye, M. M.; van der Lelie, D.; Gang, O. *Nature* **2008**, *451*, 549–552.

[142] Perro, A.; Reculusa, S.; Ravaine, S.; Bourgeat-Lami, E. B.; Duguet, E. *J. Mater. Chem.* **2005**, *15*, 3745–3760.

[143] Zhao, Y.; Gu, H.; Xie, Z.; Shum, H. C.; Wang, B.; Gu, Z. *J. Am. Chem. Soc.* **2013**, *135*, 54–57.

[144] Jiang, S.; Chen, Q.; Tripathy, M.; Luijten, E.; Schweizer, K. S.; Granick, S. *Adv. Mater.* **2010**, *22*, 1060–1071.

[145] Lattuada, M.; Hatton, T. A. *J. Am. Chem. Soc.* **2007**, *129*, 12878–12889.

[146] Walther, A.; Muller, A. H. E. *Chem. Rev.* **2013**, *113*, 5194–5261.

[147] Gao, W.; Pei, A.; Feng, X.; Hennessy, C.; Wang, J. *J. Am. Chem. Soc.* **2013**, *135*, 998–1001.

[148] Yan, J.; Bloom, M.; Bae, S. C.; Luijten, E.; Granick, S. *Nature* **2012**, *491*, 578–581.

[149] Nie, L.; Liu, S.; Shen, W.; Chen, D.; Jiang, M. *Angew. Chem. Int. Ed.* **2007**, *46*, 6321–6324.

[150] Chen, Q.; Whitmer, J. K.; Jiang, S.; Bae, S. C.; Luijten, E.; Granick, S. *Science* **2011**, *331*, 199–202.

[151] Liu, B.; Wei, W.; Qu, X.; Yang, Z. *Angew. Chem. Int. Ed.* **2008**, *47*, 3973–3975.

[152] Paunov, V. N.; Cayre, O. J. *Adv. Mater.* **2004**, *16*, 788–791.

[153] Baraban, L.; Makarov, D.; Streubel, R.; Mönch, I.; Grimm, D.; Sanchez, S.; Schmidt, O. G. *ACS Nano* **2012**, *6*, 3383–3389.

[154] Nie, Z.; Li, W.; Seo, M.; Xu, S.; Kumacheva, E. *J. Am. Chem. Soc.* **2006**, *128*, 9408–9412.

[155] Saito, N.; Kagari, Y.; Okubo, M. *Langmuir* **2006**, *22*, 9397–9402.

[156] Tanaka, T.; Nakatsuru, R.; Kagari, Y.; Saito, N.; Okubo, M. *Langmuir* **2008**, *24*, 12267–12271.

[157] Yang, S.; Guo, F.; Kiraly, B.; Mao, X.; Lu, M.; Leong, K. W.; Huang, T. J. *Lab. Chip* **2012**, *12*, 2097.

[158] Zerrouki, D.; Baudry, J.; , D.; Chaikin, P.; Bibette, J. *Nature* **2008**, *455*, 380–382.

[159] Zhou, Y.; Wang, D.; Huang, S.; Auernhammer, G.; He, Y.; Butt, H.-J.; Wu, S. *Chem. Commun.* **2015**, *51*, 2725–2727.

[160] Isaacs, L. *Chem. Commun.* **2009**, 619–629.

[161] Baret, J.-c.; Miller, O. J.; Taly, V.; El-harrak, A.; Frenz, L.; Rick, C.; Samuels, M. L.; Hutchison, J. B.; Agresti, J. J.; Link, D. R.; Weitz, D. A.; Griffiths, A. D. *Lab. Chip* **2009**, *9*.

[162] Rising, A.; Johansson, J. *Nat. Chem. Biol.* **2015**, *11*, 309–15.

[163] Vollrath, F.; Knight, D. P. *Nature* **2001**, *410*, 541–8.

[164] Greiner, A.; Wendorff, J. H. *Angew. Chem. Int. Ed.* **2007**, *46*, 5670–5703.

[165] Whitesides, G. M.; Mathias, J. P.; Seto, C. T. *Science (New York, N.Y.)* **1991**, *254*, 1312–9.

[166] Webber, M. J.; Appel, E. A.; Meijer, E. W.; Langer, R. *Nature Materials* **2016**, *15*, 13–26.

[167] Aida, T.; Meijer, E. W.; Stupp, S. I. *Science* **2012**, *335*, 813–817.

[168] Capito, R.; Azevedo, H.; Velichko, Y.; Mata, A.; Stupp, S. *Science* **2008**, *319*, 1812–1816.

[169] Nelson, R.; Sawaya, M. R.; Balbirnie, M.; Madsen, A. Ø.; Riekel, C.; Grothe, R.; Eisenberg, D. *Nat. Cell Biol.* **2005**, *435*, 773–778.

[170] Zhang, S.; Greenfield, M. A.; Mata, A.; C., P. L.; Bitton, R.; Mantei, J. R.; Aparicio, C.; Cruz, M. O. d. l.; Stupp, S. I. *Nature Materials* **2010**, *9*, 594–601.

[171] Dankers, P.; Harmsen, M.; Brouwer, M. J. A. V., L. A. abd Luyn; Meijer, E. W. *Nature Materials* **2005**, *4*, 568–574.

[172] Merzlyak, A.; Indrakanti, S.; Lee, S. W. *Nano Lett.* **2009**, *9*, 846–852.

[173] Reches, M.; Gazit, E. *Science* **2003**, *300*, 625–627.

[174] Hartgerink, J. D.; Beniash, E.; Stupp, S. I. *Science* **2001**, *294*, 1684–1688.

[175] Kato, T.; Mizoshita, N.; Kishimoto, K. *Angew. Chem. Int. Ed.* **2005**, *45*, 38–68.

[176] Loh, J.; Scherman, O. A.; Appel, E. A. *Chem. Soc. Rev.* **2012**, 6195–6214.

[177] Reinhoudt, D.; Atwood, J.; M., L. J. *omprehensive Supramolecular Chemistry, Pergamon Press, Oxford*; 1996.

[178] Seiffert, S.; Sprakel, J. *Chem. Soc. Rev.* **2012**, *41*, 909–930.

[179] Appel, E. A.; Loh, X. J.; Jones, S. T.; Biedermann, F.; Dreiss, C. A.; Scherman, O. A. *J. Am. Chem. Soc.* **2012**, *134*, 11767–11773.

[180] Cordier, P.; Tournilhac, F.; S., Z. C.; Leibler, L. *Nature* **2008**, *451*, 997–980.

[181] Sijbesma, R. P.; Meijer, E. W. *Curr. Opin. Colloid Interface* **1999**, *4*, 24–32.

[182] Kumpfer, J. R.; Rowan, S. J. *J. Am. Chem. Soc.* **2011**, *133*, 12866–12874.

[183] Weng, W.; Beck, J. B.; Jamieson, A. M.; Rowan, S. J. *J. Am. Chem. Soc.* **2006**, 11663–11672.

[184] Liu, S.; Ruspic, C.; Mukhopadhyay, S., P.and Chakrabarti; Zavalij, P.; Isaacs, L. *J. Am. Chem. Soc.* **2005**, *127*, 15959–15967.

[185] Szetjli, J. *Chem. Rev.* **1998**, *98*, 1743–1753.

[186] Wang, Q.; Mynar, J. L.; Yoshida, M.; Lee, E.; Lee, M.; Okuro, K.; Kinbara, K.; Aida, T. *Nature* **2010**, *463*, 339–343.

[187] Mynar, J. L.; Aida, T. *Nature* **2008**, *451*, 895–896.

[188] Shea, E. K. O.; Rutkowski, R.; Kim, P. S. *Science* **1987**, *243*.

[189] Petka, W. A.; Harden, J. L.; Mcgrath, K. P.; Wirtz, D.; Tirrell, D. A. *Science* **1998**, *281*, 389–393.

[190] Appel, E. A.; Loh, X. J.; Jones, S. T.; Dreiss, C. A.; Scherman, O. A. *Biomaterials* **2012**, *33*, 4646–4652.

[191] Tan, C. S. Y.; Barrio, J.; Liu, J.; Scherman, O. A. *Polym. Chem.* **2015**, *6*, 7652–7657.

[192] Rowland, M. J.; Appel, E. A.; Coulston, R. J.; Scherman, O. A. *J. Mater. Chem.* **2013**, *1*, 2904–2910.

[193] Rowland, M. J.; Atgie, M.; Hoogland, D.; Scherman, O. A. *Biomacromolecules* **2015**, *1*, 2436–2443.

[194] Li, C.; Rowland, M. J.; Shao, Y.; Cao, T. Y.; Chen, C.; Jia, H. Y.; Zhou, X.; Yang, Z. Q.; Scherman, O. A.; Liu, D. S. *Adv. Mater.* **2015**, *21*, 3298–3304.

[195] Rose, S.; Prevoteau, A.; Elzière, P.; Hourdet, D.; Marcellan, A.; Leibler, L. *Nature* **2014**, *505*, 382–385.

[196] Lan, Y.; Loh, X. J.; Geng, J.; Walsh, Z.; Scherman, O. A. *Chem. Commun.* **2012**, *48*, 8757–8759.

[197] Shah, D.; D., P.; F., V. *Compos. Sci. Technol.* **2014**, *101*, 173–183.

[198] Lewin, M. *Handbook of fiber chemistry. Boca Raton: CRC Press LLC.*; 2007.

[199] Dumanli, A.; A.H., W. *J. Mater. Sci.* **2012**, *47*, 4236–4250.

[200] Romer, T.; Scheibel, T. *Prion* **2008**, *2*, 154–161.

[201] Trivedi, M. K.; Nayak, G.; Patil, S.; Tallapragada, R. M.; Mishra, R. *J. Mol. Pharm. Org. Process Res.* **2015**, *3*, 154–161, doi: 10.4172/2329-9053.1000126.

[202] Mukerabigwi, J. F. e. a. *RSC Adv.* **2016**, *6*, 31607–31618.

[203] Colomban, P.; Dinh, H.; Bunsell, A.; Mauchamp, B. *J. Raman Spectrosc.* **2012**, *43*, 425–432.

[204] Aslan, M.; Chinga-Carrasco, G.; Sø rensen, B.; Madsen, B. *J. Raman Spectrosc.* **2011**, *46*, 6344–6354.

[205] Vollrath, F.; Porter, D.; Holland, C. *MRS Bulletin* **2013**, *38*, 73–80.

[206] Shao, Z.; Vollrath, F. *Polymer* **1999**, *40*, 1799–1806.

[207] Kelly, S.; Sensenig, A.; Lorentz, K.; Blackledge, T. *Zoology* **2011**, *114*, 233–238.

[208] Tommasi, D. D.; Puglisi, G.; Saccomandi, G. *Biophys. J.* **2010**, *98*, 1941–1948.

[209] Germack, T. A. e. a. *J. Am. Chem. Soc.* **2008**, *125*, 3831–3838.

[210] Wu, T.; Zhang, Y. F.; Wang, X. F.; Y., L. S. *Chem. Mater.* **2008**, *20*, 101–109.

[211] Egan, P.; Sinko, R.; Leduc, P. R.; Keten, S. *Nat. Commun.* **2015**, *6*, 1–12.

[212] Zhao, H.; Feng, X.; Shi, H. *Mater. Sci. Eng. C* **2007**, *27*, 675–683.

[213] Nawroth, J. C.; Lee, H.; Feinberg, A. W.; Ripplinger, C. M.; Mccain, M. L.; Grosberg, A.; Dabiri, J. O.; Parker, K. K. *Nat. Biotechnol.* **2012**, *30*, 792–797.

[214] Heim, M.; Keerl, D.; Scheibel, T. *Angew. Chem.* **2009**, 3584–3596.

[215] Ene, R.; Papadopoulos, P.; Kremer, F. *Soft Mater.* **2009**, *212*, 4568–4574.

[216] Blackledge, T. A.; Boutry, C.; Wong, S.-c.; Baji, A.; Dhinojwala, A.; Sahni, V.; Agnarsson, I. *J. Exp. Biol.* **2009**, *2*, 1981–1989.

[217] Agnarsson, I.; Dhinojwala, A.; Sahni, V.; Blackledge, T. A. *J. Exp. Biol.* **2009**, 1990–1994.

[218] Boutry, C.; Blackledge, T. A. *J. Exp. Biol.* **2010**, 3505–3514.

[219] Liu, Y. I.; Shao, Z.; Vollrath, F. *Nat. Mater.* **2005**, *4*, 901–905.

[220] Qin, Z.; Buehler, M. J. *Nat. Mater.* **2013**, *12*, 185–187.

[221] Zheng, Y.; Bai, H.; Huang, Z.; Tian, X.; Nie, F.-q.; Zhao, Y.; Zhai, J.; Jiang, L. *Nature* **2010**, *463*, 640–643.

[222] Huang, X.; Liu, G.; Wang, X. *Adv. Mater.* **2012**, 1482–1486.

[223] Agnarsson, I.; Boutry, C.; Wong, S.-c.; Baji, A.; Dhinojwala, A.; Sensenig, A. T.; Blackledge, T. A. *Zoology* **2009**, *112*, 325–331.

[224] Haines, C. S. et al. *Science* **2014**, *343*.

[225] Haines, C. S.; Li, N.; Spinks, G. M.; Aliev, A. E.; Di, J.; Baughman, R. H. *Proc. Natl. Acad. Sci. U.S.A.* **2016**, *113*, 11709–11716.

[226] Wu, Y.; Shah, D. U.; Liu, C.; Yu, Z.; Liu, J.; Ren, X.; Rowland, M. J.; Abell, C. *Proc. Natl. Acad. Sci. U.S.A.* **2017**, *114*.

[227] Liu, X.; Won, Y.; Ma, P. X. *Biomaterials* **2006**, *27*, 3980–3987.

[228] Benavente, R.; Mijangos, C.; Peren, J. M.; Krumova, M.; Lo, D. *Polymer* **2000**, *41*, 9265–9272.

[229] Perez-Rigueiro, J.; Elices, M.; Guinea, G. *Polymer* **2003**, *3861*.

[230] Elices, M.; Plaza, G. R. *J. Exp. Biol.* **2005**, *208*, 25–30.

[231] Elices, M.; Plaza, G. R.; Pérez-rigueiro, J. *J. Mech. Behav. Biomed.* **2011**, *4*, 658–669.